To fold or not to fold?

An exploration of deployable porous biomaterials for the treatment of large bone defects

Bobbert, F.S.L.

DOI

Publication date

2021

Document Version

Final published version

Citation (APA)

Important note

To cite this publication, please use the final published version (if applicable).
Please check the document version above.

To fold or not to fold?

An exploration of deployable porous biomaterials for the treatment of large bone defects

To fold or not to fold?

An exploration of deployable porous biomaterials for the treatment of large bone defects

Proefschrift

ter verkrijging van de graad van doctor
aan de Technische Universiteit Delft,
op gezag van de Rector Magnificus, Prof.dr.ir. T.H.J.J. van der Hagen,
voorzitter van het College voor Promoties,
in het openbaar te verdedigen op
vrijdag 9 juli 2021 om 12:30 uur.

door

Françoise Siu Lin BOBBERT

Master of Science in Biomedical Engineering,
Technische Universiteit Delft, Nederland,
geboren te Amstelveen, Nederland.

Dit proefschrift is goedgekeurd door de promotor.

Samenstelling promotiecommissie bestaat uit:

Rector magnificus,	voorzitter
Prof.dr. A.A. Zadpoor	Technische Universiteit Delft, promotor

Onafhankelijke leden:

Prof.dr.ir. J.L. Herder	Technische Universiteit Delft
Prof.dr. E. Karana	Technische Universiteit Delft
Prof.dr. E.B. Wolvius	Erasmus MC
Dr. J. Jeffers	Imperial College London

Content

Summary

Without our musculoskeletal system, which consists of bones, joints, and muscles, we would not be able to live. Our bones are responsible for the protection of our organs, the support of our body, and they enable our mobility. Therefore, it is important to keep them healthy. This is done by cells who repair small cracks and fractures caused by our daily activities through continuous remodeling of the skeleton. However, severe bone damage and defects can occur, for example, due to trauma (*e.g.*, car accidents) and bone tumor resection. In this case, the defects are too large for the cells to repair and surgical intervention is required to support the bone regeneration process. Bone substitutes or porous biomaterials are used to fill these defects to help the cells to regenerate the bone.

Bone substitutes require implantation via open surgery due to their large dimensions and rigidity. This causes great damage to the body, which results in a long recovery time for the patient and increases the risk of infections. To reduce the invasiveness of the implantation process, minimally invasive surgery (MIS) could be used. MIS techniques make it possible to perform surgical treatments through specific minimally invasive tools that are inserted into the body through small incisions. In order to make minimally invasive implantation possible, the dimensions of porous biomaterials should be reduced to fit through these small incisions.

In addition, it has been demonstrated that the bone regeneration process can be optimized and infections could be prevented by applying precisely controlled nanopatterns to the surface of bone substitutes. However, surface patterning techniques can only be applied to flat surfaces. Therefore, it is not possible to apply surface patterns to the inner surfaces of three-dimensional porous structures, such as those fabricated through 3D printing techniques.

To resolve these two issues, biomaterials could be made deployable and be folded from flat sheets to simultaneously enable the use of MIS and surface patterning techniques. Because neither deployable nor foldable biomaterials have been developed before, the aim of this thesis is to explore the feasibility of making porous biomaterials deployable and foldable from a flat state.

In order to understand the important architectural parameters of porous biomaterials and their effect on the bone regeneration process, a literature review was conducted in Chapter 2.

In Chapter 3, rigid metallic porous biomaterials based on four different types of minimal surfaces were designed using a three-dimensional computer models. Computer models allow for the design of porous biomaterials with the desired properties for the application as bone substitutes. These computer models were used to manufacture the rigid porous biomaterials using selective laser melting (SLM), which is an additive manufacturing (=3D

printing) technique to build metal objects. This enabled us to evaluate the mechanical (*i.e.*, quasi-static mechanical properties and fatigue behavior) and mass transport properties of solid free-form fabricated porous biomaterials.

Although the porous structures presented in Chapter 3 offer a unique combination of mechanical and mass transport properties, they are not suitable to be implanted using MIS procedures. Therefore, a first step towards deployable metallic biomaterials is made in Chapter 4. This chapter presents deployable non-assembly mechanisms, which were manufactured using SLM. Different geometries consisting of revolute joints, wavelike elements, and rigid rods were assembled into structures that could be deployed and retracted by applying compressive or tensile forces to their proximal and distal vertices.

The revolute joints in the deployable non-assembly mechanisms presented in Chapter 4 complicate the design of deployable porous biomaterials. Therefore, they were eliminated from our deployable designs presented in Chapter 5. Bi-stable elements were printed using fused deposition modeling (FDM). The bi-stable elements were combined in various ways to make multi-stable structures that can be deployed in different ways.

Although the multi-stable structures developed in Chapter 5 were deployable, their three-dimensional design does not allow for the application of surface patterning techniques. In Chapter 6, the knowledge gained from this study was used to develop deployable and foldable structures. FDM and laser micromachining were used to create three-dimensional deployable cubes. Due to the flat state of the laser-cut metal sheets, it was possible to apply micro-patterns to their surfaces. Moreover, the metal sheets could be folded into three-dimensional deployable configurations.

Chapter 7 summarizes the main findings of the thesis and tries to formulate succinct answers to the primary and secondary research questions presented in Chapter 1. Additionally, recommendations for future research are provided and alternative applications are proposed.

Overall, the work covered by this thesis is the first step towards the development of deployable porous biomaterials, which can be folded from a flat state. We hope that our designs provide inspiration for the further development of such biomaterials and for making them available for the treatment of large bone defects. Such biomaterials should be also compatible with MIS techniques and allow for the application of precisely-controlled surface nanopatterns.

Samenvatting

Zonder ons spierskeletstelse dat bestaat uit botten, gewrichten en spieren, zouden we niet kunnen overleven. Onze botten beschermen onze organen, geven structuur aan ons lichaam en ze maken het mogelijk dat we ons kunnen bewegen. Botcellen zorgen ervoor dat onze botten gezond blijven door kleine scheuren en breuken die veroorzaakt worden door dagelijkse activiteiten te herstellen. Helaas kan het voorkomen dat bottumoren verwijderd moeten worden of dat we ernstig verongelukken waardoor grote botdefecten ontstaan. Deze defecten zijn te ernstig om door onze botcellen hersteld te worden. In dit geval is een operatie nodig om de cellen te ondersteunen bij het botherstel. Botvervangers kunnen in het defect geplaatst worden om een brug te vormen tussen de twee uiteinden van het defect en zorgen ervoor dat cellen gestimuleerd worden om nieuw botweefsel te vormen.

De afmetingen van de beschikbare botvervangers voor de behandeling van botdefecten zorgen ervoor dat deze implantaten alleen in een defect geplaatst kunnen worden via een open operatie. Zo'n operatie veroorzaakt grote schade aan het lichaam wat leidt tot een langdurig herstelproces en het vergroot de kans op infecties. Minimaal invasieve chirurgie zou toegepast kunnen worden om de operatie minder ingrijpend te maken. Met deze techniek kunnen operaties uitgevoerd worden met speciale instrumenten die door kleine sneden in het lichaam worden gebracht. Om minimaal invasieve implantatie van botvervangers mogelijk te maken, zouden botimplantaten gemaakt moeten worden die door deze kleine openingen passen. Daarnaast is het bewezen dat het botherstel bevorderd kan worden en infecties voorkomen kunnen worden door specifieke nano-patronen op het oppervlak van een botvervanger aan te brengen. Helaas is het niet mogelijk om de technieken die hiervoor gebruikt worden toe te passen op de beschikbare botimplantaten vanwege hun drie-dimensionele structuur. Om deze twee problemen op te lossen zouden botvervangers uitklapbaar gemaakt kunnen worden en gevouwen kunnen worden vanuit een twee-dimensionele geometrie. Omdat uitklapbare en vouwbare botvervangers niet bestaan, is het doel van dit proefschrift om uit te zoeken of het mogelijk is om uitklapbare botvervangers te maken en deze te vouwen van vlakke platen.

In hoofdstuk 2 worden verschillende aspecten van de geometrie van een botvervanger onderzocht om erachter te komen hoe deze het botherstel beïnvloeden.

In hoofdstuk 3 worden poreuze structuren met een specifieke geometrie gepresenteerd die ontworpen zijn met computermodellen. Een 3D-printtechniek dat selective laser melting heet, werd gebruikt om deze poreuze structuren te fabriceren op basis van de computermodellen. Evaluatie van hun mechanische eigenschappen en hun doorlaatbaarheid geeft ons een idee van de eigenschappen van botvervangers die ontworpen zijn met volledige controle over hun geometrie.

Ondanks de gewenste eigenschappen die de poreuze structuren in hoofdstuk 3 hebben, zijn ze niet geschikt om ze met minimaal invasieve technieken te kunnen implanteren. Daarom wordt een eerste stap gemaakt in de ontwikkeling van metalen uitklapbare botvervangers in hoofdstuk 4. In dit hoofdstuk worden mechanismen ontworpen die direct na hun fabricage met selective laser melting functioneel zijn. Dankzij scharnieren, verende elementen en staven kunnen deze mechanismen in- en uitgeklapt worden door op specifieke punten trek- en drukkrachten uit te oefenen.

De scharnieren die gebruikt worden voor de uitklapbare mechanismen in hoofdstuk 4 compliceren het ontwerp. Daarom worden in hoofdstuk 5 simpele structuren 3D-geprint die geen scharnieren bevatten maar op basis van elastische vervorming kunnen wisselen tussen twee verschillende stabiele configuraties. Deze simpele structuren kunnen op verschillende manieren samengesteld worden om uitklapbare structuren te vormen die meerdere stabiele configuraties hebben.

De structuren in hoofdstuk 5 kunnen ingeklapt en uitgeklapt worden, maar vanwege hun drie-dimensionele geometrie zijn ze niet geschikt om oppervlaktebehandelingen toe te passen. De kennis die we tijdens dit onderzoek hebben opgedaan is gebruikt voor de ontwikkeling van uitklapbare en vouwbare structuren die gepresenteerd worden in hoofdstuk 6. 3D-printen en het lasersnijden van metalen platen worden gebruikt om drie-dimensionele uitklapbare kubussen te maken. Dankzij de vlakke configuratie van de lasergesneden metalen platen konden micro-patronen aangebracht worden op het oppervlak. Ook kunnen de gesneden platen gevouwen worden om drie-dimensionele uitklapbare botvervangers te maken.

In hoofdstuk 7 worden de belangrijkste bevindingen van dit proefschrift besproken en worden de onderzoeksvragen uit hoofdstuk 1 beantwoord. Daarnaast worden er aanbevelingen gedaan voor toekomstige onderzoeken en alternatieve toepassingen voorgesteld.

Het werk dat gepresenteerd is in dit proefschrift is de eerste stap in de ontwikkeling van uitklapbare botvervangers en uitklapbare botvervangers die gevouwen kunnen worden van vlakke platen. We hopen dat onze ontwerpen inspireren voor de verdere ontwikkeling om botvervangers geschikt te maken voor minimaal invasieve chirurgie en oppervlaktebehandelingen toepasbaar te maken voor uitklapbare drie-dimensionele structuren.

1

Introduction

Science and art sometimes can touch one another,
like two pieces of the jigsaw puzzle which is our human life,
and that contact may be made across the borderline
between the two respective domains.

-M. C. Escher

1.1 Background

Our bodies can be seen as magical worlds in which trillions of cells live and work together. These cells are responsible for many processes to make our organs and tissues function properly.

Our musculoskeletal system, which consists of bones, joints, and muscles, fulfils several important functions. For example, our bones are responsible for the support and protection of our organs while enabling our mobility. Therefore, it is important to keep them healthy. This is done by cells who repair small cracks and fractures caused by our daily activities. However, severe bone damage and large bony defects can occur due to different reasons, such as bone tumor resection or car accidents. In many such cases, the defects are too large for the cells to repair on their own and surgical intervention is required to support the bone regeneration process.

A bone substitute can be implanted into the defect to replace the lost bone and to act as a bridge between both parts of the native bone on either side of the defect. Cells are then able to move into the bone substitute to form new bone and to integrate the newly formed bone with the native bone. To ensure successful bone regeneration, it is important that the bone substitutes satisfy a long list of requirements, including biocompatibility and bioactivity, while also providing specific mechanical functions and favorable mass transport properties. Since this is not an easy task, many studies have been performed to develop bone substitutes, which fulfil those requirements.

1.2 Bone structure and the remodeling process

Bone is organized into multiple levels of structural hierarchy (*i.e.*, macrostructure, microstructure, sub-microstructure, nanostructure, and sub-nanostructure [1]). At the macroscale, bone can be divided into cortical (or compact) bone and trabecular (or cancellous) bone [1, 2]. The stiffer and denser cortical bone can be found in 80% of a mature skeleton [3], while a combination of cortical and porous, spongy trabecular bone can be found in long and flat bones [1, 3, 4]. Cortical bone primarily consists of osteons, which are cylindrical structures that are aligned in parallel with the longitudinal axis of bones [3]. Trabecular bone is made up of trabeculae, which are connected struts that form an efficient porous network to support the mechanical loads exerted on the bones [3-5].

Bone remodeling is required for the growth of the skeleton [8], to optimize the inner architecture of bones in order to support mechanical loads [3, 6], and to maintain calcium and phosphorous levels inside the body [2, 3]. The most important cells in this process are osteoclasts [7] and osteoblasts [7], whose roles are bone resorption and bone formation [6], respectively. In addition to those two cell types, osteocytes are crucial for a process called mechanotransduction [3, 6, 7]. This is a mechanism in which mechanical stresses are converted into biochemical signals. These signals are then used to regulate the osteoblast

and osteoclast activity [3].

Although microdamage can be repaired by bone remodeling [9], the repair of large (*i.e.*, critical size) bony defects, caused by accidents for example, require surgical intervention. As a rule of thumb, a defect is considered large when the length of the defect is 2-3 times the diameter of the bone involved [10]. This means that, for example, defects larger than 3 cm in the bones of our lower arm, 5 cm in the bones of our legs, and 6 cm in the bone of our upper arm [10] cannot be repaired by our cells alone. Bone tissue engineering aims at the repair and regeneration of such large bone defects [2] by using biomaterials to integrate the newly formed bone w the native bone [2].

1.3   Biomaterials

Bone substituting materials are used to fill large bony defects. Bone substitutes, such as autologous (from the same patient) and allogenic (from another person) bone tissue grafts are available. However, their limited supply [11-13], donor site morbidity [11, 13], and the risk of viral and bacterial disease transmission [11, 14] means that there is a need for engineered and innovative replacements [11, 12].

Synthetic replacements for bone grafts are called porous biomaterials. These biomaterials can be made of ceramics [7, 13], polymers [7, 13], or metals [15-18] and their alloys. They aim to help and guide our cells in the bone regeneration process [19]. Biomaterials should be biocompatible so that they are not harmful for the cells and tissues in our body [20].

1.3.1   Biomaterial architecture

To make sure that our cells receive the nutrients and oxygen they require to survive and function as desired, the architecture of a biomaterial is important. Architectural parameters include the pore size [2, 21] and shape, the overall porosity of the biomaterial [2, 21], surface properties [2, 21], and mechanical properties [2, 21]. When the architecture is not optimal for the cells to live in, the bone regeneration process will be obstructed and the connection between the implant and the native bone will be too weak. The biomaterial remains or becomes loose and needs to be surgically removed and replaced. Therefore, a biomaterial should promote cells to become bone cells (osteoinduction) [7, 22], support bone growth (osteoconduction) [7, 22], and be able to integrate with the native bone (osseointegration) [7]. The porosity, pore size, and the pore interconnectivity of bone substitutes are important to enable cells to travel through the biomaterial [2] and native bone and blood vessels [2] to grow into the porous structure. These events are necessary for the generation of *de novo* bone that integrates with the existing tissue.

1.3.2   Biomaterial surface

The surface of a porous biomaterial is important, because the surface properties determine the cell response [7, 15]. Modifications to the surface, such as the application of nanopatterns [15, 23, 24] can induce cells to adhere to the surface, which is important for cells to travel through the implant (migration), to multiply (proliferation) [23, 24], and to specialize (*i.e.*, differentiate) into the type of cells required for bone tissue regeneration [15, 24]. For bone implants, it is desired that the cells on the surface of the implant become bone cells. In addition to inducing bone formation, surfaces can be made antimicrobial [25, 26] to prevent serious infections, which can lead to implant failure.

3D printing or additive manufacturing (AM) has been recently used to manufacture complex and porous biomaterials [27-29]. Such biomaterials contain a large area of internal surfaces, which cannot be easily reached after fabrication. The main reason for this is that controlled surface patterning techniques can only be applied to flat surfaces [7, 30].

1.4   Minimally invasive surgery

Due to the dimensions and rigidity of available porous biomaterials, open surgery is commonly used for the treatment of large bone defects. A large incision is made to place the implant at the right location. This is a highly invasive process, which increases the risk of infections and is associated with long recovery times.

Minimally invasive surgery was introduced at the beginning of the 20th century [31]. For this type of surgery, incisions of 1- 1.5 centimeters [32] are made to insert laparoscopic tools. Using these long cylindrical tools with a small camera, many treatments are performed on a daily basis. Minimally invasive surgery is applied to treat vascular diseases [33], to remove tumors from the brain [34], and to take biopsies [35]. In addition to these examples, many other treatments have been performed using this surgery technique.

It is a challenging task to implant bone substitutes minimally invasively because biomaterials are in general rigid structures with large dimensions. Therefore, they cannot be deformed easily to fit through small incisions or to be placed at locations that are difficult to reach. To overcome these issues, biomaterials could be made deployable.

1.5   Deployable structures

Deployable structures are structures that, upon deployment, can change their configuration from a compact state to their operational configuration [36, 37]. This enables deployable structures to be transported in a compact way [37]. Deployability is used for the transportation of antennas, solar panels, and masts into space [38], to carry an umbrella inside a bag [37], or to quickly place a temporary bridge to recover damaged infrastructures caused by natural disasters [39]. Deployable structures can be designed using mechanical joints and rigid

elements [38], elastic deformation, or plastic deformation.

1.5.1   Rigid assemblies

Rigid assemblies are deployable structures that consist of mechanical joints and rigid elements [38]. An example of a deployable rigid assembly is an umbrella. An external force is required to change its configuration from retracted (closed) to deployed (open). A locking mechanism is integrated to keep the umbrella in its deployed configuration.

1.5.2   Elastic deformation

Deployable structures can also be made using elastic deformation. This kind of deformation happens in the elastic range of the material. Elastic deformations can be made undone when the external force is removed.

Elastic deformation can also occur in bi-stable and multi-stable structures, which have more than one stable configuration in which they are load-bearing. An external force is only required to elastically deform the structures locally to make them switch between the stable configurations.

1.5.3   Plastic deformation

In addition to elastic deformation, deployable structures can work on the basis of plastic deformation. Unlike elastic deformation, which enables a material or a structure to return to its original shape when the external force is removed, plastic deformation results in a permanent shape transformation. An example of deployable structures that are plastically deformed are stents used for coronary balloon angioplasty [40]. Stents are placed inside a narrowed artery using minimally invasive surgery. A balloon may then be used to open the stent and to plastically deform the stent, thereby keeping the artery open [40].

To summarize, deployable implants can be made using mechanical joints and elastic deformation, which allow them to switch between different stable configurations. Plastic deformation on the other hand, can be used to deform structures or materials permanently.

1.6   Problem statement

The dimensions and rigidity of the available porous biomaterials for the treatment of large bone defects require implantation using open surgery. This may cause great damage to the body, resulting in a long recovery time for the patient and increasing the risk of infections.

Moreover, it has been demonstrated that the bone regeneration process can be improved by applying complex and precisely-controlled nanopatterns to the surface of bone substitutes. However, due to the three-dimensional nature of the available porous

biomaterials, many surface patterning techniques cannot be used because they can only be applied to flat surfaces.

To resolve these two issues, porous biomaterials could be made deployable and be folded from a flat state to enable the application of minimally invasive procedures and the use of surface patterning techniques.

1.7   Aim and research questions

Because neither deployable nor foldable biomaterials have been developed before, the aim of this thesis is to explore the feasibility of making porous biomaterials deployable and foldable from a flat state. More specifically, the central research question addressed in this thesis is defined as:

Is it feasible to fold deployable biomaterials from a flat state which can be used for the treatment of large bone defects?

The following sub-research questions were addressed to answer the main research question:

- *What are the main requirements for bone substitutes in terms of their geometry, mechanical properties, and mass transport properties and to what extent do existing designs and manufacturing techniques (e.g., 3D printing) achieve those properties?*
- *How can mechanical joints and elastic deformation be used to develop deployable porous biomaterials?*
- *How can elastic deformation be used to develop deployable porous biomaterials?*
- *How can deployable porous biomaterials be made foldable in order to apply precisely controlled patterns to their surfaces?*

In this thesis, different manufacturing techniques, materials, and designs were used and evaluated to explore the feasibility of making porous biomaterials deployable and foldable from a flat state.

1.8   Thesis outline

This thesis consists of seven chapters in total, including the Introduction (Chapter 1) and the General Discussion and Conclusion (Chapter 7). Chapter 2 and 3 adress the first sub-research question and each of the remaining chapters addresses one of the other sub-research questions.

To gain more knowledge about the important architectural parameters of porous biomaterials and their effect on the bone regeneration process, a literature review is

presented in Chapter 2.

To evaluate the properties of rigid porous biomaterials of which the geometry can be fully controlled, four types of rigid porous biomaterials are presented in Chapter 3. These porous biomaterials were manufactured using selective laser melting (SLM), which is a 3D printing or additive manufacturing (AM) technique to build metal objects through in a layer-by-layer fashion. The fabricated biomaterials were evaluated in terms of their morphological, mechanical (both quasi-static and fatigue), and mass transport properties.

Although the porous structures presented in Chapter 3 offer unique combinations of mechanical and mass properties, they are not suitable to be implanted using minimally invasive procedures. Therefore, a first step towards deployable metallic biomaterials is made in Chapter 4. This chapter presents deployable non-assembly mechanisms, which were manufactured using SLM. Different geometries, including a bicapped cube, a bicapped square antiprism, and a bicapped trigonal antiprism, were designed and fabricated using a single-step fabrication process. This type of fabrication leads to the immediate functionality of the mechanisms after manufacturing. The structures consist of revolute joints, wavelike elements, and rigid rods. Moreover, they can be deployed and retracted when compressive and tensile forces are applied to some specific locations within the mechanisms.

The mechanisms presented in Chapter 4 include revolute joints, which complicate the design of deployable porous biomaterials. For this reason, elastic deformation was used to design multi-stable deployable structures in Chapter 5. In this way, revolute joints could be avoided to simplify the design. Bi-stable elements were manufactured using fused deposition modeling (FDM), which is an AM technique to fabricate polymer objects. The bi-stable elements were combined in various ways to make multi-stable structures, which can be deployed and retracted in different ways.

Although the bi-stable and multi-stable structures presented in Chapter 5 were deployable, their three-dimensional design did not allow for the application of surface patterns. The knowledge gained from the study in Chapter 5 was used for the development of the deployable and foldable structures presented in Chapter 6. FDM was used to manufacture panels with bi-stable elements, which were combined to assemble deployable cubes. In addition to these 3D printed structures, micromachining was used to cut unfolded cubes from metal sheets. Due to the flat state of the unfolded cubes, it was possible to apply micropatterns to their surfaces. Moreover, they could be folded into a 3D deployable cube. Silicone balloons were designed and manufactured to act as actuators for the deployment of the cubes.

Chapter 7 summarizes the most important findings of this thesis and tries to formulate succinct answers to the research questions presented in the introduction. Additionally, recommendations for future research are provided and alternative applications are proposed.

References

[1] J.-Y. Rho, L. Kuhn-Spearing, P. Zioupos, Mechanical properties and the hierarchical structure of bone, Medical engineering & physics 20(2) (1998) 92-102.

[2] A.R. Amini, C.T. Laurencin, S.P. Nukavarapu, Bone tissue engineering: recent advances and challenges, Critical Reviews™ in Biomedical Engineering 40(5) (2012).

[3] J.D. Black, B.J. Tadros, Bone structure: from cortical to calcium, Orthopaedics and Trauma (2020).

[4] T.M. Keaveny, E.F. Morgan, G.L. Niebur, O.C. Yeh, Biomechanics of trabecular bone, Annual review of biomedical engineering 3(1) (2001) 307-333.

[5] C.H. Turner, Three rules for bone adaptation to mechanical stimuli, Bone 23(5) (1998) 399-407.

[6] S. Tatsumi, K. Ishii, N. Amizuka, M. Li, T. Kobayashi, K. Kohno, M. Ito, S. Takeshita, K. Ikeda, Targeted ablation of osteocytes induces osteoporosis with defective mechanotransduction, Cell metabolism 5(6) (2007) 464-475.

[7] J. Mitra, G. Tripathi, A. Sharma, B. Basu, Scaffolds for bone tissue engineering: role of surface patterning on osteoblast response, Rsc Advances 3(28) (2013) 11073-11094.

[8] A. Salhotra, H.N. Shah, B. Levi, M.T. Longaker, Mechanisms of bone development and repair, Nature Reviews Molecular Cell Biology (2020) 1-16.

[9] E.F. Eriksen, Cellular mechanisms of bone remodeling, Reviews in Endocrine and Metabolic Disorders 11(4) (2010) 219-227.

[10] S. Stewart, S.J. Bryant, J. Ahn, K.D. Hankenson, Bone regeneration, translational regenerative medicine, Elsevier2015, pp. 313-333.

[11] C. Laurencin, Y. Khan, S.F. El-Amin, Bone graft substitutes, Expert review of medical devices 3(1) (2006) 49-57.

[12] Y. Yu, Y. Wang, W. Zhang, H. Wang, J. Li, L. Pan, F. Han, B. Li, Biomimetic periosteum-bone substitute composed of preosteoblast-derived matrix and hydrogel for large segmental bone defect repair, Acta biomaterialia 113 (2020) 317-327.

[13] M.M. Stevens, Biomaterials for bone tissue engineering, Materials today 11(5) (2008) 18-25.

[14] C. Delloye, Tissue allografts and health risks, Acta orthopaedica Belgica 60 (1994) 62-67.

[15] A.I. Greer, V. Goriainov, J. Kanczler, C.R. Black, L.-A. Turner, R.M. Meek, K. Burgess, I. MacLaren, M.J. Dalby, R.O. Oreffo, Nanopatterned titanium implants accelerate bone formation in vivo, ACS applied materials & interfaces 12(30) (2020) 33541-33549.

[16] Y. Li, H. Jahr, K. Lietaert, P. Pavanram, A. Yilmaz, L. Fockaert, M. Leeflang, B. Pouran, Y. Gonzalez-Garcia, H. Weinans, Additively manufactured biodegradable porous iron, Acta biomaterialia 77 (2018) 380-393.

[17] Y. Li, J. Zhou, P. Pavanram, M. Leeflang, L. Fockaert, B. Pouran, N. Tümer, K.-U. Schröder, J. Mol, H. Weinans, Additively manufactured biodegradable porous magnesium, Acta biomaterialia 67 (2018) 378-392.

[18] Y. Li, P. Pavanram, J. Zhou, K. Lietaert, P. Taheri, W. Li, H. San, M. Leeflang, J. Mol, H. Jahr, Additively manufactured biodegradable porous zinc, Acta Biomaterialia 101 (2020) 609-623.

[19] T. Winkler, F. Sass, G. Duda, K. Schmidt-Bleek, A review of biomaterials in bone defect healing, remaining shortcomings and future opportunities for bone tissue engineering: The unsolved challenge,

Bone & joint research 7(3) (2018) 232-243.

[20] L. Ghasemi-Mobarakeh, D. Kolahreez, S. Ramakrishna, D. Williams, Key terminology in biomaterials and biocompatibility, Current Opinion in Biomedical Engineering 10 (2019) 45-50.

[21] G. Turnbull, J. Clarke, F. Picard, P. Riches, L. Jia, F. Han, B. Li, W. Shu, 3D bioactive composite scaffolds for bone tissue engineering, Bioactive materials 3(3) (2018) 278-314.

[22] T. Albrektsson, C. Johansson, Osteoinduction, osteoconduction and osseointegration, European spine journal 10(2) (2001) S96-S101.

[23] L. Richert, F. Vetrone, J.H. Yi, S.F. Zalzal, J.D. Wuest, F. Rosei, A. Nanci, Surface nanopatterning to control cell growth, Advanced Materials 20(8) (2008) 1488-1492.

[24] J. Hasan, S. Jain, K. Chatterjee, Nanoscale topography on black titanium imparts multi-biofunctional properties for orthopedic applications, Scientific reports 7(1) (2017) 1-13.

[25] M. Ganjian, K. Modaresifar, M.R. Ligeon, L.B. Kunkels, N. Tümer, L. Angeloni, C.W. Hagen, L.G. Otten, P.L. Hagedoorn, I. Apachitei, L.E. Fratila-Apachitei, A.A. Zadpoor, Nature helps: Toward bioinspired bactericidal nanopatterns, Advanced Materials Interfaces 6(16) (2019) 1900640.

[26] J. Hasan, R.J. Crawford, E.P. Ivanova, Antibacterial surfaces: the quest for a new generation of biomaterials, Trends in biotechnology 31(5) (2013) 295-304.

[27] S. Arabnejad, R.B. Johnston, J.A. Pura, B. Singh, M. Tanzer, D. Pasini, High-strength porous biomaterials for bone replacement: A strategy to assess the interplay between cell morphology, mechanical properties, bone ingrowth and manufacturing constraints, Acta biomaterialia 30 (2016) 345-356.

[28] G. Campoli, M. Borleffs, S.A. Yavari, R. Wauthle, H. Weinans, A.A. Zadpoor, Mechanical properties of open-cell metallic biomaterials manufactured using additive manufacturing, Materials & Design 49 (2013) 957-965.

[29] J. Kadkhodapour, H. Montazerian, A.C. Darabi, A. Anaraki, S. Ahmadi, A. Zadpoor, S. Schmauder, Failure mechanisms of additively manufactured porous biomaterials: Effects of porosity and type of unit cell, Journal of the mechanical behavior of biomedical materials 50 (2015) 180-191.

[30] V.A. Bolaños Quiñones, H. Zhu, A.A. Solovev, Y. Mei, D.H. Gracias, Origami biosystems: 3D assembly methods for biomedical applications, Advanced Biosystems 2(12) (2018) 1800230.

[31] S.D.S. Peter, G.W. Holcomb III, History of minimally invasive surgery, Atlas of Pediatric Laparoscopy and Thoracoscopy (2008) 1.

[32] G. Li, S.K. Ling, H.A. Li, Y. Zhang, J. Hu, How to perform minimally invasive tibial cortex transverse transport surgery, Journal of Orthopaedic Translation (2020).

[33] D.L. Fischman, M.B. Leon, D.S. Baim, R.A. Schatz, M.P. Savage, I. Penn, K. Detre, L. Veltri, D. Ricci, M. Nobuyoshi, A randomized comparison of coronary-stent placement and balloon angioplasty in the treatment of coronary artery disease, New England Journal of Medicine 331(8) (1994) 496-501.

[34] Y. Kim, S.S. Cheng, M. Diakite, R.P. Gullapalli, J.M. Simard, J.P. Desai, Toward the development of a flexible mesoscale MRI-compatible neurosurgical continuum robot, IEEE Transactions on Robotics 33(6) (2017) 1386-1397.

[35] S.H. Parker, F. Burbank, A practical approach to minimally invasive breast biopsy, Radiology 200(1) (1996) 11-20.

[36] A. Al Sabouni-Zawadzka, A. Zawadzki, W. Gilewski, Modern lightweight deployable engineering

structures.

[37] S. Pellegrino, Deployable structures, Springer2014.

[38] G. Kiper, E. Soylemez, Deployable space structures, 2009 4th International Conference on Recent Advances in Space Technologies, IEEE, 2009, pp. 131-138.

[39] I. Ario, M. Nakazawa, Y. Tanaka, I. Tanikura, S. Ono, Development of a prototype deployable bridge based on origami skill, Automation in construction 32 (2013) 104-111.

[40] G.P. Kumar, S. Yuan, F. Cui, P.S. Branicio, M. Jafary-Zadeh, Nanoglass-based balloon expandable stents, Journal of Biomedical Materials Research Part B: Applied Biomaterials 108(1) (2020) 73-79.

2

The effects of the bone substitute architecture on the bone regeneration process

The success of bone substitutes used to repair bone defects such as critical sized defects depends on the architecture of the porous biomaterial. The architectural parameters and surface properties affect the cell seeding efficiency, cell response, angiogenesis, and eventually bone formation. The relevant parameters include the pore size and porosity, pore shape and fiber orientation, surface properties, and mechanical properties. For example, small pores are preferable for cell seeding, but limit cell viability, cell proliferation and differentiation. Moreover, the pore size and geometry affect the alignment of cells and the structure of the regenerated bone. This chapter presents an overview of the effects of the architecture of a porous biomaterial on the cell seeding efficiency, cell response, angiogenesis, and bone formation.

2.1 Introduction

Bone substitutes act as three-dimensional matrices that guide and promote bone regeneration in order to heal critical sized defects [1–3]. In these defects caused by trauma [4], tumor resection [4,5], or severe fracture [5,6], bone is unable to heal itself. The most common bone substitutes include autografts [7,8], allografts [8], and xenografts [8], which are pieces of bone removed from the body of the patient, another person, or an animal, respectively [8]. Because the use of these biological grafts may result in damage to the body and their supply is limited, another solution has to be found [7]. Therefore, new synthetic biocompatible porous materials are developed. These biocompatible materials could also be called biomaterials and are not harmful or toxic to living cells and tissues inside the body [9].

Depending on the biomaterial used (polymer, ceramic, or metal) (Table 1), different fabrication techniques could be applied to manufacture the designed porous biomaterials. For metal bone substitutes, selective laser melting (SLM) [10–16], selective laser sintering (SLS) [17], sintering [18], perforating titanium sheet [14] and capsule-free hot isostatic pressing (CF-HIP) [19] are some examples of the applicable production methods. Polymer and ceramic bone substitutes could be manufactured with porogen leaching [20–30], freeze drying [31], 3D printing of successive fiber/strut layers [32–36], electrospinning [37], or gas foaming [1,38]. The above-mentioned techniques vary in accuracy and the level of control

Biomaterial abbreviation	Full form of biomaterial	Biomaterial group
CaP	Calcium Phosphate	Ceramic
HA	Hydroxyapatite	Ceramic
MBG	Mesoporous bioactive glass	Ceramic
β-TCP	β-tricalcium phosphate	Ceramic
Ti6Al4V	Titanium	Metal
TiNi	Titanium Nickel	Metal
TT	Trabecular titanium	Metal
CSNF	Chitosan network fibers	Polymer
Col	Collagen	Polymer
CG	Collagen-glycosaminoglycan	Polymer
DEF	diethyl fumarate	Polymer
HFIP	hexafluoroisopropanol	Polymer
PA	polyacrylamide	Polymer
PDMS	poly(dimethylsiloxane)	Polymer
PLGA	Poly(lactide-co-glycolide)	Polymer
PPC	poly(propylene carbonate)	Polymer
PPF	poly(propylene fumarate)	Polymer
PCL	poly(ε-caprolactone)	Polymer
SF	Silk fibroin	Polymer
SPCL	Starch poly(ε-caprolactone)	Polymer
TG	thermoplastic gelatin	Polymer
TPU	Thermoplastic polyurethane	Polymer
PDLLA	poly(D,L-lactic acid)	Polymer

Table 1. Biomaterials abbreviations and material group.

over the parameters that describe the architecture of the scaffold.

A lot of research has been undertaken to see how the architectural parameters and surface properties of a developed bone substitute influence the bone regeneration process. Parameters determining the performance of porous biomaterials for bone tissue engineering include pore size [39–43], pore shape [32,41,43], porosity [39,41,43,44], interconnectivity [39,42,43], fiber orientation [32], surface properties [2,39,45,46], and mechanical properties [39,40]. The design of biomimetic materials affects cell behavior and provides guidance during tissue regeneration. Therefore, the design parameters can be chosen such that the desired cell response is elicited and the formation and structure of the new bone is guided.

Bone formation occurs in several steps starting with cell seeding [47] or recruitment of stem cells. In the case of cell seeding, the cell seeding efficiency can be measured, which is the number or percentage of attached cells within the structure after a cell suspension is seeded [47]. Cell viability is important in all stages of bone regeneration and depends on the availability of nutrients [48] and oxygen for the cells within a structure, as well as on waste removal [49].

Cells should be able to migrate and distribute throughout the structure to ensure a stable bone-implant fixation and bone formation within the structure. The migration of cells is a stepwise process. First, the lamellipodia and filopodia protrude at the front of the cell and adhere to the surface of the biomaterial, which is called focal adhesion [50]. The cell pulls itself forward by releasing the adhesions at its back side and contracting its body [51]. The strength of the focal adhesions influences the cell morphology [52] and is thought to determine cell response and gene expression [53–55].

During bone regeneration, cells proliferate and differentiate into osteoblasts which deposit a collagen matrix that becomes mineralized. The first stage (i.e., proliferation) takes place in the first days after seeding and consists mainly of cell division [56]. During this stage, cells are still able to migrate [56]. After proliferation, cells start to differentiate into osteoprogenitor cells until the end of the second week, and the release of alkaline phosphatase (ALP) increases [57,58]. In two weeks after the differentiation stage, osteocalcin (OCN) and osteopontin (OPN) are produced and secreted by the cells [57,58], indicating the presence of osteoblasts [57,58] (Table 2). When the collagen matrix is synthesized by osteoblasts [59], biomineralization is initiated and mineral crystals are formed within the collagen matrix [55]. In parallel with the proliferation and differentiation of cells, blood vessels form from existing vessels (angiogenesis) [60]. These vessels create a vascular network to provide oxygen and nutrients to the cells and developing tissue within the bone substitute [60]. This network provides stem cells needed for bone regeneration and direct the differentiation of endothelial cells and pre-osteoblasts [61,62]. All these steps in the bone regeneration process and the architecture of the bone substitute determine the amount and the quality of the newly formed bone.

Understanding the effects of the architecture of a bone substitute on the cell response is important to optimize the design of porous biomaterials that are aimed for bone regeneration. This paper presents an overview of the effects of various architectural parameters and surface properties on the cell seeding efficiency, cell response, angiogenesis, and bone formation. The seeded cell types were mainly BMSCs, (pre) osteoblasts, and fibroblasts. Only in a limited number of cases the cell behavior seemed to depend on the type of seeded cells [63–65].

Marker abbreviation	Full form of marker	Expressed by
ALP	Alkaline phosphatase	Osteoprogenitor
RunX-2		Osteoprogenitor, osteoblast
OPN	Osteopontin	Osteoblast
OCN	Osteocalcin	Osteoblast
OPG	Osteoprotegerin	Osteoblast, inhibits bone resorption
Calcium		Osteoblast
Col1	Collagen type 1	Organic matrix of bone, synthesized by osteoblasts
VEGF	Vascular endothelial growth factor	Growth factor blood vessels
BSP	Bone sialoprotein	Mineralized tissue

Table 2. Osteogenic markers.

2.2 Pore size and porosity

Pores are the voids within a porous biomaterial which provide space where new tissue and blood vessels will grow [66,67]. The pore size (diameter of an individual void) and porosity (percentage of void volume within a porous biomaterial) are connected to each other when the bone substitute contains an interconnected pore network. An increase in pore size has been associated with an increased porosity in most studies. Increasing the porosity of a porous bone substitute is a way to lower the stiffness [68]. This reduces the mismatch between the stiffness of a (metal) bone substitute and the host bone [69], thereby mitigating the problems associated with stress shielding [70].

2.2.1 Seeding efficiency

The seeding efficiency (Table 3) depends on the number of attachment sites within a porous biomaterial and the available time for cells to attach to the surface [12]. With an increased pore size, the surface area within the structure decreases, resulting in less attachment sites for the seeded cells [20,31]. In addition to the lower number of attachment sites caused by bigger pores and a higher porosity, the permeability of the porous biomaterial increases [12]. A higher permeability value is associated with a higher flow rate, which reduces the time for cell attachment to the surface of the structure during seeding [12].

Several studies have shown that the seeding efficiency decreases as the pore size increases, regardless of the biomaterial or seeding cells used [1,12,38,44,71]. Cells are more likely to aggregate at the seeding surface of poly(e-caprolactone) (PCL) porous biomaterials with pores smaller than 84 μm [71]. This results in an inhomogeneous distribution of cells throughout the structure [71]. In structures with bigger pores (*e.g.*, 116 μm), cells are able to penetrate the top surface and distribute homogeneously throughout the scaffold [71]. However, when pores become larger (>162 μm), cells tend to escape from the structure [71]. In a study by Salerno *et al.*, PCL structures seeded with hMSCs with a bi-modal architecture (mean pore sizes 38 μm and 312 μm) and a mono-modal structure (mean pore size 325 μm) were compared [38]. They found that cells distributed throughout the bi-modal scaffolds, but that they remained in the seeding region of the mono-modal scaffolds [38]. Studies with silk fibroin (SF) scaffolds found a low seeding efficiency with no difference among scaffolds with pore sizes between 80 and 500 μm [22,23,72].

One explanation for this low seeding efficiency on these scaffolds is their high porosity which ranged between 71% and 96%. In general, small pores are preferable for cell seeding. However, these pores should be larger than 100 μm to make a homogeneous distribution throughout the porous biomaterial possible. Depending on the tortuosity of the void space, there is a limit to the pore size to prevent cell escape which will reduce the seeding efficiency.

2.2.2   Cell viability

Cell viability seems to be mainly affected by the pore size and the porosity of the biomaterial (Table 3). Different studies [1,12,20,31,44,72] found a higher cell viability in porous biomaterials with bigger pores, which can be related to the higher oxygen diffusion into the interior region of these structures [20]. The oxygen diffusion within porous biomaterials with small pores is limited by cell aggregation at the surface and the low penetration level during cell seeding and migration. In decellularized bone scaffolds, no difference in cell viability was found for different pore sizes and porosities [44]. The difference in these findings might be the result of the structure thickness, the pore size and porosity of these porous biomaterials, and the tortuosity of the void network. The porosity (and pore size) of different porous biomaterials varied between 71% and 94% (80–300 μm) (SF) [72], 36–58% (94–147μm) poly(lactide-co-glycolide) (PLGA) [1], 42–87% (500–1000 μm) (Ti6Al4V) [12], and for the decellularized bone substitutes between 70.4% and 88.3% (208–376 μm) [44]. The lower cell viability in the SF [72] (Figure 2h) and PLGA [1] (Figure 2c) scaffolds with small pores can be explained by the pore size which was smaller than 100 μm.In these scaffolds, cells are more likely to aggregate and block the way for oxygen and nutrients to the center of the scaffolds. Based on these results, it could be concluded that pores smaller than 100 μm should be avoided to prevent cell death.

Pore size and porosity

Biomaterial	Seeding cells /implantation site	Pore size [μm] (porosity [%])	Seeding efficiency	Cell viability	Migration	Alignment	Morphology	Proliferation	Osteogenic differentiation	Angiogenesis	Tissue formation	Mineralization	Reference
SF	hMSC	112-224 (94)	+										23
		400-500 (96)	+										
		112-500 (95)	+										
PCL	L929	84	++										71
		116	++										
		141	+				R						
		162	-										
PLGA	3T3 fibroblasts	94 (36)	++	+	++	S/L	S	-					1
		123 (45)	+	+	+	S/L	S	+					
		147 (58)	-	++	+	S	S+	++					
SF	BMSC	80-150 (71)	-	-	-			-	-				72
		150-200 (80)	-	+	+			+	+				
		200-250 (87)	-	+	+			+	+				
		250-300 (94)	-	+	+			+	+				
SF	hASC	140 (76)	+	+	+			+	+		B+	+	22
		254 (87)	+	+	+			+	+		B+	+	
Decellularized bovine bone	hESC	208 (70)	++	+	-			-	+		B	+	44
		315 (80)	+	+	++			+	+		B+	+	
		376 (88)	-	+	+			+	+		B	++	
CG	MC3T3	85	-	-	-		R	-					31
		120	+	+	+			+					
		325	++	++	++			++					
PLGA	MC3T3	100-300	-	-	-		R	-				-	20
		100-400	+	+	+		S	+				+	
		100-500	++	++	+		S	++				++	

Material	Cell / defect	Pore size (µm)	Porosity (%)	Cell response a	Alignment	Morphology	Cell response b	Cell response c	Tissue formation	Angiogenesis	Ref
T6Al4V	hPDC	500		+			−				12
		1000		−			+				
PCL + OM	hBMSC	38, 312		+			++	++*	−	+	38
		325		+			+	+	+	++	
PDLLA	MG63	<275	(87)	−	L	R	+		C−	−	24
		<325	(88)	+	L/S	S	+		C+	+	
		<420	(85)	+	S	S	+		C+	+	
PCL	ASC	355–500	(65)	+	B	R/E	+	+		−	73
		500–1000	(65)	+	B/S	R/E	++	++		+	
		1000–1500	(65)	+	S	S	++	++		++	
PLGA – CaP	rBMSC	470–590	(85)	+			+	+	B+	+	26
	/rat calvarial defect	590–850	(85)	+			+	+	B	−	
		850–1200	(85)	+			++	++	B	−	
PPF/DEF	BMSC	>500		+			+			V+	21
		180–300					−			V	
B-TCP	/rabbit fascia lumbodorsalis	337	(73)						F+	−	27
		415	(74)						F	+	
		557	(71)						F	+	
		631	(72)						F	+	
PLGA	/Rat proximal tibia	100–300	(86)						B	+	81
		300–500	(87)						B+	++	
		500–710	(87)						B	+	
Ti6Al4V	/rat femoral defect	490	(88)						B+		11
		490	(68)						B		

Table 3. The effect of pore size and porosity on cell response, angiogenesis and tissue formation. Alignment: B – bridging, L – loose cells, S – sheet forming. Morphology S – spread, E – elongated, R – round. Angiogenesis: V – VEGF, Tissue formation: B – bone, F – fibrous tissue, C – collagen1. *in vitro* result, *in vivo* result. * after 2 weeks of culture. No significant difference between groups cultured without OM (osteogenic medium).

2.2.3 Cell migration

Cell migration depends on the pore size and porosity of a porous biomaterial (Table 3) [1,20,24,31,38,44,71,72]. Restricted cell migration was observed in porous biomaterials with small pores, while cells can migrate more easily and distribute homogeneously when a structure contains bigger pores up to 500 μm [20,31,44].

2.2.4 Cell alignment and morphology

Table 3 summarizes the results found on cell alignment and morphology (Figure 1). In large pores, cells tend to align with and form sheets on the pore walls [1,24,44,73] while cells are able to bridge smaller pores [69,73]. The sheet formation occurred in PCL scaffolds with pores between 1000 and 1500 μm [73].

In a study on Ti structures with a mean pore size of 425 μm, cells elongated and connected with other cells and the pore walls in pores whose size was between 100 and 150 μm [69]. Pores larger than 200 μm could not be bridged and the cells aligned with the pore surface [69]. No cell growth was found in pores smaller than 100 μm [69].

The sheet-formation of cells could be connected to a well-spread cell morphology [10,19,25,33,72,74] (Figure 1c–f) with filopodia adhered to different points on the pore surface, indicating strong focal adhesions [69,75]. These filopodia help the cell sheets to align within the pores [75]. Cells that bridge small pores or several struts are subjected to higher strains than cells adhered to a single surface, depending on the ratio between the cell size and pore size or the distance between the struts [76]. Cell sheets are formed by filopodia of cells that are connected to neighboring cells, leading to a better communication between the cells [77,78]. Furthermore, a close connection with the pore surface seems to improve the bone regeneration process [73]. By modifying the pore size, the alignment within the pores and the cell morphology could be guided. However, the pore shape and biomaterial used should be taken into account as well.
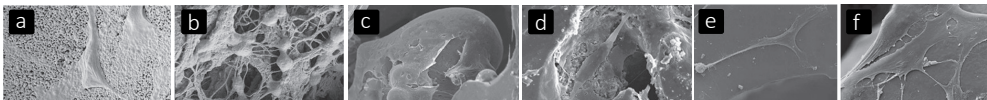
Figure 1: Cell alignment and morphology on different biomaterials with different surfaces and architectures. a) Spreading of BMSCs on surface of HA structures [85] b) BMSCs bridging several collagen fibers within the HA structure [85] c) spreading of osteoblasts and forming sheets on a convex surface in NiTi structures [19] d) osteoblasts adjusting morphology to the roughness of pores in NiTi structures [19] e) stretched morphology of BMSCs on MBG surface after 7 days [74] f) BMSCs show a well spread morphology and connecting to other MBScs after 7 days on MBG structures with a silk film created with a 5.0 % silk solution [74].

2.2.5 Cell proliferation

Cell proliferation depends on the amount of nutrients to produce a new cell and the available space for cells to grow and multiply [69,79]. The pore size and porosity are important to satisfy these requirements, resulting in higher proliferation rates in porous biomaterials with bigger pores and higher porosities [1,12,20,24,31,44,69,72,73] (Table 3). Porous biomaterials with large pores have more space for cell growth and enhance the diffusion of oxygen and nutrients. In the bi-modal and mono-modal PCL scaffolds mentioned before, the hMSCs within the seeding region of the mono-modal scaffolds proliferated faster than the cells within the bi-modal scaffolds up to 21 days after seeding [38]. This was due to the higher availability of oxygen and nutrients at the top of the scaffolds compared to the center and the bottom of the scaffold [38]. However, due to the high number of cells within the top part of these mono-modal scaffolds after three weeks, lack of space led to a reduction of living cells [38]. A higher cell number was found within decellularized bone [44], SF [72], PLGA [20] and collagen–glycosaminoglycan (CG) [61] scaffolds containing more pores with a minimum size of 200–300 μm [31]. Studies on PLGA-CaP [26] and SF [22] structures with pores between 140 and 1200 μm did not find a significant difference in cell proliferation. It is difficult to determine why some studies found a significant difference in proliferation and some did not. The materials (PLGA and SF) were used in the studies that found a significant difference in proliferation for larger pores as well as in studies that did not. Also, the pore sizes used in the latter studies were in the range of the pore sizes used in the studies in which pore size seemed to affect cell proliferation. And finally, the seeding cells used (ASCs and BMSCs) also do not seem to be the reason for the different findings. Therefore, it is not clear what pore size would promote cell proliferation.

2.2.6 Cell differentiation

The results in Table 3 imply that the pore size may affect cell differentiation. Studies on porous SF [22] and decellularized bone [44] structures found no significant difference in alkaline phosphatase (ALP) expression between structures with different pore sizes. However, an initially higher ALP activity was found in SF scaffolds (Figure 2h) with bigger pores [72]. This might suggest that small pores delay osteogenic differentiation. Studies on poly (propylene fumarate) (PPF) [21], PLGA-CaP [26], PCL [74], poly (D,L-lactic acid) (PDLLA) [24], Ti6Al4V [12] and SF [72] scaffolds found an increased osteogenic differentiation in scaffolds with larger pores.

In a study on bi-modal and mono-modal PCL scaffolds, higher OPN levels were found at the top of the scaffolds with a mono-modal architecture [38]. In those scaffolds, the seeded cells remained at the top of the scaffold and therefore faster proliferation and osteogenic differentiation occurred due to the high availability of oxygen and nutrients and exposure of the cells to osteogenic medium [38]. One explanation that osteogenic differentiation

occurred more in large pores is that the cells tend to be more spread in large pores compared to small pores. This morphology is thought to promote osteogenic differentiation [53].
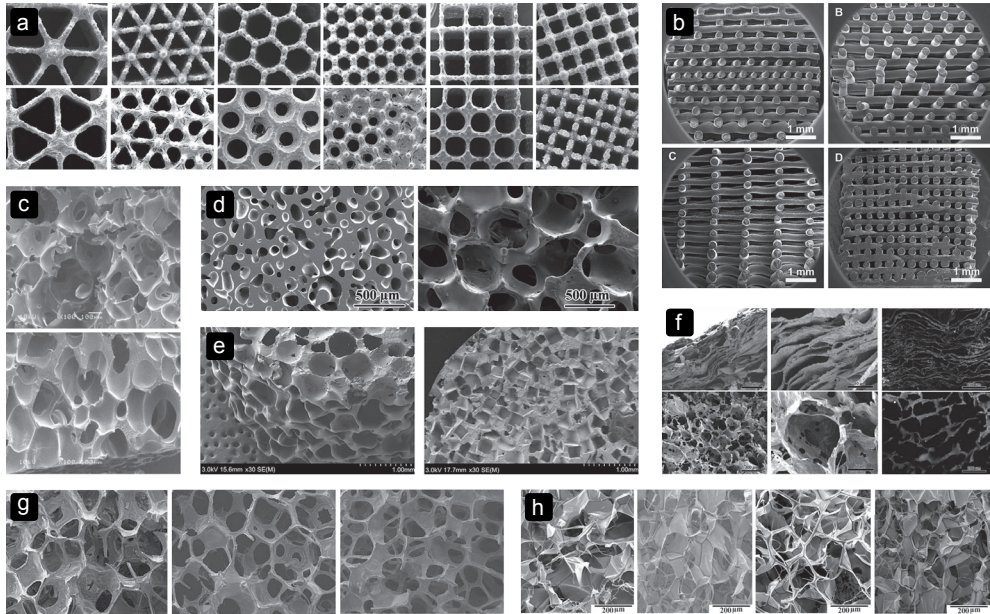
Figure 2: Different pore sizes, shapes and biomaterials. a. Ti6Al4V [12], b. SPCL [103], c. PLGA [1], d. BG [87], e. PPF [21], f. collagen-apatite [64], g. MBG [74], h. SF [72].

2.2.7   Blood vessel formation

Angiogenesis occurs by the formation of small branches at the ends of existing blood vessels [80] that grow into the bone substitute [19]. The production of vascular endothelial growth factor (VEGF) is needed to stimulate the growth of these small blood vessels [80] and is found to be higher in porous PPF biomaterials (Fig. 2e) cultured in vitro with large pores (Table 3) [21]. When insufficient blood vessels are present during the bone regeneration process, fibrous tissue will form [80]. Fibrous tissue was found in porous biomaterials with small pores in an in vivo study on β-tricalcium phosphate (β-TCP) scaffolds [27]. In the same study, more blood vessels with a bigger diameter were present and less fibrous tissue was formed in substitutes with pores bigger than 400 μm [27]. It was also observed that porous biomaterials with pores between 470 and 590 μm contained more blood vessels as compared to porous biomaterials with pores larger than 590 μm [26]. These results seem to suggest that pores larger than 400 μm are preferable for blood vessel formation and consequently for the delivery of oxygen and nutrients to the cells inside the bone substitute.

2.2.8   Tissue formation and mineralization

Tissue formation and mineralization in porous biomaterials are affected by pore sizes and porosities (Table 3). In the initial stage (*i.e.*, up to 2 weeks of *in vitro* culture), collagen structures were unorganized in a PDLLA structure [24]. After this period, they became more complex and structurally organized [24]. This was also found in implanted PLGA structures with a higher amount of collagen in structures with large pores compared to structures with small pores [81]. Thicker collagen fibers were present in PDLLA scaffolds with medium sized pores compared to scaffolds with larger and smaller pores [24]. Moreover, the amount of mineralized collagen was higher in scaffolds with medium sized pores compared to the scaffolds with large pores, and no calcium areas were found in scaffolds with the smallest pores (<275 µm) [24].

Porous biomaterials with larger pores were found to have a better and higher distribution of calcium and mineral deposition parallel to the pore walls *in vitro* [73]. This could be an effect of the alignment of cells with the pore walls, higher cell viability, distribution, and proliferation rate in structures with large pores. An *in vitro* study showed increased bone formation in scaffolds with medium sized pores, which could be related to the higher number of osteoblasts present in the inner region of these scaffolds [44]. Different *in vivo* studies have shown that a higher porosity promotes host bone ingrowth for a stable fixation with the bone substitute [11,70] and that larger pores suppress fibrous tissue infiltration [27]. In an *in vivo* study by Sicchieri *et al.*, most bone was formed in scaffolds with pores between 470 and 590 µm [26]. The limited amount of fibrous tissue infiltration and high amount of bone formation in large pores seems to be related to the higher amount of space and blood vessels present in these structures. Therefore, it can be concluded that large pores and angiogenesis are important for bone formation.

2.2.9   Structure of the new bone

The structure of the new bone grown *in vivo* depends on the organization of the synthesized collagen, which seems to be affected by the pore size [81] (Table 3). It was observed that cells tend to align with the walls of big pores where they proliferate, differentiate, and synthesize a structured collagen matrix. When this matrix becomes mineralized, it forms a lamellar structure [81]. Therefore, the alignment of cells with the pore walls in bigger pores could be used to control the structure of the newly formed bone. In a study on PLGA scaffolds with different pore size ranges of 100–300, 300–500 and 500–710 µm, the most newly formed bone with a lamellar structure was found in scaffolds with the medium pore size range [81].

2.3 Pore shape and fiber orientation

The geometry of pores within a bone substitute can be, among others, spherical, rectangular, square, hexagonal or trabecular-like, depending on the biomaterial and manufacturing process used (Figure 2). With solid freeform fabrication techniques, even more complex shapes can be realized (Figure 3) [82,83]. The pore size and shape affect the mechanical properties of porous biomaterials, as they determine the dimensions and orientation of the struts or fibers and, thus, the stress distribution inside those structural elements [12,13]. Moreover, stress concentrations due to the notches present inside the structure or caused by manufacturing imperfections could affect the mechanical behavior of porous biomaterials [13].

Scaffolds with a ladder-like structure and rectangular pores and scaffolds with large spherical pores collapse more easily than porous biomaterials with smaller uniform round pores [25]. Studies on the mechanical properties of Ti6Al4V structures (Figure 3a) with different pore shapes (diamond, cube, truncated cuboctahedron, triangular, and hexagonal) showed different mechanical properties [12] and fatigue strength for different unit cells with a similar porosity [13].

2.3.1 Seeding efficiency

In the studies evaluated (Table 4), not much research has been done on the seeding efficiency of different pore geometries. A study on SF scaffolds found no difference in the seeding efficiency of lamellar structures or structures with spherical pores [22]. However, in a study
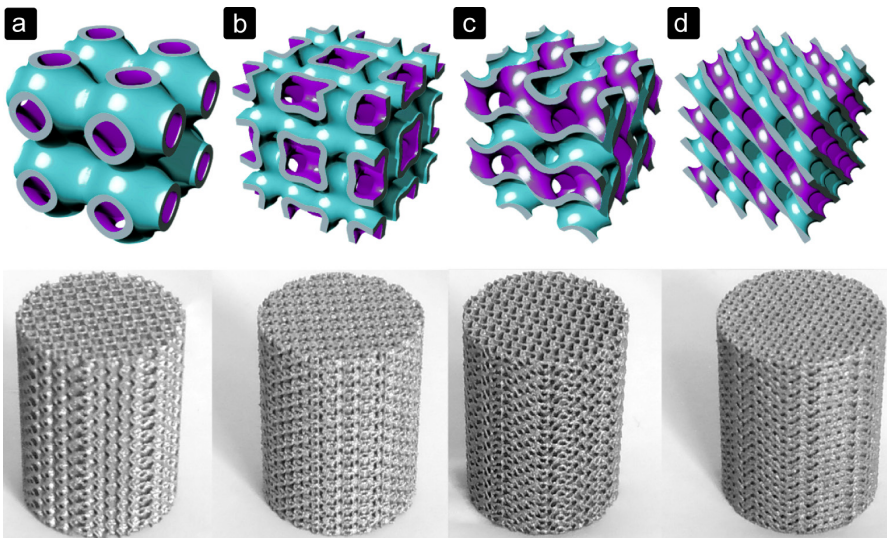
Figure 3. Selective laser melted Ti6Al4V porous biomaterials for bone regeneration based on triply periodic minimal surfaces [104]. a. primitive, b. gyroid, c. I-WP, d. diamond

where PCL scaffolds consisted of random or oriented fibers, a higher seeding efficiency was found in the scaffolds with a random fiber orientation [34]. This random architecture created a more tortuous void space and therefore a better geometry for cells to attach to during seeding.

2.3.2   Cell migration

The effects of pore shape and fiber orientation on cell migration can be found in Table 4. Cell migration is limited in collagen-apatite (Col-apatite) structures with lamellar pores compared to spherical pores [64].

In the lamellar structure, the pores are channels with a height of 30 μm, divided by Col-apatite layers (Figure 2f). The cellular structure has a more honeycomb-like structure with large interconnected pores of 242 μm (Figure 2f). The limited cell migration in the lamellar structure may have been caused by the lower interconnectivity and small distance between the lamellae as compared to spherical pores.

Cell migration behavior changes for different pore shapes. On a concave poly(dimethylsiloxane) (PDMS) surface with a depth of 100 μm and a diameter of 200 μm the cells tried to escape, while the cells on convex surfaces with similar dimensions moved on top of the convex shape [84]. A slow migration on flat surfaces was observed [84].

2.3.3   Cell alignment and morphology

The pore shape influences the cell alignment and the rate and level of pore size reduction by cells within a porous biomaterial [10,12,22,25] (Table 4). In vitro studies have shown that cells tend to bridge small distances between struts or fibers, making the pores circular-shaped [10,12]. Circular pores and pores with wide angled corners, like honeycomb pores, are reduced in size more and faster by cells that elongate and span short distances than pores with sharp corners [12]. Cells on hydroxyapatite (HA) scaffolds including a collagen fiber network connected with several collagen fibers, while the cells on the pure HA scaffolds with round pores were well spread on the pore surface [85] (Figure 1a, b). These results suggest that porous biomaterials with sharp cornered pores and an open space can delay pore size reduction by cells and consequently improve the transport of nutrients, oxygen, and waste removal. An in vitro study on cell behavior on convex and concave PDMS micro-patterns found that the cells on convex and flat surfaces had a well spread morphology [84]. A rounder morphology of the cells was found on concave micro-patterns [84].

2.3.4   Cell proliferation

The effect of pore shape and fiber orientation is summarized in Table 4. On PCL scaffolds with randomly oriented fibers, in vitro cell proliferation was found to be higher compared to

Pore shape and fiber orientation

Biomaterial	Seeding cells /implantation site	Pore shape / Pore size [μm] (porosity (%))		Seeding efficiency	Cell viability	Migration	Alignment	Morphology	Proliferation	Osteogenic differentiation	Angiogenesis	Tissue formation	Mineralization	Reference
SF	hASC	Spherical	140 (76)	+	+	+				+		+	+	22
		Spherical	254 (87)	+	+	+				+		+	+	
		Lamellar	126 (64)	+	+	+			-	++		-	+	
PCL	BMSC	Fiber orientation												34
		• Oriented		-				S	+	+				
		• Oriented offset		-				S	+	+				
		• Random		+				S	++	++				
T6Al4V	hPDC	Triangular	500		+		B	E	++	++				12
		Hexagonal	500		+		B+	E	+	+				
		Rectangular	500		+		B	E	+	+				
PPC +chitosan fiber network (CSFN)	BMSC /rabbit femoral condyle	- CSFN	300-350 (92)		+		S		+			B		86
		+ CSFN fiber 50-500nm	300-350 (92)		++		S+B		++			B+	++	
Col-apatite	BMSC, OPC /mouse calvarial defect	Spherical	242 (95)			+		E			+	LB^	+	64
		Lamellar	30 (95)			-		E			+	CB+^	++	
PDMS	L929 hMSC	Flat				+		S	+					84
		Concave				++		S	-					
		Convex				-		O	+					
HA-Col	BMSC /mouse ectopic model	HA	(80)				S	S			++	LB		85
		HA + collagen fibers	250-450 (80)				B	E/R			+	RB		
HA	/canine dorsal muscle	Concave									-	C	-	62
		Convex									+*	LB	+*	

HA	/rabbit radial diaphysis	Bi-layer outside 450 (68)	200, inside	+	B	88
		Trabecular 440 (66)		+	B+	
13-93 BG	/rat calvarial defect	Oriented 50-150 (50)		++	++	87
		Trabecular 100-500 (80)		+	+	

Table 4. The effect of pore shape and fiber orientation on cell response, angiogenesis and tissue formation. Alignment: B-bridging, S-sheet forming. Morphology: S – spread, E – elongated, R – rounded. Tissue formation: B – bone, LB – lamellar bone, RB – random bone, CB – cortical bone, C – callus. *in vitro* result, *in vivo* result. ^ more host bone integration in scaffolds seeded with BMSC compared to OPCs. * exceeded amount of calcium and blood vessels after 3 months of implantation

orthogonal oriented fibers [34]. This random organization with a more tortuous architecture also improved the seeding efficiency and therefore, more cells throughout the scaffold were able to proliferate [34]. Triangular pores in Ti6Al4V scaffolds also showed a higher amount of cell proliferation compared to hexagonal and rectangular pores. This may be due to the number of cells that bridged the small distances compared to the other two geometries. Therefore, there was more space in the triangular pores for cells to proliferate [12]. This higher amount of space also seemed to be the reason why SF structures with spherical pores performed better in terms of cell proliferation compared to the lamellar structures [22].

2.3.5   Cell differentiation

Cell differentiation seems to be affected by the pore size and fiber orientation (Table 4). In an *in vitro* study by Van Bael *et al.* (Figure 2a), triangular pores with a size of 500 μm could induce osteogenic differentiation while hexagonal pores and rectangular pores could not [12]. Another *in vitro* study found that osteogenic differentiation is affected by the orientation of a fiber network [34]. A higher ALP activity was found in random fiber structures compared to PCL structures with an organized orientation of fibers [34]. The higher number of cells in these scaffolds due to the higher seeding efficiency [34], lower reduction of pore size [12], and higher proliferation [12,34] may be the reason why more osteogenic differentiation took place.

2.3.6   Blood vessel formation

Angiogenesis seems to be affected by the organization of fibers within a porous biomaterial [85] (Table 4). An *in vivo* study by Scaglione *et al.* found many blood vessels in the void space of HA and HA/Col scaffolds after two months of implantation [85]. In HA/Col scaffolds, where there was no controlled orientation of the collagen fibers, large blood vessels grew randomly towards the center of the structure [85]. In pure HA scaffolds, where more blood vessels were found, they grew through the interconnected pore network into the scaffold [85]. HA scaffolds with concave pores have been found to be more suitable for angiogenesis in the early stages of implantation, while convex pores promote blood vessel formation after 3 months of implantation [62].

2.3.7   Tissue formation and mineralization

Results of various studies imply that the inner geometry of porous biomaterials affects the structural organization of the synthesized collagen (Table 4). In an *in vivo* study, HA scaffolds incorporated with a random orientation of collagen fibers within the pores showed an unorganized deposition of collagen 1 [85]. The pure HA scaffolds with a round pore shape contained a more organized network of collagen fibers which was deposited parallel to the pore wall [85]. In an *in vivo* study on scaffolds with concave and convex pores, more

calcium and collagen were deposited in scaffolds with concave pores [62]. However, after three months of implantation, the scaffolds with convex pores contained more collagen and calcium [62]. The fiber orientation [86] and pore shape [62,64,87] seemed to influence *in vivo* bone formation and apatite crystal deposition within the collagen matrix.

In vitro [22] and *in vivo* [87,88] bone formation seems to be enhanced in porous biomaterials with a trabecular architecture [22,87,88]. Different studies found better bone ingrowth and integration with the host bone in trabecular scaffolds compared to oriented bioactive glass (BG) [87] (Figure 2d) and SF [22] scaffolds. After 24 weeks, more bone was grown in from the sides and bottom of the scaffolds and small bone areas were present within the trabecular BG implants [87]. This indicates that osteoblasts were present within the scaffold and were able to form apatite crystals. In scaffolds with lamellar pores, more bone was formed after 4 weeks of implantation as compared to cellular shaped pores [64]. The addition of a chitosan fiber network to PPC scaffolds led to more *in vivo* bone formation compared to pure PPC scaffolds [86]. The higher number of cells within these scaffolds due to the higher cell viability and higher proliferation may be the reason why more bone formed in these scaffolds compared to the pure PPC scaffolds.

2.3.8   Structure of the new bone

The pore shape seems to affect the structure of the new bone (Table 4). This was found in an *in vivo* study by Yu *et al.*, where a lamellar or cellular structure (Figure 2f) seeded with either OPCs or BMSCs was placed inside a bone defect [64]. In the lamellar structure, cortical like bone was formed, while a bone structure similar to trabecular bone was formed within the cellular structure (Figure 4) [64]. They also found that BMSCs promoted host bone integration with the scaffolds, while OPCs did not [64].
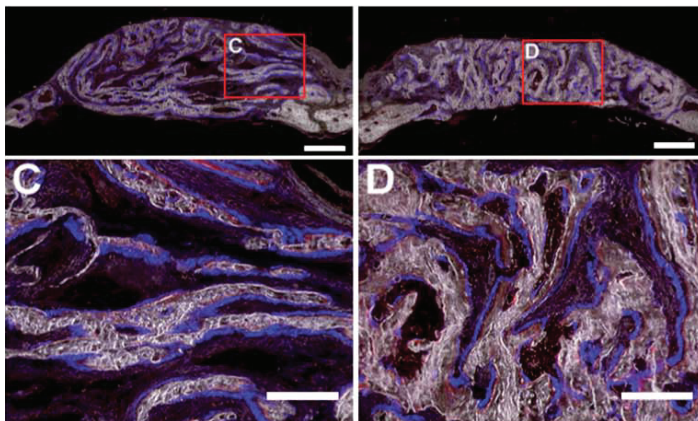
Figure 4. Formation of new bone in collagen-apatite scaffolds after 4 weeks [64]. C- cortical bone structure formed in structures with a lamellar structure loaded with OPCs. D- trabecular bone structure formed in structures with a lamellar architecture loaded with OPCs.

The *in vivo* formed bone in pure HA scaffolds with an ordered inner geometry had a lamellar structure with collagen fibers deposited parallel to the pore wall, while the orientation of collagen fibers and bone formation on the HA/Col scaffolds was random [85]. Active osteoblasts were still present in HA/Col scaffolds after two months, which indicates that woven bone was present in these scaffolds [85]. Thin lining cells that control the mineral composition of bone were covering the new bone formed in the HA scaffolds [85]. Structures with convex pores induced *in vivo* formation of lamellar bone with osteoblasts and osteoclasts, while almost no mature bone was found in structures with concave pores [62]. This might be related to the higher vascularity in the structures with convex pores [62].

2.4 Surface topography and chemistry

Surface characteristics are important for adhesion, attachment, and spreading of cells on the surface of biomaterials [89]. In addition to the biomaterial a bone substitute is made of, the use of surface treatments [16], addition of a silk [74] or CaP coating [17], and integration of HA particles [25,28,29,37] or HA whiskers [30] may affect the surface roughness and can improve the bioactivity of a porous biomaterial [58]. Incorporation of CaP coatings, such as HA particles or whiskers, are thought to improve bone formation in porous biomaterials [58]. It is thought that due to the similarity between the composition of CaPs and bioapatite, cells would respond in a similar way as during natural bone remodeling [58].

2.4.1   Seeding efficiency

A higher surface roughness is associated with a higher surface area [90] to which cells can attach during seeding. Various studies have shown (Table 5) that the initial attachment and seeding efficiency increases with an increased surface roughness in Ti6Al4V [16,91] and HA [92] structures, or surface chemistry of PCL/nHA porous biomaterials [28]. In contrast to these findings, silk scaffolds with an increased HA micro-particle content showed a lower seeding efficiency despite a higher surface roughness [29]. In a study on mesoporous bioactive glass (MBG) scaffolds (Figure 2g) incorporated with a silk film within the pores to reduce the surface roughness, no significant difference in seeding efficiency was found [74]. Although a higher surface roughness increases the surface area and would therefore be preferable for improved seeding efficiency, contradictory results were found. It seems that a significant difference in surface roughness may indeed increase the seeding efficiency. However, the seeding efficiency does not seem to be affected when there is no significant difference in surface roughness between the compared samples.

2.4.2   Cell alignment and morphology

Cells adapt their morphology according to the surface topography of porous biomaterials

[2,28,35,74,92] (Table 5). A higher surface roughness of PCL/nHA [28] and calcium phosphate (CaP) [2] scaffolds elicited a more spread cell morphology, while a higher surface roughness of PCL [35] and MBG [74] scaffolds drove hBMSCs to a less spread and more rounded morphology (Figure 1e and f). On HA [92], Ti6Al4V [91], thermoplastic polyurethane (TPU) [25], and collagen [30] structures no difference in cell morphology was found. The cells were spread on the surface of all scaffolds. These contradictory results may imply that not only surface roughness but also surface chemistry affect the cell morphology. The surface properties of a biomaterial determine how well the cells can attach to the surface, which in turn affects their morphology.

2.4.3   Cell proliferation

The results in Table 5 suggest that adding HA to porous biomaterials may improve cell proliferation [28,29,92]. A higher cell proliferation rate was found on HA scaffolds with a smooth surface [92] and in scaffolds with nHA whiskers [28,29]. On titanium structures, the number of cells increased upon increasing the surface roughness [91,93]. Cell attachment and proliferation were significantly different between Ti6Al4V porous biomaterials with an arithmetical mean roughness (Ra) of 0.32 µm and 0.87 µm [91]. Given this difference, it seems that hBMSCs are sensitive to a surface roughness difference of about 0.6 µm [91]. A study by Kumar *et al.* showed an equally good proliferation rate on etched and unetched PCL scaffolds with Ra values of 1.1 and 0.2 µm, respectively [35]. Although the variation in Ra was more than 0.6 µm and hBMSCs were used, the different outcome may have been caused by the different surface chemistry or stiffness of these porous biomaterials.

2.4.4   Cell differentiation

While the higher surface roughness of PCL scaffolds created by etching had no effect on the cell proliferation and caused a more rounded morphology of the cells (Fig. 1), more osteogenic differentiation of hBMSCs occurred [35] (Table 5). A higher surface roughness seems to improve cell differentiation on Col-HA [30] and MBG [74] scaffolds while smooth surfaces tend to slow down osteogenic differentiation. In contrast to these results, more osteogenic differentiation was present in Ti structures with a lower surface roughness [93]. In two other studies on HA [92] and Ti6Al4V [91], where the surface roughness was significantly different between the tested samples, no difference in osteogenic differentiation was found. Although cell morphology is thought to affect the type into which cells differentiate, these contradictory results do not seem to show this relationship.

2.4.5   Tissue formation and mineralization

Fixation of a porous biomaterial with the native bone is facilitated by friction, mechanical interlocking, and chemical bonding [94]. The highest bond strength, mineralization, and bone

Surface roughness and chemistry

Biomaterial	Seeding cells /implantation site	Surface roughness [μm]	Seeding efficiency	Cell viability	Migration	Alignment	Morphology	Proliferation	Osteogenic differentiation	Angiogenesis	Tissue formation	Mineralization	Reference
Ti6Al4V	hPDC /rat femoral defect	Untreated	+			B/S		+			B	+	16
		Alkali-Acid (100-200nm)	+			B/S		+			B+	++	
		Alkali-Acid-Heat (100-200nm)	++			B/S		++			B	+	
		Anodizing-Heat (nanotubes)	+			B/S		+++			B	++	
												+	
Silk	hBMSC	0% HA (smooth)	++	+				-			B	+	29
		1.6% HA (rough)	+	+				+			B+	+	
		3.1% HA (rough+)	+	+				+			B++	+	
		4.6 % HA (rough +)	-	+				+			B++	+	
Ti6Al4V	hBMSC	0.320	+			B	E/S	++	+				91
		0.490	+			B	E/S	+	+				
		0.874	++			B	E/S	+	+				
HA	hBMSC	0.733	+			B	E/S	++	+				92
		2.856	+			B	E/S	+	+				
		4.680	++			B	E/S	+	+				
MBG	BMSC	MBG (rough)	+			S	E/S	-	+				74
		MGB +2.5% silk (smooth)	+			S+	E/S	+	+				
		MGB +5.0% silk (smooth)	+			S+	E/S	+	++				
PLGA	MC3T3	PLGA (smooth)	+	+			S	+	+			-	37
		+5% HA (rough)	+	+			S+	+	++			+	
TPU (HA particles)	3T3	TPU		+		S	S					-	25
		TPU +mHA		+		S	S					-	
		TPU +nHA		+		S	S					+	
Collagen	mASC	Collagen			+	B	E		-				30
		40 % HA whiskers			+	B	E		+				
		80% HA whiskers			+	B	E		+				

Material	Cells / animal model	Surface	Morphology / Alignment	Cell response	Angiogenesis	Tissue formation (in vivo)	Ref
PCL	MG-63	PCL	L, R	+			28
		PCL+nHA	S, S	++			
PCL	hBMSC	0.21	S	+	−	*−*	35
		1.06	R	+	+	*+*	
CaP/gelatin	hOPC /rabbit radial diaphysis	Unpatterned	E	−		*B* −	2
		50 µm grooves	S	−		*B+* +	
		40 µm pits	S	+		*B+* +	
Ti grade 2 (+nanoscale modification (NM))	MG63	0.43	++	++	V−		93
		0.37 +NM	+	+	V		
		3.29	+	+	V+		
		2.80 +NM	+	+	V++		
HA	/pig latissimus dorsi	Non-microporous fibers		+	−	*−*	36
		Microporous fibers 2-8 µm		+	+	*LB,WB*	
Titanium 200-400 µm pores	/canine femoral defect	Untreated (smooth)			−	*B*	18
		Anodized (nanotubes)			−	*B*	
		Heat-treated+anodized (nanotubes)			+	*B+*	

Table 5. The effect of surface roughness and chemistry on cell response, angiogenesis and tissue formation. Alignment: B-bridging, S-sheet forming. Morphology: S – spread, E – elongated, R – rounded. Tissue formation: B – bone, LB – lamellar bone, WB – woven bone. *in vitro* result, *in vivo* result.

formation were found in Ti6Al4V porous biomaterials with anatase nanotubes compared to structures with non-bioactive nanotubes and structures without treatment after three months of *in vivo* implantation [18] (Table 5). A higher bond strength can be related to a higher surface roughness, which promotes osseointegration [2,95].

In vivo implanted HA scaffolds with an increased surface roughness upon the addition of microporous rods contained newly formed bone in the center, top, and periphery of the scaffolds, while bone was only present at the periphery of HA scaffolds without porous rods [36]. This could be explained by the presence of rhBMP-2 and blood vessels in the center of the scaffolds which supplied mesenchymal stem cells [36]. Due to the microporous rods, more rhBMP-2 and HA surface area was present in these scaffolds compared to HA scaffolds without rods, bone formation was more promoted in these scaffolds [36]. A higher amount of *in vitro* [25,29,37] bone formation [29,30] and mineralization [25,29,37] in scaffolds with HA particles [25,29,37] seems to imply that the addition of HA improves osteogenesis. Applying surface treatments to bone substitutes can also change the surface chemistry and roughness to improve mineralization. It was shown that different surface treatments of Ti6Al4V structures change these properties [16]. *In vivo* apatite formation and osseointegration were the highest in structures treated with an acid–alkali (AcAl), while anodized-heat (AnH) treated and as-manufactured (AsM) structures showed the lowest apatite formation [16]. Although the AnH treated specimens did not stimulate apatite formation, they had the best mechanical stability when tested under torsion [16]. This may be due to their higher surface roughness with micropits and nanotubes on their surface, which improved mechanical interlocking and the mechanotransduction pathways of the cells on the surface [16].

2.5 Structure stiffness

Biomaterials that are used for bone substitutes could be roughly divided into three groups, namely metals, ceramics, and polymers [96], with different mechanical properties. The stiffness of metals is in general higher than the elastic modulus of bone, while the stiffness of polymers is lower [97] (Table 6). Consequently, the load transfer varies and leads to different stress and deformation patterns throughout the implant [94]. During migration, cells adhere to the surface of the porous biomaterial and pull themselves forward [51]. Through their adhesions to the surface, cells apply forces to the structure and sense the stiffness of this structure [89,98]. Although it is assumed that cell attachment depends on the structure stiffness [55,89], no effect of the stiffness on the migration of cells was found in the studies evaluated.

2.5.1 Seeding efficiency

Not many studies investigated the effect of structural stiffness on the seeding efficiency (Table 6). One study on the stiffness of PDMS scaffolds found a higher seeding efficiency on the

softest structures, which decreased with increasing stiffness [63]. However, on PPF scaffolds (Figure 2e), a similar seeding efficiency was found on structures with different stiffness [21]. Despite the lack of studies on seeding efficiency and substrate stiffness, there does not seem to be a connection between these two.

2.5.2   Cell viability

The structure stiffness does not seem to affect the cell viability (Table 6) of polyacrylamide (PA) scaffolds with a stiffness in the range of 0.5–26 kPa [65,99]. However, a study on thermoplastic gelatin (TG)-gel scaffolds found a lower cell viability on scaffolds with a lower structure stiffness [100]. Due to the limited and contradictory results, no conclusion can be drawn on the relationship between the substrate stiffness and cell viability.

2.5.3   Cell alignment and morphology

It was assumed that the structure stiffness would affect the cell morphology, where a well-spread morphology would induce osteogenic differentiation [53]. Although differences in morphology were found on TG-gel [100] and PA [101] scaffolds with different stiffness, cells on substrates with a higher stiffness were not necessarily more spread (Table 6). A study on PA scaffolds showed that cells were more rounded on substrates with a stiffness of 10 and 23 kPa compared to substrates with a stiffness of 34 kPa [101]. However, the cells were more spread on the scaffolds with a stiffness of 34 kPa compared to the scaffolds with a stiffness of 40 kPa [101]. In another study, cells were more rounded on TG-gel structures with a higher stiffness compared to the softest scaffold [100]. Although the morphology of cells was different on structures with different stiffness, a higher stiffness did not necessarily lead to a more spread cell morphology.

2.5.4   Cell differentiation

A higher stiffness of hexafluoroisopropanol (HFIP) [46] and MBG [74] scaffolds achieved by the addition of silk microfibers, improved early hMSC differentiation into the osteogenic lineage (Table 6). This was also observed in PPF scaffolds with a higher stiffness due to the incorporation of diethyl fumarate (DEF) [21]. In PDMS [63] and PA [65,99] scaffolds, the stiffest scaffolds also showed the most osteogenic differentiation. On the PDMS structures, either BMCs or AMSCs were seeded to see the response of both cell types [63]. This study showed that BMSCs differentiated more into osteoblasts than AMSCs [63]. In contrast to the highest cell differentiation on the above-mentioned porous biomaterials, the most osteogenic cell differentiation took place on the PA scaffolds with the second highest stiffness [101]. Although there did not seem to be a relationship between cell morphology and substrate stiffness, a higher stiffness resulted in general in more cells that differentiated into osteoblasts. However, as can be seen in the PA scaffolds [101], there are some exceptions.

Structure stiffness

Biomaterial	Seeding cells /implantation site	Structure stiffness		Seeding efficiency	Cell viability	Migration	Alignment	Morphology	Proliferation	Osteogenic differentiation	Angiogenesis	Tissue formation	Mineralization	Reference
PPF + DEF%	Rat BMSC	0%	18 MPa	-						-	>			21
		+10%	31 MPa	+						+	>			
		+25%	43 MPa	+						+	>			
		+33%	28 MPa	+						++	V+			
PDMS	rAMSC	Softest		+++						-				63
		Soft		++						-				
	rBMSC	Middle		+						+-				
		Stiff		+-						+				
		Stiffest		-						++*				
PA	MSC	0.51 kPa			+				+	+			-	99
		3.7 kPa			+				++	+			-	
		22 kPa			+				+++	++			+	
PA	BMSC	1.46 kPa			+				+	+^			+	65
	BDC	26.12 kPa			+				+	++^			++	
TG-Gel	C2C12	1.58 kPa			-			E	+	-	+	-		100
		13.51 kPa			+			R	+	+	+	B		
		32.32 kPa			+			R	+	-	+	B+		
PCL	MG-63	PCL	124kPa				L	R	+					28
		PCL+nHA	275kPa				S	S	++					
PA	hBMSC	10 kPa						S-		- -				101
		23 kPa						S		-				
		34 kPa						S++		++				
		40 kPa						S+		+				

Material	Model	Structure	Stiffness	Morphology	Cell response	Angiogenesis	Tissue formation	Ref
MBG +silk%	BMSC	MBG	60 kPa	E/S	++	-	-	
		+2.5%	120 kPa	E/S+	+	+	+	74
		+5.0%	250 kPa	E/S+	+	++	++	
HFIP-silk +silk fiber	hMSC /mouse lateral subcutaneous pockets	Control	85.06 kPa		-	-	-	
		+fiber S	4.52 MPa		+	+	+	46
		+fiber M	9.79 MPa		++	+	+	
		+fiber L	10.64 MPa		+	+	+	
Ti6Al4V	/sheep metatarsal bone	Flex cage	5.9 GPa			+	B+	14
		Porous cylinder	8.22 GPa			++	B	

Table 6. The effect of structure stiffness on cell response, angiogenesis and tissue formation. Morphology: S – spread, E – elongated, R – rounded. Angiogenesis: V – VEGF, Tissue formation: B – bone. *in vitro* result, *in vivo* result. * BMSC showed higher osteogenic differentiation than AMSC. ^ Osteogenic differentiation of BDCs was lower for BDCs compared to BMSCs. Also, no significant difference in osteogenic differentiation of BDCs was found among the different scaffolds with a different stiffness.

2.5.5 Tissue formation and mineralization

The implant stiffness affects integration with the host bone when there is a clear difference in stiffness (Table 6). An increased stiffness of MBG scaffolds promoted the *in vitro* formation of apatite particles [74], which may be due to the highest amount of osteogenic differentiation in these scaffolds.

In an *in vivo* study on titanium implants with two completely different designs, a stable bone-implant interface was present [14]. However, more bone was present within and around flex-cage scaffolds as compared to the stiffer selective laser melted porous biomaterials [14]. This suggests that structure stiffness values close to the stiffness of bone also promote bone ingrowth and bone-porous biomaterial integration.

2.6 Discussion and conclusion

This paper presents an overview of how cells respond to the architecture and surface properties of porous biomaterials for bone regeneration. We have seen that the biomaterial(s) chosen for the bone substitute is responsible for the mechanical properties and surface properties and determines the applicable manufacturing process. The manufacturing technique in turn determines the accuracy and control over the architecture of the bone substitute.

For metal bone substitutes, selective laser melting (SLM) [10–16], selective laser sintering (SLS) [17] sintering [18], perforating titanium sheet [14] and capsule-free hot isostatic pressing (CF-HIP) [19] were used. Those manufacturing techniques differ in terms of their production accuracy. Both SLM and SLS can be used to create complex structures [10–13] with a completely controlled architecture [102], while porous biomaterials manufactured with CF-HIP [19] and sintering [18] had a relatively simple geometry. The size and the shape of pores between the metal powder particles can be partly controlled and acted as the void space for tissue regeneration [18,19]. Sheet perforation was used to cut rhombic holes into a titanium sheet which was shaped into a star [14]. Although the shape and size of the holes and the geometry of the sheet can be modified, no 'inner' architecture was present in these biomaterials [14]. The polymer and ceramic bone substitutes evaluated in this study were manufactured with porogen leaching [20–30], freeze drying [31]. 3D printing of successive fiber/strut layers [32–36], electrospinning [37], or gas foaming [1,38]. 3D printing of fiber layers and electro spinning were used to generate fiber-based constructs with a controlled and uncontrolled architecture, respectively. It was seen that with the other techniques, the pore size, interconnectivity and pore shape could be partly controlled (Figure 2). 3D printing is the most promising manufacturing technique for load bearing (biodegradable) metal bone substitutes because high control over the architecture of the structures can be realized (Figure 3).

Different studies have shown that the seeding efficiency is mainly affected by the pore size of the porous biomaterials. However, more than just the pore size should be taken

into account when optimizing the seeding efficiency of a structure for bone regeneration. Although it is important to prevent cells from aggregating at the seeding surface by making the pores not too small, it is also important to take the tortuosity and interconnectivity of the void space into account. Different results would be acquired when cells are seeded onto a scaffold with pores in which the cells can vertically fall through the structure or when they can only reach the bottom of the implant via tortuous pathways. Therefore, based on the tortuosity and the interconnectivity of the void space that are created with the manufacturing technique, a suitable pore size (>100 µm) should be chosen. For good progress of all the steps following cell seeding, the pores should have a minimum size of 200–300 µm.

Cell aggregation should be prevented because this can obstruct the path to the center of the structure. Cells tend to bridge small distances which occur in small pores, in pores with sharp angles and in structures with randomly deposited fibers. It was found that it takes more time for cells to reduce the size of the pores with wide angles or spherical pores as compared to pores with sharp angles [12]. This makes sense because more space is available at the corners of pores with sharp angles (triangular pores) as compared to the spherical pores with a similar pore size. If pores are large enough, cells align with the pore walls and form sheets, which leaves the void space open for oxygen and nutrients to reach the inner regions of the porous biomaterial. Because oxygen and nutrients are vital for cells to survive and proliferate, porous biomaterials with large pores are preferable for bone regeneration.

The alignment of cells with the walls of large pores causes cells to synthesize a collagen matrix which is aligned with the pore walls. This behavior could be used to control or guide the desired bone structure within biodegradable structures. Cells aligned within lamellar shaped pores tend to form cortical bone, while a trabecular bone structure could be achieved by designing a structure with big spherical shaped pores.

Cell proliferation depends on the available surface area for cells to multiply and may also be dependent on the surface roughness. However, due to disparity in the results no decisive conclusion could be drawn regarding the effects of surface roughness on cell proliferation.

Porous biomaterials with a pore size larger than 400 µm seem to be beneficial for angiogenesis. Blood vessels provide the cells and nutrients needed for bone formation and grow into the porous biomaterial through the interconnected pore network. When the void space is clearly defined, blood vessels will grow in a controlled way, while a random inner architecture leads to an uncontrolled network of blood vessels. It is clear that a well vascularized structure is important for the formation of new bone.

The addition of HA or CaP increases the surface roughness and chemistry, thereby improving cell adhesion and promoting a well-spread morphology. A well-spread morphology is associated with osteogenic differentiation as shown in a study by McBeath et al. [53], and seems to be the case in more studies. However, it was seen that in some studies a less spread morphology could also induce osteogenic differentiation. Cell differentiation into osteoblasts

is also promoted by structures with an elastic modulus close to the stiffnes of bone.

More new bone is found in structures with bigger pores, a higher porosity, the addition of chitosan or HA, a higher surface roughness, and a stiffness close to the elastic modulus of bone. A higher surface roughness promotes mechanical interlocking, which improves the bond strength between the porous biomaterial and the host bone.

These findings show that different cell responses are connected to each other. Although the seeding efficiency is well studied in different papers, a higher seeding efficiency is not crucial for consequent cell responses. Even though a higher seeding efficiency was found in porous biomaterials with smaller pores, small pores do not seem to be beneficial for other steps in the bone regeneration process. Good perfusion of oxygen and nutrients is preferable for high cell viability and proliferation, and osteogenic differentiation and blood vessel formation are important for the mineralization of the synthesized collagen matrix and bone formation.

Future research should focus on optimizing the diffusion of oxygen and nutrients to the inner regions of a bone substitute to promote osteogenic differentiation and the formation of blood vessels. This paper shows that different aspects have to be considered when designing a porous biomaterial for bone regeneration. With the information available, it is impossible to say what value should be chosen for every architectural parameter to design the 'ideal' porous biomaterial. Depending on the biomaterial of the bone substitute, an appropriate porosity, pore size, and pore shape should be chosen to make the porous biomaterial suitable for the implantation site. By designing a tortuous void network, the cell suspension is more guided through the scaffold which increases the available surface and time for the cells to attach to the surface of the porous biomaterial. It is more or less clear that a pore size smaller than 100 µm should be avoided, that pores smaller than 200–300 µm may limit cell migration and proliferation and that pores larger than 400µm are preferable for angiogenesis.

References

[1] Y. Reinwald, R. Johal, A. Ghaemmaghami, F. Rose, S. Howdle, K. Shakesheff, Interconnectivity and permeability of supercritical fluid-foamed scaffolds and the effect of their structural properties on cell distribution, Polymer 55(1) (2014) 435-444.

[2] D. Nadeem, C.-A. Smith, M.J. Dalby, R.D. Meek, S. Lin, G. Li, B. Su, Three-dimensional CaP/gelatin lattice scaffolds with integrated osteoinductive surface topographies for bone tissue engineering, Biofabrication 7(1) (2015) 015005.

[3] C.E. Holy, M.S. Shoichet, J.E. Davies, Engineering three-dimensional bone tissue in vitro using biodegradable scaffolds: investigating initial cell-seeding density and culture period, Journal of biomedical materials research 51(3) (2000) 376-382.

[4] B. Seo, W. Sonoyama, T. Yamaza, C. Coppe, T. Kikuiri, K. Akiyama, J. Lee, S. Shi, SHED repair critical-size calvarial defects in mice, Oral diseases 14(5) (2008) 428-434.

[5] J. Park, J. Ries, K. Gelse, F. Kloss, K. Von Der Mark, J. Wiltfang, F. Neukam, H. Schneider, Bone regeneration in critical size defects by cell-mediated BMP-2 gene transfer: a comparison of adenoviral vectors and liposomes, Gene therapy 10(13) (2003) 1089-1098.

[6] Z.S. Patel, S. Young, Y. Tabata, J.A. Jansen, M.E. Wong, A.G. Mikos, Dual delivery of an angiogenic and an osteogenic growth factor for bone regeneration in a critical size defect model, Bone 43(5) (2008) 931-940.

[7] M.P. Lutolf, F.E. Weber, H.G. Schmoekel, J.C. Schense, T. Kohler, R. Müller, J.A. Hubbell, Repair of bone defects using synthetic mimetics of collagenous extracellular matrices, Nature biotechnology 21(5) (2003) 513-518.

[8] H.H. Lu, S.F. El-Amin, K.D. Scott, C.T. Laurencin, Three-dimensional, bioactive, biodegradable, polymer–bioactive glass composite scaffolds with improved mechanical properties support collagen synthesis and mineralization of human osteoblast-like cells in vitro, Journal of Biomedical Materials Research Part A 64(3) (2003) 465-474.

[9] D.F. Williams, On the mechanisms of biocompatibility, Biomaterials 29(20) (2008) 2941-2953.

[10] P.H. Warnke, T. Douglas, P. Wollny, E. Sherry, M. Steiner, S. Galonska, S.T. Becker, I.N. Springer, J. Wiltfang, S. Sivananthan, Rapid prototyping: porous titanium alloy scaffolds produced by selective laser melting for bone tissue engineering, Tissue engineering part c: Methods 15(2) (2008) 115-124.

[11] J. Van der Stok, O.P. Van der Jagt, S. Amin Yavari, M.F. De Haas, J.H. Waarsing, H. Jahr, E.M. Van Lieshout, P. Patka, J.A. Verhaar, A.A. Zadpoor, Selective laser melting-produced porous titanium scaffolds regenerate bone in critical size cortical bone defects, Journal of Orthopaedic Research 31(5) (2013) 792-799.

[12] S. Van Bael, Y.C. Chai, S. Truscello, M. Moesen, G. Kerckhofs, H. Van Oosterwyck, J.-P. Kruth, J. Schrooten, The effect of pore geometry on the in vitro biological behavior of human periosteum-derived cells seeded on selective laser-melted Ti6Al4V bone scaffolds, Acta biomaterialia 8(7) (2012) 2824-2834.

[13] S.A. Yavari, S. Ahmadi, R. Wauthle, B. Pouran, J. Schrooten, H. Weinans, A. Zadpoor, Relationship between unit cell type and porosity and the fatigue behavior of selective laser melted meta-biomaterials, Journal of the mechanical behavior of biomedical materials 43 (2015) 91-100.

[14] J. Wieding, T. Lindner, P. Bergschmidt, R. Bader, Biomechanical stability of novel mechanically adapted open-porous titanium scaffolds in metatarsal bone defects of sheep, Biomaterials 46 (2015)

35-47.

[15] J. Wieding, A. Jonitz, R. Bader, The effect of structural design on mechanical properties and cellular response of additive manufactured titanium scaffolds, Materials 5(8) (2012) 1336-1347.

[16] S.A. Yavari, J. van der Stok, Y.C. Chai, R. Wauthle, Z.T. Birgani, P. Habibovic, M. Mulier, J. Schrooten, H. Weinans, A.A. Zadpoor, Bone regeneration performance of surface-treated porous titanium, Biomaterials 35(24) (2014) 6172-6181.

[17] E. García-Gareta, J. Hua, G.W. Blunn, Osseointegration of acellular and cellularized osteoconductive scaffolds: Is tissue engineering using mesenchymal stem cells necessary for implant fixation?, Journal of Biomedical Materials Research Part A (2014).

[18] X. Fan, B. Feng, Z. Liu, J. Tan, W. Zhi, X. Lu, J. Wang, J. Weng, Fabrication of TiO2 nanotubes on porous titanium scaffold and biocompatibility evaluation in vitro and in vivo, Journal of Biomedical Materials Research Part A 100(12) (2012) 3422-3427.

[19] X. Liu, S. Wu, K.W. Yeung, Y. Chan, T. Hu, Z. Xu, X. Liu, J.C. Chung, K.M. Cheung, P.K. Chu, Relationship between osseointegration and superelastic biomechanics in porous NiTi scaffolds, Biomaterials 32(2) (2011) 330-338.

[20] A.R. Amini, D.J. Adams, C.T. Laurencin, S.P. Nukavarapu, Optimally porous and biomechanically compatible scaffolds for large-area bone regeneration, Tissue Engineering Part A 18(13-14) (2012) 1376-1388.

[21] K. Kim, D. Dean, J. Wallace, R. Breithaupt, A.G. Mikos, J.P. Fisher, The influence of stereolithographic scaffold architecture and composition on osteogenic signal expression with rat bone marrow stromal cells, Biomaterials 32(15) (2011) 3750-3763.

[22] C. Correia, S. Bhumiratana, L.-P. Yan, A.L. Oliveira, J.M. Gimble, D. Rockwood, D.L. Kaplan, R.A. Sousa, R.L. Reis, G. Vunjak-Novakovic, Development of silk-based scaffolds for tissue engineering of bone from human adipose-derived stem cells, Acta biomaterialia 8(7) (2012) 2483-2492.

[23] S. Hofmann, H. Hagenmüller, A.M. Koch, R. Müller, G. Vunjak-Novakovic, D.L. Kaplan, H.P. Merkle, L. Meinel, Control of in vitro tissue-engineered bone-like structures using human mesenchymal stem cells and porous silk scaffolds, Biomaterials 28(6) (2007) 1152-1162.

[24] M. Stoppato, E. Carletti, V. Sidarovich, A. Quattrone, R.E. Unger, C.J. Kirkpatrick, C. Migliaresi, A. Motta, Influence of scaffold pore size on collagen I development: a new in vitro evaluation perspective, Journal of Bioactive and Compatible Polymers 28(1) (2013) 16-32.

[25] H.-Y. Mi, X. Jing, M.R. Salick, T.M. Cordie, X.-F. Peng, L.-S. Turng, Morphology, mechanical properties, and mineralization of rigid thermoplastic polyurethane/hydroxyapatite scaffolds for bone tissue applications: effects of fabrication approaches and hydroxyapatite size, Journal of Materials Science 49(5) (2014) 2324-2337.

[26] L.G. Sicchieri, G.E. Crippa, P.T. de Oliveira, M.M. Beloti, A.L. Rosa, Pore size regulates cell and tissue interactions with PLGA–CaP scaffolds used for bone engineering, Journal of tissue engineering and regenerative medicine 6(2) (2012) 155-162.

[27] B. Feng, Z. Jinkang, W. Zhen, L. Jianxi, C. Jiang, L. Jian, M. Guolin, D. Xin, The effect of pore size on tissue ingrowth and neovascularization in porous bioceramics of controlled architecture in vivo, Biomedical Materials 6(1) (2011) 015007.

[28] J. Qian, M. Xu, A. Suo, T. Yang, X. Yong, An innovative method to fabricate honeycomb-like poly (ε-caprolactone)/nano-hydroxyapatite scaffolds, Materials Letters 93 (2013) 72-76.

[29] S. Bhumiratana, W.L. Grayson, A. Castaneda, D.N. Rockwood, E.S. Gil, D.L. Kaplan, G. Vunjak-Novakovic, Nucleation and growth of mineralized bone matrix on silk-hydroxyapatite composite scaffolds, Biomaterials 32(11) (2011) 2812-2820.

[30] R.J. Kane, H.E. Weiss-Bilka, M.J. Meagher, Y. Liu, J.A. Gargac, G.L. Niebur, D.R. Wagner, R.K. Roeder, Hydroxyapatite reinforced collagen scaffolds with improved architecture and mechanical properties, Acta biomaterialia 17 (2015) 16-25.

[31] C.M. Murphy, M.G. Haugh, F.J. O'Brien, The effect of mean pore size on cell attachment, proliferation and migration in collagen–glycosaminoglycan scaffolds for bone tissue engineering, Biomaterials 31(3) (2010) 461-466.

[32] P. Yilgor, G. Yilmaz, M. Onal, I. Solmaz, S. Gundogdu, S. Keskil, R. Sousa, R. Reis, N. Hasirci, V. Hasirci, An in vivo study on the effect of scaffold geometry and growth factor release on the healing of bone defects, Journal of tissue engineering and regenerative medicine 7(9) (2013) 687-696.

[33] C. Wu, Y. Luo, G. Cuniberti, Y. Xiao, M. Gelinsky, Three-dimensional printing of hierarchical and tough mesoporous bioactive glass scaffolds with a controllable pore architecture, excellent mechanical strength and mineralization ability, Acta biomaterialia 7(6) (2011) 2644-2650.

[34] P. Yilgor, R.A. Sousa, R.L. Reis, N. Hasirci, V. Hasirci, Effect of scaffold architecture and BMP-2/BMP-7 delivery on in vitro bone regeneration, Journal of Materials Science: Materials in Medicine 21(11) (2010) 2999-3008.

[35] G. Kumar, M.S. Waters, T.M. Farooque, M.F. Young, C.G. Simon, Freeform fabricated scaffolds with roughened struts that enhance both stem cell proliferation and differentiation by controlling cell shape, Biomaterials 33(16) (2012) 4022-4030.

[36] J.R. Woodard, A.J. Hilldore, S.K. Lan, C. Park, A.W. Morgan, J.A.C. Eurell, S.G. Clark, M.B. Wheeler, R.D. Jamison, A.J.W. Johnson, The mechanical properties and osteoconductivity of hydroxyapatite bone scaffolds with multi-scale porosity, Biomaterials 28(1) (2007) 45-54.

[37] L. Lao, Y. Wang, Y. Zhu, Y. Zhang, C. Gao, Poly (lactide-co-glycolide)/hydroxyapatite nanofibrous scaffolds fabricated by electrospinning for bone tissue engineering, Journal of Materials Science: Materials in Medicine 22(8) (2011) 1873-1884.

[38] A. Salerno, D. Guarnieri, M. Iannone, S. Zeppetelli, P.A. Netti, Effect of micro-and macroporosity of bone tissue three-dimensional-poly (ε-caprolactone) scaffold on human mesenchymal stem cells invasion, proliferation, and differentiation in vitro, Tissue Engineering Part A 16(8) (2010) 2661-2673.

[39] J. Sanz-Herrera, J. Garcia-Aznar, M. Doblare, A mathematical model for bone tissue regeneration inside a specific type of scaffold, Biomechanics and modeling in mechanobiology 7(5) (2008) 355-366.

[40] C. Jungreuthmayer, S.W. Donahue, M.J. Jaasma, A.A. Al-Munajjed, J. Zanghellini, D.J. Kelly, F.J. O'Brien, A comparative study of shear stresses in collagen-glycosaminoglycan and calcium phosphate scaffolds in bone tissue-engineering bioreactors, Tissue Engineering Part A 15(5) (2008) 1141-1149.

[41] A.A. Zadpoor, Bone tissue regeneration: the role of scaffold geometry, Biomaterials science 3(2) (2015) 231-245.

[42] M. Bohner, Y. Loosli, G. Baroud, D. Lacroix, Commentary: deciphering the link between architecture and biological response of a bone graft substitute, Acta biomaterialia 7(2) (2011) 478-484.

[43] M. Dias, P. Fernandes, J. Guedes, S. Hollister, Permeability analysis of scaffolds for bone tissue engineering, Journal of biomechanics 45(6) (2012) 938-944.

[44] I. Marcos-Campos, D. Marolt, P. Petridis, S. Bhumiratana, D. Schmidt, G. Vunjak-Novakovic, Bone

scaffold architecture modulates the development of mineralized bone matrix by human embryonic stem cells, Biomaterials 33(33) (2012) 8329-8342.

[45] H.-I. Chang, Y. Wang, Cell Responses to Surface and Architecture of Tissue Engineering Scaffolds, in: P.D. Eberli (Ed.), Regenerative Medicine and Tissue Engineering- Cells and Biomaterials, InTech2011, pp. 569-588.

[46] B.B. Mandal, A. Grinberg, E.S. Gil, B. Panilaitis, D.L. Kaplan, High-strength silk protein scaffolds for bone repair, Proceedings of the National Academy of Sciences 109(20) (2012) 7699-7704.

[47] D. Wendt, A. Marsano, M. Jakob, M. Heberer, I. Martin, Oscillating perfusion of cell suspensions through three-dimensional scaffolds enhances cell seeding efficiency and uniformity, Biotechnology and bioengineering 84(2) (2003) 205-214.

[48] P. Codogno, A.J. Meijer, Autophagy and signaling: their role in cell survival and cell death, Cell Death & Differentiation 12 (2005) 1509-1518.

[49] S.S. Kim, H. Utsunomiya, J.A. Koski, B.M. Wu, M.J. Cima, J. Sohn, K. Mukai, L.G. Griffith, J.P. Vacanti, Survival and function of hepatocytes on a novel three-dimensional synthetic biodegradable polymer scaffold with an intrinsic network of channels, Annals of surgery 228(1) (1998) 8.

[50] N.Q. Balaban, U.S. Schwarz, D. Riveline, P. Goichberg, G. Tzur, I. Sabanay, D. Mahalu, S. Safran, A. Bershadsky, L. Addadi, Force and focal adhesion assembly: a close relationship studied using elastic micropatterned substrates, Nature cell biology 3(5) (2001) 466-472.

[51] M.L. Gardel, I.C. Schneider, Y. Aratyn-Schaus, C.M. Waterman, Mechanical integration of actin and adhesion dynamics in cell migration, Annual review of cell and developmental biology 26 (2010) 315.

[52] C.S. Chen, J.L. Alonso, E. Ostuni, G.M. Whitesides, D.E. Ingber, Cell shape provides global control of focal adhesion assembly, Biochemical and biophysical research communications 307(2) (2003) 355-361.

[53] R. McBeath, D.M. Pirone, C.M. Nelson, K. Bhadriraju, C.S. Chen, Cell shape, cytoskeletal tension, and RhoA regulate stem cell lineage commitment, Developmental cell 6(4) (2004) 483-495.

[54] K. Anselme, Osteoblast adhesion on biomaterials, Biomaterials 21(7) (2000) 667-681.

[55] F.M. Watt, W.T. Huck, Role of the extracellular matrix in regulating stem cell fate, Nature reviews Molecular cell biology 14(8) (2013) 467-473.

[56] H. Tal, Introductory Chapter, Bone Regeneration InTech2012.

[57] E. Birmingham, G. Niebur, P. McHugh, Osteogenic differentiation of mesenchymal stem cells is regulated by osteocyte and osteoblast cells in a simplified bone niche (2012).

[58] A.M. Martins, C.M. Alves, R.L. Reis, A.G. Mikos, F.K. Kasper, Toward osteogenic differentiation of marrow stromal cells and in vitro production of mineralized extracellular matrix onto natural scaffolds, Biological Interactions on Materials Surfaces, Springer2009, pp. 263-281.

[59] O. Matsubara, E. Hase, T. Minamikawa, T. Yasui, K. Sato, In situ quantitative evaluation of osteoblastic collagen synthesis under cyclic strain by using second-harmonic-generation microscope, SPIE BiOS, International Society for Optics and Photonics, 2016, pp. 971222-971222-6.

[60] Q.L. Loh, C. Choong, Three-dimensional scaffolds for tissue engineering applications: role of porosity and pore size, Tissue Engineering Part B: Reviews 19(6) (2013) 485-502.

[61] W. Murphy, C. Simmons, D. Kaigler, D. Mooney, Bone regeneration via a mineral substrate and induced angiogenesis, Journal of dental research 83(3) (2004) 204-210.

[62] H. Wang, W. Zhi, X. Lu, X. Li, K. Duan, R. Duan, Y. Mu, J. Weng, Comparative studies on ectopic bone

formation in porous hydroxyapatite scaffolds with complementary pore structures, Acta biomaterialia 9(9) (2013) 8413-8421.

[63] X. Li, Y. Huang, L. Zheng, H. Liu, X. Niu, J. Huang, F. Zhao, Y. Fan, Effect of substrate stiffness on the functions of rat bone marrow and adipose tissue derived mesenchymal stem cells in vitro, Journal of Biomedical Materials Research Part A 102(4) (2014) 1092-1101.

[64] X. Yu, Z. Xia, L. Wang, F. Peng, X. Jiang, J. Huang, D. Rowe, M. Wei, Controlling the structural organization of regenerated bone by tailoring tissue engineering scaffold architecture, Journal of Materials Chemistry 22(19) (2012) 9721-9730.

[65] M. Witkowska-Zimny, K. Walenko, E. Wrobel, P. Mrowka, A. Mikulska, J. Przybylski, Effect of substrate stiffness on the osteogenic differentiation of bone marrow stem cells and bone-derived cells, Cell biology international 37(6) (2013) 608-616.

[66] J.A. Helsen, Y. Missirlis, Tissue Engineering: Regenerative Medicine, Biomaterials, Springer2010, pp. 269-289.

[67] T. Van Cleynenbreugel, J. Schrooten, H. Van Oosterwyck, J. Vander Sloten, Micro-CT-based screening of biomechanical and structural properties of bone tissue engineering scaffolds, Medical and Biological Engineering and Computing 44(7) (2006) 517-525.

[68] B.V. Krishna, S. Bose, A. Bandyopadhyay, Low stiffness porous Ti structures for load-bearing implants, Acta biomaterialia 3(6) (2007) 997-1006.

[69] W. Xue, B.V. Krishna, A. Bandyopadhyay, S. Bose, Processing and biocompatibility evaluation of laser processed porous titanium, Acta biomaterialia 3(6) (2007) 1007-1018.

[70] A. Bandyopadhyay, F. Espana, V.K. Balla, S. Bose, Y. Ohgami, N.M. Davies, Influence of porosity on mechanical properties and in vivo response of Ti6Al4V implants, Acta biomaterialia 6(4) (2010) 1640-1648.

[71] N.G. Mehr, X. Li, M.B. Ariganello, C.D. Hoemann, B.D. Favis, Poly (ε-caprolactone) scaffolds of highly controlled porosity and interconnectivity derived from co-continuous polymer blends: model bead and cell infiltration behavior, Journal of Materials Science: Materials in Medicine 25(9) (2014) 2083-2093.

[72] Y. Zhang, W. Fan, Z. Ma, C. Wu, W. Fang, G. Liu, Y. Xiao, The effects of pore architecture in silk fibroin scaffolds on the growth and differentiation of mesenchymal stem cells expressing BMP7, Acta biomaterialia 6(8) (2010) 3021-3028.

[73] P.Y. Huri, B.A. Ozilgen, D.L. Hutton, W.L. Grayson, Scaffold pore size modulates in vitro osteogenesis of human adipose-derived stem/stromal cells, Biomedical Materials 9(4) (2014) 045003.

[74] C. Wu, Y. Zhang, Y. Zhu, T. Friis, Y. Xiao, Structure–property relationships of silk-modified mesoporous bioglass scaffolds, Biomaterials 31(13) (2010) 3429-3438.

[75] P.K. Mattila, P. Lappalainen, Filopodia: molecular architecture and cellular functions, Nature reviews Molecular cell biology 9(6) (2008) 446-454.

[76] C. Jungreuthmayer, M.J. Jaasma, A.A. Al-Munajjed, J. Zanghellini, D.J. Kelly, F.J. O'Brien, Deformation simulation of cells seeded on a collagen-GAG scaffold in a flow perfusion bioreactor using a sequential 3D CFD-elastostatics model, Medical engineering & physics 31(4) (2009) 420-427.

[77] K. Matsuo, N. Irie, Osteoclast–osteoblast communication, Archives of biochemistry and biophysics 473(2) (2008) 201-209.

[78] F. Lecanda, D.A. Towler, K. Ziambaras, S.-L. Cheng, M. Koval, T.H. Steinberg, R. Civitelli, Gap

junctional communication modulates gene expression in osteoblastic cells, Molecular biology of the cell 9(8) (1998) 2249-2258.

[79] M.G. Vander Heiden, L.C. Cantley, C.B. Thompson, Understanding the Warburg effect: the metabolic requirements of cell proliferation, science 324(5930) (2009) 1029-1033.

[80] R.A. Carano, E.H. Filvaroff, Angiogenesis and bone repair, Drug discovery today 8(21) (2003) 980-989.

[81] A. Penk, Y. Förster, H.A. Scheidt, A. Nimptsch, M.C. Hacker, M. Schulz-Siegmund, P. Ahnert, J. Schiller, S. Rammelt, D. Huster, The pore size of PLGA bone implants determines the de novo formation of bone tissue in tibial head defects in rats, Magnetic resonance in medicine 70(4) (2013) 925-935.

[82] D.W. Hutmacher, M. Sittinger, M.V. Risbud, Scaffold-based tissue engineering: rationale for computer-aided design and solid free-form fabrication systems, TRENDS in Biotechnology 22(7) (2004) 354-362.

[83] A. Abarrategi, C. Moreno-Vicente, F.J. Martínez-Vázquez, A. Civantos, V. Ramos, J.V. Sanz-Casado, R. Martínez-Corriá, F.H. Perera, F. Mulero, P. Miranda, Biological properties of solid free form designed ceramic scaffolds with BMP-2: in vitro and in vivo evaluation, PloS one 7(3) (2012) e34117.

[84] J.Y. Park, D.H. Lee, E.J. Lee, S.-H. Lee, Study of cellular behaviors on concave and convex microstructures fabricated from elastic PDMS membranes, Lab on a Chip 9(14) (2009) 2043-2049.

[85] S. Scaglione, P. Giannoni, P. Bianchini, M. Sandri, R. Marotta, G. Firpo, U. Valbusa, A. Tampieri, A. Diaspro, P. Bianco, Order versus Disorder: in vivo bone formation within osteoconductive scaffolds, Scientific reports 2 (2012).

[86] J. Zhao, W. Han, H. Chen, M. Tu, S. Huan, G. Miao, R. Zeng, H. Wu, Z. Cha, C. Zhou, Fabrication and in vivo osteogenesis of biomimetic poly (propylene carbonate) scaffold with nanofibrous chitosan network in macropores for bone tissue engineering, Journal of Materials Science: Materials in Medicine 23(2) (2012) 517-525.

[87] X. Liu, M.N. Rahaman, Q. Fu, Bone regeneration in strong porous bioactive glass (13-93) scaffolds with an oriented microstructure implanted in rat calvarial defects, Acta biomaterialia 9(1) (2013) 4889-4898.

[88] T. Guda, J.A. Walker, B. Singleton, J. Hernandez, D.S. Oh, M.R. Appleford, J.L. Ong, J.C. Wenke, Hydroxyapatite scaffold pore architecture effects in large bone defects in vivo, Journal of biomaterials applications 28(7) (2014) 1016-1027.

[89] F. Guilak, D.M. Cohen, B.T. Estes, J.M. Gimble, W. Liedtke, C.S. Chen, Control of stem cell fate by physical interactions with the extracellular matrix, Cell stem cell 5(1) (2009) 17-26.

[90] D.A. Puleo, R. Bizios, Biological interactions on materials surfaces: understanding and controlling protein, cell, and tissue responses, Springer Science & Business Media2009.

[91] D.D. Deligianni, N. Katsala, S. Ladas, D. Sotiropoulou, J. Amedee, Y. Missirlis, Effect of surface roughness of the titanium alloy Ti–6Al–4V on human bone marrow cell response and on protein adsorption, Biomaterials 22(11) (2001) 1241-1251.

[92] D.D. Deligianni, N.D. Katsala, P.G. Koutsoukos, Y.F. Missirlis, Effect of surface roughness of hydroxyapatite on human bone marrow cell adhesion, proliferation, differentiation and detachment strength, Biomaterials 22(1) (2000) 87-96.

[93] R.A. Gittens, T. McLachlan, R. Olivares-Navarrete, Y. Cai, S. Berner, R. Tannenbaum, Z. Schwartz, K.H. Sandhage, B.D. Boyan, The effects of combined micron-/submicron-scale surface roughness and

nanoscale features on cell proliferation and differentiation, Biomaterials 32(13) (2011) 3395-3403.

[94] E.A. Nauman, K. Fong, T. Keaveny, Dependence of intertrabecular permeability on flow direction and anatomic site, Annals of biomedical engineering 27(4) (1999) 517-524.

[95] R. Bosco, J. Van Den Beucken, S. Leeuwenburgh, J. Jansen, Surface engineering for bone implants: a trend from passive to active surfaces, Coatings 2(3) (2012) 95-119.

[96] M. Navarro, A. Michiardi, O. Castano, J. Planell, Biomaterials in orthopaedics, Journal of the Royal Society Interface 5(27) (2008) 1137-1158.

[97] M.F. Ashby, D. Cebon, Materials selection in mechanical design, Le Journal de Physique IV 3(C7) (1993) C7-1-C7-9.

[98] D.E. Discher, P. Janmey, Y.-l. Wang, Tissue cells feel and respond to the stiffness of their substrate, Science 310(5751) (2005) 1139-1143.

[99] A.S. Mao, J.-W. Shin, D.J. Mooney, Effects of substrate stiffness and cell-cell contact on mesenchymal stem cell differentiation, Biomaterials 98 (2016) 184-191.

[100] S. Tan, J.Y. Fang, Z. Yang, M.E. Nimni, B. Han, The synergetic effect of hydrogel stiffness and growth factor on osteogenic differentiation, Biomaterials 35(20) (2014) 5294-5306.

[101] J. Lee, A.A. Abdeen, T.H. Huang, K.A. Kilian, Controlling cell geometry on substrates of variable stiffness can tune the degree of osteogenesis in human mesenchymal stem cells, Journal of the mechanical behavior of biomedical materials 38 (2014) 209-218.

[102] J.-P. Kruth, P. Mercelis, J. Van Vaerenbergh, L. Froyen, M. Rombouts, Binding mechanisms in selective laser sintering and selective laser melting, Rapid prototyping journal 11(1) (2005) 26-36.

[103] J.M. Sobral, S.G. Caridade, R.A. Sousa, J.F. Mano, R.L. Reis, Three-dimensional plotted scaffolds with controlled pore size gradients: effect of scaffold geometry on mechanical performance and cell seeding efficiency, Acta Biomaterialia 7(3) (2011) 1009-1018.

[104] F. Bobbert, K. Lietaert, A. Eftekhari, B. Pouran, S. Ahmadi, H. Weinans, A. Zadpoor, Additively manufactured metallic porous biomaterials based on minimal surfaces: A unique combination of topological, mechanical, and mass transport properties, Acta Biomaterialia (2017).

3

Rigid porous biomaterials

Porous biomaterials that simultaneously mimic the topological, mechanical, and mass transport properties of bone are in great demand but are rarely found in the literature. In this study, we designed and additively manufactured (AM) porous metallic biomaterials based on four different types of triply periodic minimal surfaces (TPMS). The topology, quasi-static mechanical properties, fatigue resistance, and permeability of the developed biomaterials were then characterized. The biomaterials showed a favorable but rare combination of relatively low elastic properties in the range of those observed for trabecular bone and high yield strengths exceeding those reported for cortical bone. This combination allows for simultaneously avoiding stress shielding, while providing ample mechanical support for bone tissue regeneration and osseointegration. Furthermore, as opposed to other AM porous biomaterials developed to date for which the fatigue endurance limit has been found to be 20% of their yield (or plateau) stress, some of the biomaterials developed in the current study show extremely high fatigue resistance with endurance limits up to 60% of their yield stress. It was also found that the permeability values measured for the developed biomaterials were in the range of values reported for trabecular bone.

3.1　Introduction

Porous biomaterials that mimic the various properties of bone are in great demand. That is due to their utility in substituting bone and their application in various types of orthopedic implants that need to avoid stress shielding while offering enough mechanical support and a long fatigue life. Moreover, the mass transport properties of bone-mimicking porous biomaterials such as their permeability have to be properly designed [1–3] to allow for nutrition and oxygenation of cells residing in the inner space of the porous biomaterials. Fully porous biomaterials provide multiple advantages as compared to other types of biomaterials [4]. These advantages include greater flexibility in adjustment of mechanical properties [5], increased surface area that could be used for bio-functionalization and infection prevention [6], and a large pore space that facilitates bone ingrowth and drug delivery from within the implants [7]. Design and manufacturing of porous biomaterials that simultaneously satisfy all the above-mentioned criteria in terms of mechanical and mass transport properties, are challenging enough but not necessarily sufficient for the desired level of bone tissue regeneration. Geometry in general, and the curvature of the surface on which cells reside in particular, has recently emerged as an important factor that determines the rate of tissue regeneration [8]. Multiple studies have, for example, shown that tissue regeneration increases with curvature and that tissue regeneration progresses much further on concave surfaces as compared to convex and flat surfaces [8–11].

Design and manufacturing of porous biomaterials whose curvature is most favorable for bone tissue regeneration have therefore received increasing attention to improve bone tissue regeneration. This coincides with recent advances in the additive manufacturing techniques. These advances enable the fabrication of tissue engineering porous biomaterials with arbitrarily complex geometries for an ever-expanding portfolio of biomaterials.

Minimal surfaces are mathematically rigorous concepts from the differential geometry of surfaces (Figure 1). In non-mathematical terms, minimal surfaces are like soap films. These films span a minimal surface area between given boundaries [12]. The specific property that makes minimal surfaces appealing for bone tissue regeneration is that they have a mean curvature of zero. A mean curvature of zero, as noted by others [13], resembles the mean curvature of trabecular bone, which is also known to be close to zero [14,15]. Moreover, minimal surfaces are frequently found in nature and tissues of a variety of species [16,17]. Examples, as nicely summarized by Kapfer *et al.* [17], include ''beetle shells, weevils, butterfly wing scales and crustacean skeletons'' [18–22]. It has been recently hypothesized that porous biomaterials based on minimal surfaces demonstrate enhanced bone tissue regeneration performance [8].

In the present study, we aimed to generate porous biomaterials based on triply periodic minimal surfaces (TPMS) (minimal surfaces with ''translational symmetries in three independent directions'' [12]) that present a unique combination of topological,

mechanical, and mass transport properties. With these properties they mimic the various properties of bone to an unprecedented level of multi-physics detail. Rational design and additive manufacturing were used to generate these biomaterials. The 'rational' design of biomaterials refers to the process of utilizing physical/biological principles and the established relationships between the topology of biomaterials and their performance to devise certain 'design criteria'. It is assumed that simultaneous satisfaction of relevant design criteria will result in improved bone tissue regeneration performance. The design process started from four different types of TPMSs and took a number of other design condensations into account to produce a large set of variations of porous biomaterials with different dimensions, porosities, and unit cell types. We used selective laser melting (SLM) for the production of metal porous biomaterials at the microscale. SLM is an additive manufacturing process in which successive addition of layers based on a computer-aided design (CAD) is used for free-form fabrication of three-dimensional metal parts. The biomaterials fabricated using SLM have precisely-controlled and highly reproducible micro-architectures. Both of those features are essential for realizing the advantages of rationally designed geometries. We studied the topological, quasi-static mechanical properties, fatigue resistance, and permeability of all types of the designed and additively manufactured porous biomaterials to evaluate their success in mimicking the various properties of bone.

3.2   Materials and Methods

3.2.1   Porous biomaterial design and manufacturing

Four TPMS structures, primitive (P), I-WP (I), gyroid (G), and diamond (D) were generated using k3DSurf, a software which provides all the options to produce complex 3D geometries in a finite volume with the use of implicit functions and inequalities. Because the only available file export option in K3Dsurf is .OBJ, a CAD converter software (MeshLab) was used to convert OBJ files to STL file format. Finally, STL files were imported to ABAQUS/CAE 6.13 [23]. By keeping the size of the unit cell constant (1.5x1.5x1.5 mm) and varying the sheet thickness of the TPMSs, four porosities between 43% and 77% per minimal surface type were designed. The porous biomaterials with the highest porosity to the lowest porosity are indicated by the numbers 500, 600, 700 or 800 that follow after P, I, G or D. For example, the P500 has the highest porosity of the primitive porous biomaterials and the P800 the lowest porosity.

Magics (Materialise, Belgium) was used to assemble the porous biomaterials based on the different TPMS unit cells. The open porous titanium (Ti6Al4V Grade 23 ELI) biomaterials were built on support structures with a customized version of the 3D Systems ProX DMP 320 machine at LayerWise N.V. (Belgium). Cylindrical specimens with a designed height of 20 mm and a diameter of 15 mm were produced (Figure 1).
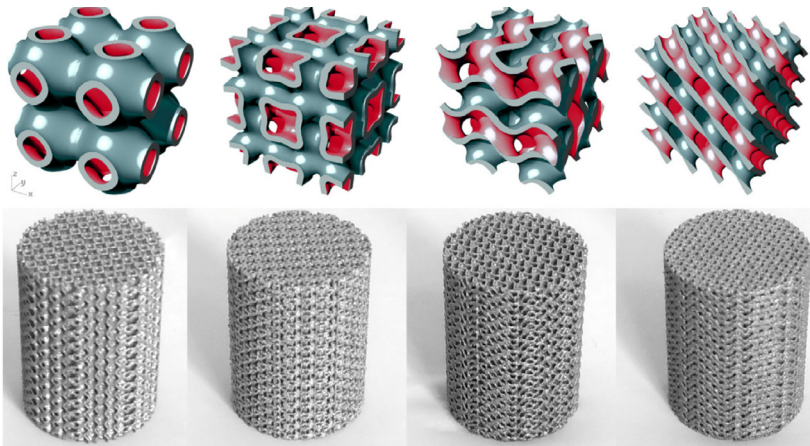
Figure 1: TPMS porous biomaterials. Top: STL file assemblies of 1.5 mm unit cells, bottom: cylindrical specimens with a height of 20 mm and a diameter of 15 mm manufactured with selective laser melting. From left to right: primitive, I-WP, gyroid, diamond.

3.2.2   Porous biomaterial morphology

The morphology of the porous biomaterials was characterized using micro-computed tomography (micro-CT) and the dry weighing method. Four samples of every type of porous biomaterial were scanned using a micro-CT scanner (Quantum FX, Perkin Elmer, USA).

A tube voltage of 90 kV, tube current of 180µA, a scan time of 3 min, and a voxel size of 60x60x60 mm^3 were used. This resolution was used because our micro-CT scanner has a field of view (FOV)-dependent spatial resolution. Therefore, it would not be possible to scan the whole porous biomaterials of 20 mm in length with higher resolutions (*e.g.*, a voxel size of 20 x 20 x 20 mm^3). If we used a higher resolution, the calculations would not be representative of the entire geometry. Furthermore, a voxel size of 60x60x60 mm^3 should be sufficient to capture the details of trabecular thickness and spacing as well as the porosity.

The projection images were reconstructed using built-in software of the scanner, and transferred to Analyze 11.0 software to obtain 2D slices, representing the cross-sections of the specimens. Fiji v.1.49s [24] in combination with the plugin BoneJ v.1.4.0 [25] was used for the segmentation of the images. First, the lower limit for the brightness level was adjusted to make sure only the Ti6Al4V was visible in the slices. Then the auto local threshold was applied, which computes the threshold value for each voxel within a specified radius in an 8-bit image. The Bernsen algorithm was selected with a radius of 6. This combination was chosen, because it gave the best results for the segmentation of the data when all algorithms available were evaluated by observation. After segmentation, circular regions of interests (ROIs) were created on the cross section of the specimens. The Fiji plugin BoneJ v.1.4.0 [25] was then used to three-dimensionally compute the morphological properties of the porous biomaterials. The porosity of porous biomaterials was determined using the ''volume fraction'' option, the pore size (*Tb.Sp*) and sheet thickness (*Tb.Th*) were retrieved with the ''thickness''

option. The surface area was obtained with the ''isosurface'' option using a resampling value of 3 and a threshold of 128, and the degree of anisotropy (DA) was determined with the default settings of the ''anisotropy'' option with a value of 20 for the minimum number of spheres and a tolerance of 0.0005.

The dry weighing method is based on the assumption that Ti6Al4V has a specific density of 4.51 g/cc. By weighing the specimen and dividing this mass by the mass of a solid cylinder with the same outer dimensions, the material percentage or apparent density (AD) of the specimen was determined. The porosity φ was defined as $\varphi = 1 - AD$.

3.2.3   Permeability

The permeability of the porous biomaterials was determined using experiments. Eq. (1) (Darcy's law) and Eq. (2) were used to determine the permeability and the Reynolds number (Re), respectively. The Reynolds number indicates whether the flow is laminar or turbulent. For porous media, the flow was assumed to be laminar if $1 < Re < 10$ [26]. The micro-CT data for the pore size was used as the pore diameter d (Table 2) to determine the Reynolds number (Eq. (2)).

$$\kappa = \frac{v \cdot \mu \cdot L}{\Delta P} \tag{1}$$

and

$$Re = \frac{v \cdot \rho \cdot d}{\mu} \tag{2}$$

where

κ	Permeability coefficient [m²]
μ	Dynamic viscosity coefficient of the fluid [Pa·s]
L	Height of the sample [m]
v	Darcy (superficial) velocity [m/s]
ΔP	Pressure difference [Pa]
Re	Reynolds number [–]
q	Density of the fluid [kg/m³]
d	Diameter of the pore [m]

3.2.3.1   Permeability measurements

The falling head method was used in the permeability experiments. In this method, a column

above the sample provides the water head. A vacuum pump was used to fill this column with water. When the column was filled, the air valve was opened and the water flowed back into the tank through the sample (Figure 2). The samples were wrapped with heat shrink tubing and then pressed into a rubber holder to ensure a tight fit and to prevent leakage on the sides. The water pressure at the bottom of the column was measured just above the porous biomaterial with a pressure gauge and registered every second in LabView (v.11.0).

Four samples of every type of porous biomaterial were used in the permeability experiments. The process described above was repeated five times for every sample, resulting in twenty measurements for every specimen. Six steps were taken to derive the permeability from the experimental results.

1. The difference in water level per second within the water column was used to determine the fluid velocity within the column $v_{column} = \dfrac{\partial h}{\partial t}$, where h is calculated from the measured pressure using Eq. (4b).

2. The volumetric flow rate was computed by multiplying this velocity by the cross-sectional area of the column (A_{column}), perpendicular to the flow direction.

3. The volumetric flow rate (Q) was divided by the cross-sectional area of the specimen ($A_{biomaterial}$) to derive the flow velocity through the sample.

4. In the graph where the pressure drop ΔP (Eq. (4)) was plotted as a function of the velocity of the fluid through the specimen ($v_{biomaterial}$), a power law ($R^2 > 0.998$) was fitted to the data. This power law was then used to extrapolate the data for velocities close to 0 m/s.

5. The Reynolds number was computed using Eq. (2), where v is defined in Eq. (3).

6. In the region where the Reynolds number was between $Re = 1$ and $Re = 10$, which is the laminar regime in porous media, Darcy's law could be applied [26]. For all specimens, the slope in this region was computed. As described in Darcy's law, this slope is equal to the reciprocal of the permeability κ, multiplied by the dynamic viscosity coefficient (μ) and the length of the specimen (L) (*i.e.,* $\dfrac{\mu L}{\kappa}$).

The steps described are summarized in Darcy's law (Eq. (1)), where v and ΔP are defined as:

$$v = v_{biomaterial} = \frac{v_{column} \cdot A_{column}}{A_{biomaterial}} \tag{3}$$

and

$$\Delta P = P_{measured} - \rho \cdot g \cdot L \tag{4}$$

where

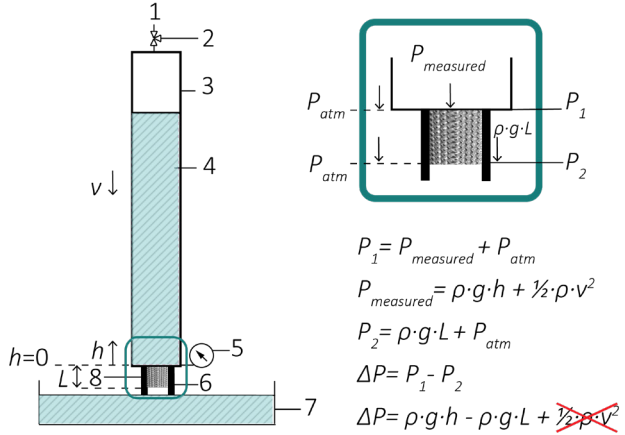|	
$v_{biomaterial}$	Fluid velocity through the specimen [m/s]
v_{column}	Fluid velocity within the column [m/s]
A_{column}	Cross sectional area of the column [m²]
$A_{biomaterial}$	Cross sectional area of the specimen [m²]
h	Water level within the column [m]

Figure 2: Permeability experiment set-up: Left: picture of the set-up. Center: Schematic overview 1. vacuum pump, 2. air valve, 3. water column, 4. water, 5. pressure gauge, 6. sample holder, 7. water container, 8. sample. Right: pressure difference over the sample [Pa], with h - water level within the column [m], L - Length of the sample [m], ρ - density of the water [kg/m³], g - gravitational acceleration [m/s²], P_{atm} - atmospheric pressure [Pa], v - fluid velocity within the column [m/s]. The kinetic terms ($1/2 \cdot \rho \cdot v^2$) is negligible because this term is relatively small compared to the pressure applied by the water ($\rho \cdot g \cdot h$).

Because the kinetic term $\left(\frac{1}{2} \cdot \rho \cdot v^2 \right)$ in $P_{measured} = \rho \cdot g \cdot h + \frac{1}{2} \cdot \rho \cdot v^2$ was relatively low compared to the pressure of the water within the column, this term was neglected.

Hence, $P_{measured} = \rho \cdot g \cdot h$ (4b). The values for the used parameters are summarized in Table 1.

Symbol	Parameter	Value	SI Unit
ρ	Density of water	10^3	[kg/m³]
μ	Dynamic viscosity of water	10^{-3}	[Pa·s]
L	Length of the specimen	20×10^{-3}	[m]
A_{column}	Cross sectional area of the column	1.26×10^{-3}	[m²]
$A_{biomaterial}$	Cross sectional area of the specimen	1.77×10^{-4}	[m²]
g	Gravitational acceleration	9.81	[m/s²]

Table 1. Parameters and their values used in the Darcy's law and the equation for the Reynolds number for the permeability experiments.

3.2.4   Mechanical tests

Nine samples of every type of porous biomaterial were used for the mechanical tests. Six samples were subjected to static compression (*i.e.,* three with and three without lubrication). Another three samples were used for compression-compression fatigue tests.

3.2.4.1   Static mechanical testing

The static mechanical tests were carried out using an Instron 5500R mechanical testing machine with a 100 kN load cell and Bluehill v3.61 software to control the machine and record the measurements. According to the standard for compression of porous and cellular metals (ISO 13314 [27]), a constant deformation rate of 10^{-2}/s should be applied to the samples. This corresponds to 1.2 mm/min for all samples with a height of 20 mm. The sample was placed between two flat hard metal machine platens and only vertical movement was allowed. When the limit of 99 kN, or a displacement of 16 mm was reached, the test was terminated. The strain was measured by the displacement of the crossheads. As described in ISO 13314 [27], the plateau stress (σ_{pl}) was determined as the arithmetical mean of the stresses between 20% and 30% compressive strain. The quasi-elastic gradient was determined by the slope between the strains and stresses within the elastic region of the stress-strain curve. The yield stress (σ_y) was found by the intersection of the stress-strain curve and a line parallel to the quasi-elastic gradient line at a strain offset of 0.2%. During the static mechanical tests, barreling was observed in some samples. Barreling is a defect caused by friction at the interface of the machine platens and the end surfaces of the specimen, and causes the sample to become barrel-shaped. To determine if this defect could be reduced by reducing the friction at the interface, tests with and without molybdenum disulfide (MoS2) lubricant at the interface of the platens and the end surfaces of the specimen were performed.

3.2.4.2   Fatigue mechanical tests

A Materials Test System (MTS) testing machine was used for compression-compression fatigue experiments. Three samples of every type of porous biomaterial were tested at a constant force ratio R = 0.1 ($R = F_{min}/F_{max}$, where F_{min} and F_{max} are the applied minimum and maximum forces, respectively [28]) using a sinusoidal waveform at a frequency of 15 Hz. The maximum force (F_{max}) applied during the fatigue tests was equal to 60% of the yield stress (σ_y). This value was derived from the static mechanical tests without lubricant. The test was terminated when the sample was fractured or when 10^6 cycles were reached without macroscopic failure of the specimen. When the deviation from the mean number of cycles to failure was higher than 40% between the samples tested for a single load level, a fourth sample was tested. To see the cracks within the specimens after fatigue testing, one sample of every TPMS geometry was embedded. The embedded samples were ground with P320, P800 and P1200 SiC paper, polished with 3 mm diamond suspension, and observed using an

Olympus BX60M light optical microscope (LOM).

3.3 Results

3.3.1 Morphology of the porous biomaterials

For every unit cell, the porosity decreases with increasing sheet thickness and the surface area decreases with decreasing porosity (Table 2). The porosities measured with the dry weighing method lay between 71–49%, 65–44%, 66–52% and 60–44% for the primitive, I-WP, gyroid and diamond porous biomaterials, respectively. These values are comparable to the porosities of the design porosity and the values retrieved from the micro-CT scans (Table 2). A lower surface area was observed for the primitive and diamond specimens compared to the I-WP and gyroid specimens. During the analysis of the micro-CT images, spheres with a maximum size were fitted into the sheets and pores (Figure 3) to determine their size. In general, the pore size decreases with increasing sheet thickness and decreasing porosity. Porous biomaterials with a similar porosity such as P700, I600, G700, and D600, show different values for the sheet thickness, pore size and surface area (Table 2).
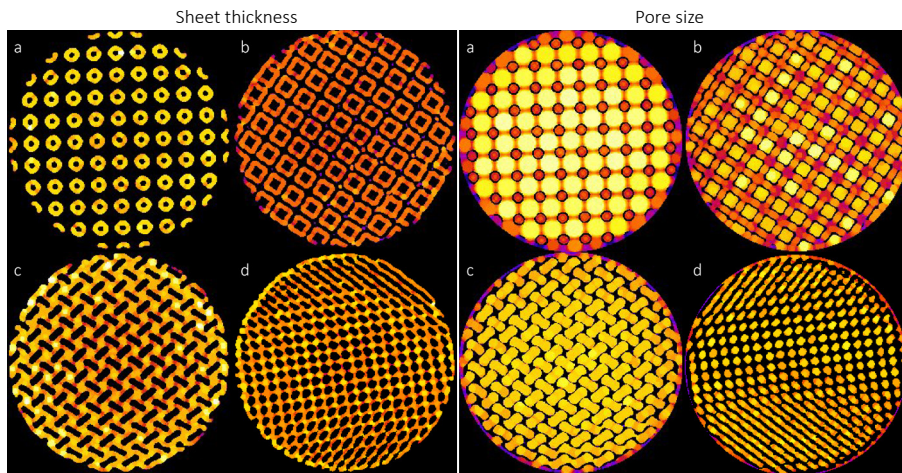

Figure 3. Micro-CT images of the sheet thickness and pore size. Sheet thickness: maximal spheres fitted into sheets. Pore size: maximal spheres fitted into pores. a. P500, b. IWP500, c: G500, d. D500.

3.3.2 Permeability values

Sixty-four samples were tested experimentally (four samples of every type of TPMS geometry with four different apparent densities). The measurements were repeated five times for every sample, resulting in twenty measurements for every type of porous biomaterial. A graph with the pressure drop ΔP as a function of flow velocity v through the sample was used to determine

	Porosity φ [%]				Sheet thickness [µm] (Tb.Th.)					Pore size [µm] (Tb.Sp.)		Surface area [µm²]		DA	
	Design	Dry weight	Micro CT	SD	Design	Micro-CT from top	SD	Micro-CT from side	SD	Micro-CT	SD	Micro-CT	SD	Micro-CT	SD
P500	77	71	71	0.59	216	244	33	246	30	896	240	1.26E+10	1.25E+08	0.36	0.01
P600	62	60	61	0.67	294	320	39	321	37	823	237	1.12E+10	5.46E+07	0.29	0.02
P700	56	55	56	0.81	333	349	39	351	36	791	244	1.07E+10	3.98E+07	0.27	0.03
P800	50	49	50	0.29	381	398	43	400	41	722	244	1.03E+10	5.37E+07	0.20	0.01
I500	65	65	54	0.50	155	271	41	275	38	392	99	1.72E+10	3.52E+08	0.13	0.01
I600	57	56	49	1.16	196	298	49	304	47	390	121	1.58E+10	5.20E+08	0.20	0.03
I700	52	52	45	1.28	221	326	56	330	53	383	126	1.43E+10	3.79E+08	0.17	0.04
I800	44	44	39	0.42	250	362	64	367	62	361	130	1.29E+10	4.50E+08	0.18	0.04
G500	69	66	62	0.93	169	258	41	261	39	464	72	1.62E+10	1.12E+08	0.25	0.09
G600	63	62	58	0.74	178	272	38	272	37	458	76	1.58E+10	1.72E+08	0.30	0.01
G700	57	58	54	1.20	230	295	39	296	38	435	75	1.47E+10	2.77E+08	0.26	0.02
G800	51	52	48	0.80	261	330	41	332	40	406	76	1.38E+10	1.41E+08	0.24	0.00
D500	61	60	47	0.52	163	292	37	291	38	370	58	1.82E+10	1.13E+08	0.30	0.01
D600	57	52	41	1.85	196	375	67	370	67	429	99	1.12E+10	3.42E+08	0.26	0.01
D700	49	48	37	0.90	203	430	63	428	66	427	99	1.06E+10	3.75E+08	0.26	0.02
D800	43	44	35	0.33	247	444	61	442	66	413	98	1.01E+10	1.81E+08	0.21	0.01

Tb.Th., trabecular thickness, *Tb. Sp.*, trabecular spacing, *DA*, degree of anisotropy

Table 2. Morphological parameters of the different types of porous biomaterials. *Tb.Th.*, trabecular thickness, *Tb. Sp.*, trabecular spacing, *DA*, degree of anisotropy.

the experimental values for the laminar region. The permeability values (Figure 4) were found to be dependent on the apparent density of the porous biomaterials (i.e., the permeability decreases with increasing apparent density). Furthermore, the permeability depended on the geometry of the unit cell, regardless of the apparent density of the specimens (Figure 4). For example, the I-WP specimens have a lower permeability than the diamond specimens up to an apparent density of 43%. It was found that the permeability decreases with increasing
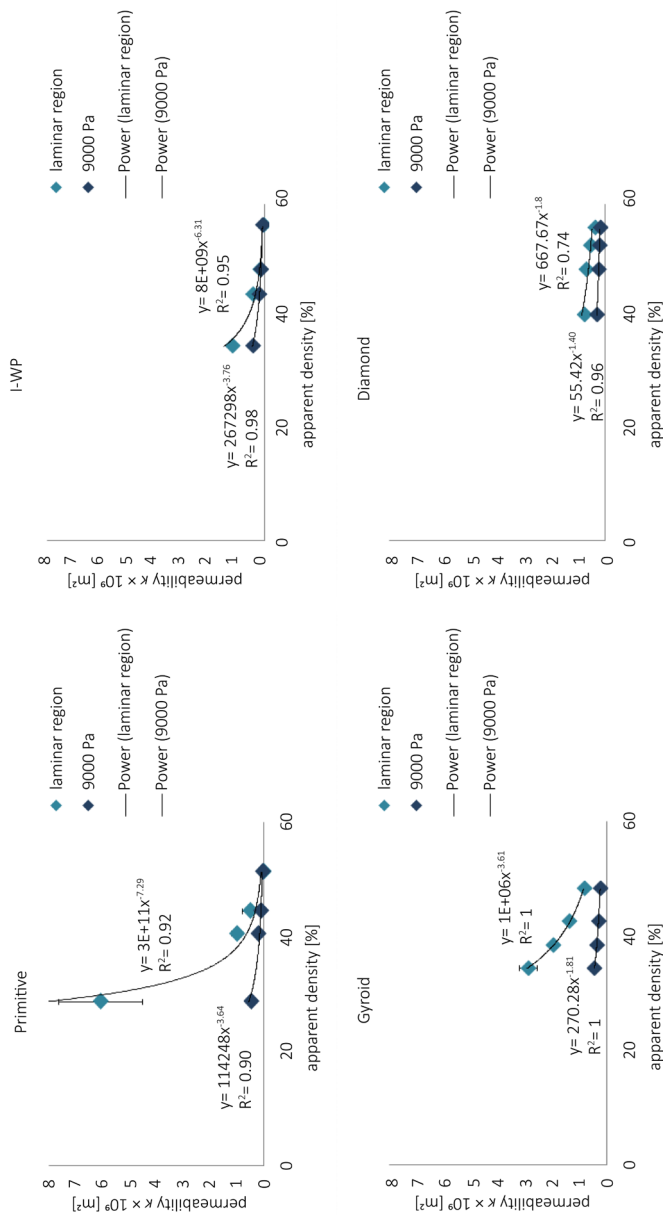
Figure 4. Permeability values derived from the experiments for the different apparent densities of the TPMS porous biomaterials. Green and blue dots represent the permeability values obtained from the laminar region $1 < Re < 10$ and for a pressure gradient of 9000 Pa (turbulent flow).

flow velocities due to growing inertial effects (Figure 4). The highest ($6.1 \times 10^{-9}\,m^2$) and lowest ($5.5 \times 10^{-11}\,m^2$) permeability values for the laminar regime were found for the P500 and I800 samples, respectively. For a pressure difference of 9000 Pa, the permeability varied between $4.9 \times 10^{-11}\,m^2$ and $4.8 \times 10^{-10}\,m^2$.

3.3.3   Mechanical tests
3.3.3.1 Static mechanical tests

Nine samples of every type of porous biomaterial were used for the mechanical tests. Six samples were subjected to static compression with or without lubricant (three for each test) and three to compression-compression fatigue tests. The stress-strain curves obtained
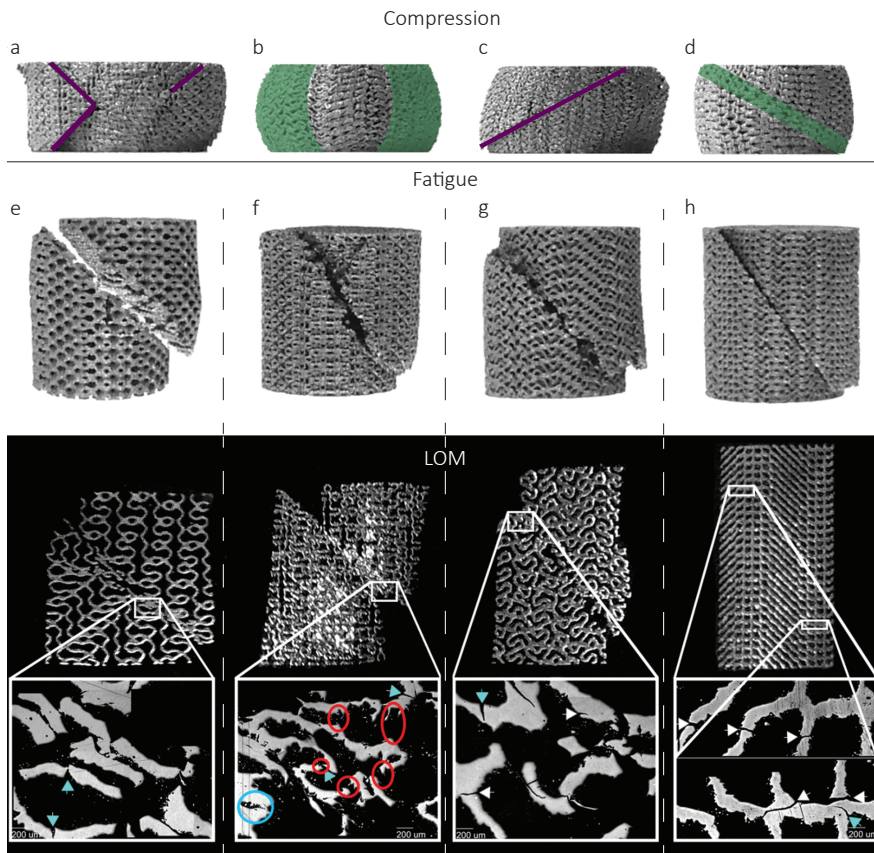
Figure 5. Compression – Different failure modes of samples during the static compression tests. a. shear lines (purple) in different directions, b. barreling (green), c. one shear line (purple), d. diagonal collapsing (green) of layers. Fatigue – Shear failure at 45 degrees of specimens after fatigue tests and LOM images of embedded samples. The pink dashed line shows the boundary of one unit cell. The white arrows indicate the initiation of crack formation. The blue arrows indicate crack formation from the inside of the unit cell. The circles in the LOM images of the I-WP specimen (f) indicate examples of crack formation due to manufacturing imperfections (blue) and weak parts of the structure (red). e. primitive, f. I-WP, g. gyroid, h. diamond.

from the static compression tests were used to derive different mechanical properties. These include the plateau stress σ_{pl}, quasi-elastic gradient, and yield stress σ_y. The values shown in the following graphs are the averages of the three samples of every type of porous biomaterial used for the tests.

Different failure modes were observed for the different types of porous biomaterials during the static compression tests (Figure 5 Compression). These failure modes are dependent on the geometry of the unit cell and could be related to the stress-strain curves
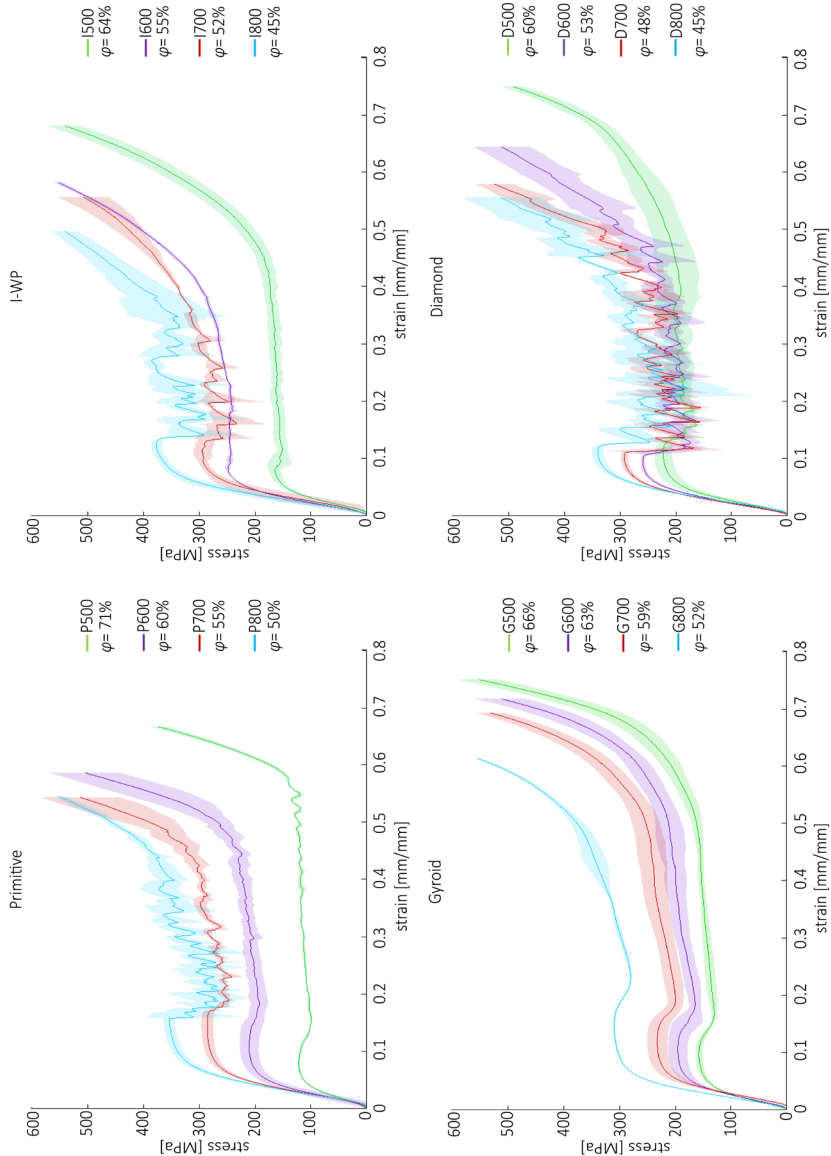
Figure 6. Stress-strain curves for the primitive, I-WP, gyroid and diamond specimens with four different porosities of the static compression tests performed with a strain rate of 1.2 mm/s. The shadow around the curves represents the standard deviation from the mean of three samples.

61

(Figure 6). All primitive and gyroid specimens, and I-WP specimens with a low apparent density showed barreling. In this case, the mid height of the sample was bulging out and layers collapsed onto each other (Figure 5b). The I-WP with a higher apparent density and all diamond specimens failed due to shear band localization (Figure 5a, c). One or multiple shear bands (Figure 5a, c) were observed in these specimens. In the primitive specimens with the highest density, shear bands were visible, but no shear fracture occurred (Figure 5d Compression).

The stress-strain curves were typical for porous biomaterials [29,30] with the same
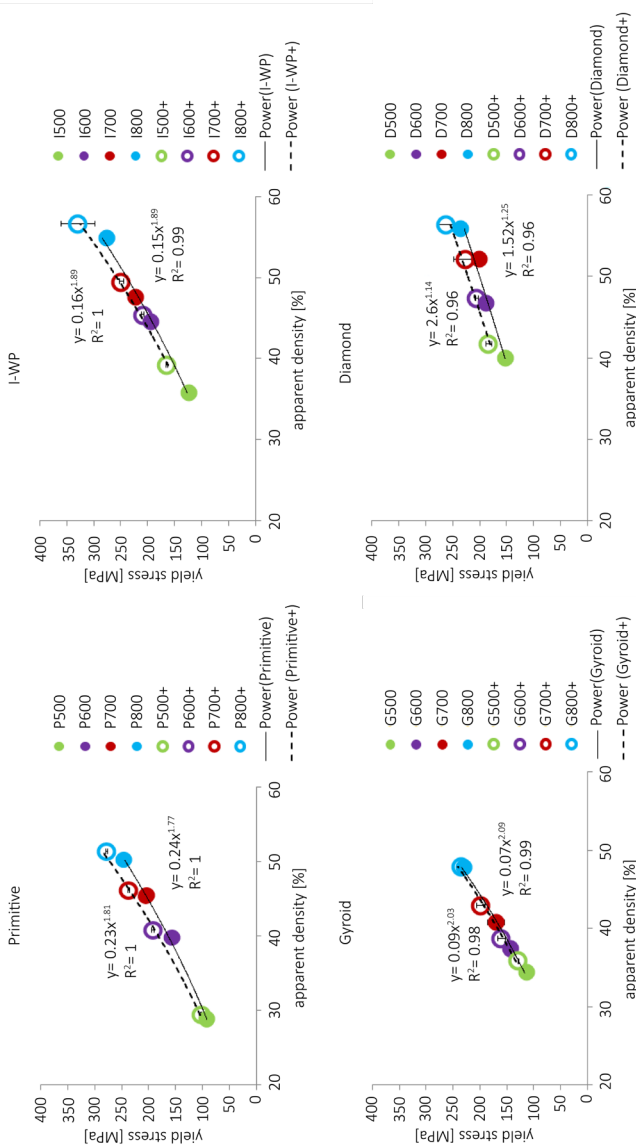
Figure 7. Yield stress for the different porosities of the primitive, I-WP, gyroid, and diamond porous biomaterials. The '+' sign indicates the values of the tests with MoS2 lubricant.

stages of deformation and same features including the linear increase in stress with strain, a relatively long plateau region with fluctuating stresses, and finally a region of rapid increase in stress (Figure 6).

It was observed that the peaks and valleys in the stress-strain curves (Figure 6) were caused by the formation of shear lines and the build-up of stresses after the load was transferred to neighboring sheets or unit cells. The stress-strain curves of the diamond specimens (Figure 6) have a short yield plateau, after which the curves demonstrated large levels of irregularity due to shear fracture of the samples.
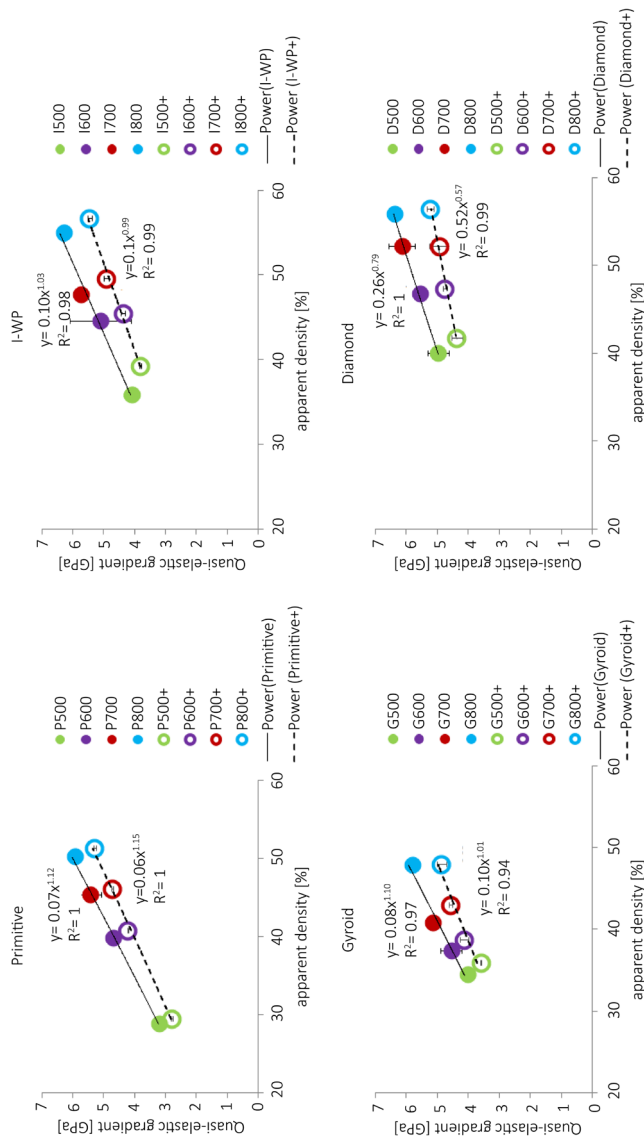

Figure 8. Quasi-elastic gradient for the different porosities of the primitive, I-WP, gyroid and diamond specimens. The '+' sign indicates the values of the tests with MoS2 lubrication.

The stress-strain curves remained largely similar when the samples were tested with or without lubricant (Figure 6). Some samples of the D700 and D800 failed under pure shear before 20% strain was reached. Because the plateau stress σ_{pl}, is defined as the mean stress between 20% and 30% strain, these values are based on only one or two measurements.

For all types of porous biomaterials, the yield stress σ_y, and plateau stress σ_{pl}, increased with increasing apparent density (Figure 7). A slightly higher plateau stress was observed for the samples tested with lubricant. The values of the quasi-elastic gradient of the primitive,
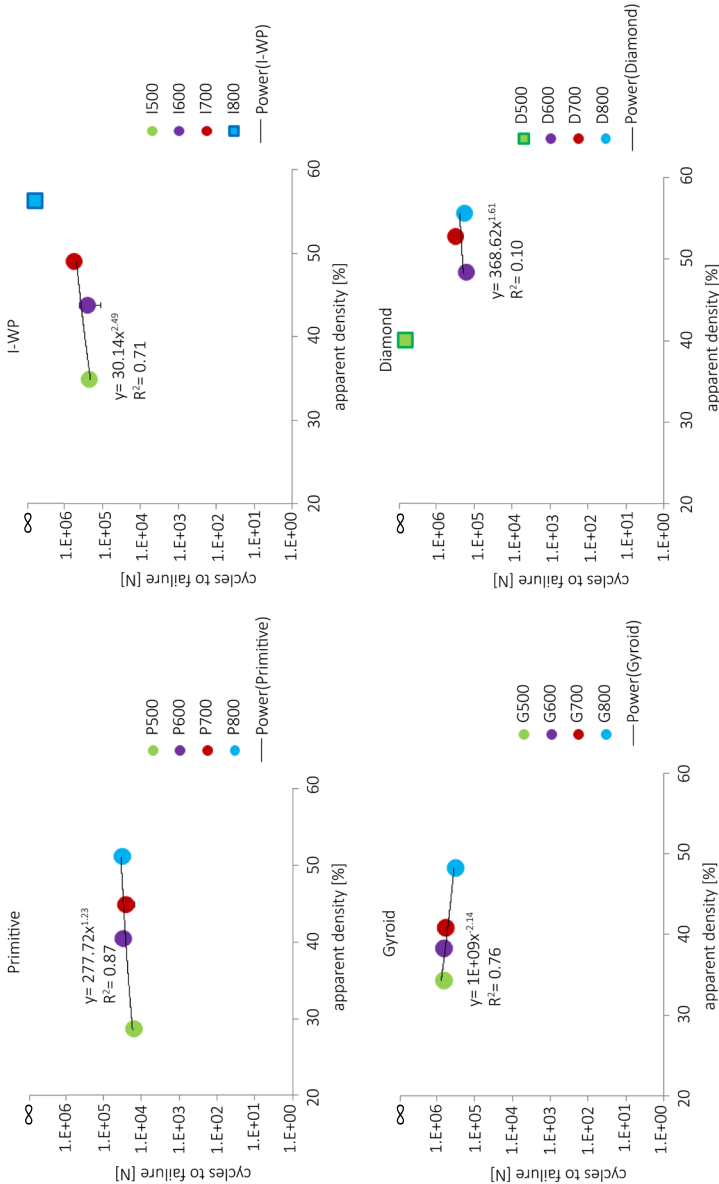

Figure 9. Number of cycles to failure for the different apparent densities of the primitive, I-WP, gyroid and diamond specimens. The blue and green square markers for the I800 and D500 in the I-WP and diamond figures indicate that these samples were still intact after 10^6 cycles.

I-WP, and gyroid samples tested without lubricant increased almost linearly with increasing apparent density (Figure 8). For all porous biomaterials, the values for the quasi-elastic gradient were reduced with the application of lubricant.

3.3.3.2 Fatigue behavior of the porous biomaterials

The primitive specimens showed the shortest fatigue life with a maximum amount of approximately 3×10^4 cycles. The fatigue life of the I-WP, diamond and gyroid specimens varied between 1×10^5 and 7×10^5 cycles. It was observed that the primitive and I-WP specimens show a slight increase in cycles to failure as the apparent density increased, while the opposite held for the gyroid specimens (Figure 9). Generally, the fatigue samples of all types of unit cells failed under a 45° angle (Figure 5 LOM). Two types of specimens from the diamond and I-WP structures, namely the D500 and I800, were still intact after 1×10^6 cycles (Figure 9).

In the primitive and gyroid specimens, crack initiation was observed at the inside of the unit cells (Figure 5 LOM). The optical microscopy images of the I-WP show crack development at manufacturing imperfections and small pores in the bulk material (Figure 5 LOM). The weak parts of the geometry seem to be the connections between two unit cells, and the vertical and horizontal sheets. Although no macroscopic damage of the diamond (D500) specimens was observed after 1×10^6 cycles, cracks were present. These cracks initiated in the sheets at the periphery of the specimen and propagated to the center via the vertical sheets (Figure 5, LOM). Cracks were also visible in the intersections of the horizontal and vertical sheets (Figure 5, LOM).

3.4   Discussion

AM porous metallic biomaterials based on four different types of triply periodic minimal surfaces and with relatively wide range of relevant porosities were developed in the current study. The results of the characterization test introduced earlier show that the developed biomaterials present an interesting combination of morphological properties, quasi-static mechanical behavior, fatigue resistance, and permeability. These properties make them excellent bone-mimicking biomaterials that can withstand fairly large deformations (>0.5 %) and exhibit exceptionally high fatigue strength. These results make them potential candidates as bone-mimicking orthopedic implant designs and bone-substituting biomaterials.

3.4.1   Morphological properties

The morphological properties of the porous structures characterized using micro-CT and dry weighing are very close to their design values. That is an important point given the fact that the specific design morphology of minimal surfaces (i.e., a mean curvature of zero) needs

to be preserved after the additive manufacturing process, to make sure the morphology resembles that of trabecular bone. Additive manufacturing of such complex geometrical surfaces at the micro-scale is quite challenging. This is partially caused by the different and continuously changing orientation of the plate-like structures that constitute the micro-architecture of such biomaterials. For example, specific parts of the micro-architecture of some of the minimal surfaces are in parallel with the powder bed while the other regions make a certain angle with the powder bed. Proper solidification of the melted powder to yield fully solid (i.e., pore-free) bulk (i.e., matrix) material is particularly difficult for the horizontal parts of micro-architecture [31] due to the disruption of heat transfer by the powder bed. Moreover, the parameters used for the horizontal parts of the micro-architecture may not work for the other parts of the micro-architecture with different orientation. Therefore, the laser processing parameters had to be optimized for every porosity of every type of minimal surface. This was done during an extensive parametric study to make sure the bulk material constituting the porous biomaterial contained the least possible number of pores.

Specific requirements have been laid out through past research regarding the morphological properties that are required for maximum bone tissue regeneration performance of biomaterials. One important parameter is the pore size whose effect on tissue regeneration performance have been extensively researched. Through extensive review of the past research, Karageorgiou and Kaplan [32] identified a recommended pore size of >300 μm. Micro-CT analysis showed that the actual pore sizes of all AM porous biomaterials developed here are above 300 μm.

When comparing the morphological properties of the AM porous biomaterials developed here and those of the trabecular bone (Table 3), it is clear that trabecular spacing (pore size) is well within the range of the values reported for bone. The BV/TV values found for TPMS also overlaps with the values reported for trabecular bone in a few other studies (Table 3). The trabecular thickness values measured for AM porous biomaterials are somewhat higher than those observed for trabecular bone (Table 3). However, the largest difference is between the degree of anisotropy of the AM porous biomaterials presented here and those reported for trabecular bone in the literature (Tables 2 and 3). The AM porous biomaterials based on TPMS are much more isotropic than the native bone tissue. The effect of this difference on the process of bone tissue regeneration is difficult to predict. Anisotropy in native bone tissue is thought to be related to the need for maximizing stiffness and strength in the main loading direction, while keeping the bone mass as low as possible. The above-mentioned concerns may be less applicable in the case of metallic biomaterials where the strength and stiffness of the bulk material, from which the porous structures are made, are much higher than those of bone tissue.

In addition to surface properties [33–36] and functional groups [37,38] that are known to profoundly affect the bone tissue regeneration process, curvature has been identified recently as a parameter influencing tissue regeneration [8–11,13]. The sign and magnitude

	TPMS	Various regions [68]	Calcaneus [69]	Femoral head [69]	Iliac crest [69]	Lumbar spine [69]	Femoral neck [70]	Greater trochanter [70]	Vertebra [70]	Iliac crest [71]
BV/TV	0.29 - 0.61	0.06 - 0.36	0.05 - 0.19	0.08 - 0.32	0.06 - 0.28	0.04 - 0.12	0.25 ± 0.06	0.10 ± 0.02	0.11 ± 0.03	0.20
Tb.Th. [µm]	244 - 444	100 - 190	102 - 169	120 - 257	101 - 225	82 - 157	178 ± 27	133 ± 14	141 ± 17	100
Tb.Sp. [µm]	361 - 896	320 - 1670	546 - 982	480 - 984	523 - 1306	612 - 1269	620 ± 82	966 ± 146	922 ± 151	395
DA	0.13 - 0.36	1.11 - 2.54	1.36 - 2.17	1.27 - 2.18	1.17 – 1.97	1.16 – 1.96	-	-	-	-

Table 3. Comparison between the morphological properties of the AM porous biomaterials presented here and those of trabecular bone from the different regions of the human body.

	TPMS	Different regions of the human body/region	Vertebra	Proximal tibia	Greater trochanter	Femoral neck	Femur	Proximal femur
E [MPa]	3200 -6400	16 – 1113 (T) [68] 10 – 1570 (T) [72] 5000 – 23000 (C) [72]	90 – 536 (T) [73] 100 – 800 (T) [40]	200 – 2800 (T) [40] 445 ± 257 (T) [74]	200 – 1500 (T) [40]	750 – 4500 (T) [40]	389 ± 270 (T) [75] 16700 (C) [76]	441 ± 271 (T) [77]
σ_y [MPa]	92 – 276	164 – 240 (C) [72]	0.56 – 3.71 (T) [73]	-	-	55.3 ± 8.6 (T) [40]	122.3 (C) [76]	-
$\kappa \times 10^{-9}$ [m^2]	0.05 – 6.10	-	8.05 ± 4.75 (T) [57]	0.467 – 14.8 (T) [78]	-	-	-	2.76 ± 1.91 (T) [57]

Table 4. Comparison between the mechanical and physical properties of AM porous biomaterials based on TPMS and those of human bone tissue.

of surface curvature are shown to drastically influence the size and rate of tissue regeneration [8–11,13]. An important bone-mimicking aspect of the AM porous biomaterials presented here is the fact that they mimic the curvature characteristics of trabecular bone. The mean curvature of trabecular bone is close to zero [14,15], which is the same as the mean curvature of minimal surfaces. The effects of curvature on tissue regeneration have been explained through the mechanotransduction pathways that involve curvature-induced tensile stresses [9,10,13,39] and might result in the reorganization of the cytoskeleton. There is therefore a mechanistic connection between the potential mechanism through which minimal surfaces could improve bone tissue regeneration performance and the mechanotransduction pathways of curvature-driven tissue regeneration. Indeed, a computational model describing the effects of curvature on tissue regeneration used geometries that could evolve to become minimal surfaces [13].

3.4.2   Quasi-static mechanical properties

The mechanical behavior of the developed biomaterials in terms of their quasi-static mechanical properties and fatigue resistance were studied. Also the fluid flow properties of the associated porous structures were characterized in terms of permeability. The quasi-elastic gradient of the developed porous biomaterials, which is the closest concept to elastic modulus in the study of the mechanical behavior of porous biomaterials, was found to be between 3.2 and 6.4 GPa. The above-mentioned range largely overlaps with the higher end of the apparent elastic moduli reported for trabecular bone in a study by Morgan et al. [40] (Table 4). They evaluated trabecular bone from different areas in the body with varying apparent densities that showed elastic moduli between 0.1 and 4.5 GPa (Table 4) [40]. The quasi-elastic modulus of the AM porous biomaterials was also close to the lower end of the elastic modulus of cortical bone reported in the literature (*e.g.*, see values reported in Ref. [41] (Table 4)). In terms of yield stress, the values measured for the AM porous biomaterials were similar to some values measured for cortical bone [42] and generally higher than those measured for trabecular bone [43] (Table 4). The plateau stress is also generally higher for the biomaterials developed here as compared to the compressive strength values reported for both trabecular and cortical bone [42–44]. The AM porous biomaterials based on triply periodic minimal surfaces therefore show a combination of relatively low elastic moduli which are in the range of those observed for trabecular and cortical bone and relatively high yield stress and compressive strength. This is a desirable combination for bone-substituting biomaterials because the relatively low elastic modulus ensures the minimal chance of stress shielding. Stress shielding occurs when an implant with a higher stiffness carries more load than the bone around the implant. This leads to bone resorption and eventually implant failure [45]. Because the quasi-elastic gradient (*i.e.*, stiffness of the porous biomaterials studied here) is within the range of the stiffness of bone, stress shielding is less likely to occur. At the same time, the relatively high mechanical strength of the bone-substituting

biomaterial provides enough mechanical support and prevents the biomaterial to fail under mechanical loading. Given the fact that the elastic modulus and mechanical stress are positively correlated with each other for most naturally occurring materials, it is often impossible to develop biomaterials that show low enough elastic modulus while preserving high mechanical strength.

The rationally designed biomaterials presented in the current study, although based on minimal surfaces, could combine both desired features. This is partially due to their sheet-based micro-architectures structure as compared to strut-based (i.e., beam-based) micro-architectures that are used in development of many other types of porous biomaterials. These findings are in line with the previous findings that the ratio of yield strength to elastic modulus is dependent on the micro-architecture of porous biomaterials [46].

It is also important to note that friction could play an important role in determining the quasi-static mechanical properties of AM porous biomaterials. The use of a consistent testing protocol with sufficient lubrication to minimize the friction is therefore recommended, particularly when one is interested the in large deformation behavior of the biomaterials.

3.4.3 Fatigue behavior

One of the limitations of most AM porous biomaterials developed to date is their relatively low fatigue resistance. In many studies, the endurance limit (the stress level for which the number of loading cycles before failure exceeds a certain threshold (*e.g.*, 1×10^6 cycles) of such biomaterials is found to be below 20% of the plateau (or yield) stress [47,48]. An important property of the AM porous biomaterials developed in the current study is their extremely high fatigue resistance as compared to comparable AM porous biomaterials developed during the recent years. When loaded at a stress level as high as 60% of their yield stress, the number of cycles to failure is more than the specified threshold (*i.e.*, 1×10^6 cycles) for some of the porous structures developed in the current study (*e.g.*, I800 and D500). Once a specimen has endured more than the specified number of loading cycles, fatigue tests are usually stopped and the specimens are assumed to have indefinite fatigue life for all practical purposes.

With a value as high as 60% of their yield stress as their endurance limit, the maximum endurance limit of these porous structures is at least three times higher than that of AM porous metallic biomaterials developed before. A threshold of 1×10^6 loading cycles is generally used in this kind of studies on AM porous biomaterials that are aimed for application in orthopedic implants. This is because the average patient walking activity is shown to be around 2 million cycles per year (*i.e.*, 52 weeks) [49] and the mean bone fracture healing time is estimated to be 16 weeks for otherwise (skeletally) healthy patients [50]. Once bone has grown into the pores of the biomaterial, the fatigue strength of the bone-implant complex increases by up to 10 folds even for bone tissue with very low mechanical properties (as might be the case for immature bone) [51].

The much-improved level of normalized fatigue resistance in the AM porous biomaterials developed in the current study is likely due to the topology of the internal structure of the biomaterials which is based on sheets rather than beams. Fatigue resistance is related to the crack initiation points, which in the case of AM porous biomaterials are the notches created through the AM process [52,53]. Beam-based designs [31,52–55] are much more prone to development of notches as compared to sheet-based designs such as TPMS. That is partially due to the fact that beam-based designs are often made through sintering of a limited number of powder particles, and the diameter of the struts is usually comparable with the accuracy of the AM technique. In contrast, sheet-based designs such as those based on TPMS have much more smooth and connected geometries that are made from many particles. Therefore, in comparison with beam-based porous structures, continuous sheet-based porous structures are expected to be less sensitive to such imperfections, which could greatly improve their fatigue resistance. Such high levels of fatigue resistance are generally very important for practical application of the developed AM porous biomaterials, because implants could be designed for much higher levels of stress without concerns for patient safety.

3.4.4   Permeability

The permeability of the AM porous biomaterials developed here are in the range of permeability values reported for trabecular bone in the literature (Table 4) [45,56,57]. Similar to trabecular bone [45,57], the permeability of the biomaterials presented here decreases as the apparent density increases (*i.e.*, porosity values decrease). This is in line with the findings of other studies, which have found that the permeability of porous biomaterials and scaffolds is correlated with their porosity, as long as the pores are interconnected [3]. Increased surface area is expected to decrease permeability due to the additional frictional forces [58]. In the porous biomaterials developed here, the surface area generally increases with porosity. Since we found the permeability to increase with porosity, it can be concluded that the effects of increased porosity on permeability are more pronounced as compared to the effects of any increase in frictional forces that might occur due to the increased surface area.

Cell nutrition and oxygenation are dependent on diffusion before the completion of angiogenesis. The reach and speed of mass transport taken place through the diffusion process are dependent on the morphology of the porous biomaterials and their permeability. If high values of pressure and/or concentration gradients are required to transfer nutrients and oxygen to the cells residing in the deepest part of the porous biomaterial, there is a high chance that cell metabolism is disrupted at least in some parts of the biomaterial and tissue regeneration does not properly progress. Proper values of permeability are therefore important for ensuring unhindered mass transport within biomaterials to maximize their bone tissue regeneration performance. Even though the absolute values of permeability measured here are found to be dependent on the type of flow conditions, particularly for

the primitive and gyroid type of minimal surfaces, the permeability values measured for both types of fluid flow remain within the reported values of permeability of trabecular bone. That is partially due to the relatively large span of permeability values reported for trabecular bone [45,56,57]. In any case, more predictability of permeability values may be beneficial during the rational design process of bone-substituting biomaterials. This predictability would help when a good description of the physical properties of the biomaterials is essential for computational modeling of the bone tissue regeneration process. It is important to realize that permeability values are known to be anisotropic also in trabecular bone [59].

3.4.5   Design implications

In general, the availability of libraries which relate the micro-architecture of porous biomaterials to their physical and mechanical properties such as permeability, elastic modulus, and fatigue life could greatly facilitate the design process [60–63]. We presented a class of AM porous biomaterials based on different types of TPMS and with different dimensions in this study. The results of our study show that these materials are generally capable of mimicking the properties of bone tissue. Application of the specific members of this class of porous biomaterials in the design of orthopedic implants may, however, require additional design considerations. For example, the type of TPMS used in different anatomical locations may need to be different or there might be a need for gradients in terms of porosity and/or TPMS type to better mimic the highly complex and spatially varying structure of trabecular bone. One of the limitations of the current study is that the *in vitro* and *in vivo* experiments required for evaluation of the tissue regeneration performance of the developed biomaterials have not been performed.

Although many studies aiming at development of porous biomaterials try to mimic the properties of bone, it is worth noting that the structure of the bone tissue at its equilibrium state may not necessarily be the best structure for enhancing the bone tissue regeneration process, which is a transient state and far from equilibrium. Therefore, it may be necessary to simulate the bone regeneration process while considering mechanobiological aspects [64,65] and theoretical models [66]. This could improve the design of the micro-architecture of bone-substituting biomaterials. Such an approach would allow for direct consideration of the local loading conditions experienced by cells residing on the surface of porous biomaterials [67] and, thus a more mechanistic design methodology.

3.5   Conclusions

Porous metallic biomaterials based on four different types of triply periodic minimal surfaces and with different porosities were rationally designed, additively manufactured, and characterized to evaluate their suitability for orthopedic applications. The combination of topological, mechanical, and physical properties exhibited by these biomaterials suggests

they are promising bone-mimicking biomaterials. In terms of topology, the rationally designed micro-architecture of the porous structures resembled the topological properties of trabecular bone including a mean curvature close to zero. Most porous biomaterials have a highly correlated elastic modulus and (yield) strength. However, the biomaterials developed here showed a unique combination of relatively low elastic moduli in the range of those observed for trabecular bone and high yield stress exceeding those reported for cortical bone. With this combination of relatively low elastic moduli and high yield strength, it is possible to simultaneously avoid stress shielding while providing strong mechanical support for bone regeneration and osseointegration. Furthermore, as opposed to other AM porous biomaterials developed to date, the biomaterials developed in the current study also show extremely high fatigue resistance with some of the porous structures showing an endurance limit as high as 60% of their yield stress. This compares to endurance limits in the range of 20% of the plateau/yield stress reported for previously developed AM porous metallic biomaterials. Finally, the permeability values measured for the developed biomaterials were in the range of permeability values reported for trabecular bone in the literature. Based on above-mentioned results, the additively manufactured porous biomaterials developed here seem to hold significant promise for orthopedic applications. However, *in vivo* studies should be performed to evaluate their actual bone regeneration performance.

References

[1] M. Dias, P. Fernandes, J. Guedes, S. Hollister, Permeability analysis of scaffolds for bone tissue engineering, J. Biomech. 45 (6) (2012) 938–944.

[2] S.J. Hollister, Porous scaffold design for tissue engineering, Nat. Mater. 4 (7) (2005) 518–524.

[3] T.S. Karande, J.L. Ong, C.M. Agrawal, Diffusion in Musculoskeletal tissue engineering scaffolds: design issues related to porosity, permeability, architecture, and nutrient mixing, Ann. Biomed. Eng. 32 (12) (2004) 1728–1743.

[4] X. Wang, S. Xu, S. Zhou, W. Xu, M. Leary, P. Choong, M. Qian, M. Brandt, Y.M.Xie, Topological design and additive manufacturing of porous metals for bone scaffolds and orthopaedic implants: a review, Biomaterials 83 (2016) 127–141.

[5] S. Li, Q. Xu, Z. Wang, W. Hou, Y. Hao, R. Yang, L. Murr, Influence of cell shape on mechanical properties of Ti–6Al–4V meshes fabricated by electron beam melting method, Acta Biomater. 10 (10) (2014) 4537–4547.

[6] S. Amin Yavari, L. Loozen, F.L. Paganelli, S. Bakhshandeh, K. Lietaert, J.A. Groot,A.C. Fluit, C.E. Boel, J. Alblas, H.C. Vogely, H. Weinans, A. A. Zadpoor, Antibacterial behavior of additively manufactured porous titanium with nanotubular surfaces releasing silver ions, ACS Appl. Mater. Interfaces 8 (27) (2016) 17080–17089.

[7] J. van der Stok, M. Koolen, M. de Maat, S.A. Yavari, J. Alblas, P. Patka, J. Verhaar, E. van Lieshout, A.A. Zadpoor, H. Weinans, H. Jahr, Full regeneration of segmental bone defects using porous titanium implants loaded with BMP-2 containing fibrin gels, Eur. Cells Mater. 2015 (29) (2015) 141–154.

[8] A.A. Zadpoor, Bone tissue regeneration: the role of scaffold geometry, Biomater. Sci. 3 (2) (2015) 231–245.

[9] C.M. Bidan, K.P. Kommareddy, M. Rumpler, P. Kollmannsberger, Y.J. Bréchet, P. Fratzl, J.W. Dunlop, How linear tension converts to curvature: geometric control of bone tissue growth, PLoS One 7 (5) (2012) e36336.

[10] C.M. Bidan, K.P. Kommareddy, M. Rumpler, P. Kollmannsberger, P. Fratzl, J.W. Dunlop, Geometry as a factor for tissue growth: towards shape optimization of tissue engineering scaffolds, Adv. Healthcare Mater. 2 (1) (2013) 186–194.

[11] M. Rumpler, A. Woesz, J.W. Dunlop, J.T. van Dongen, P. Fratzl, The effect of geometry on three-dimensional tissue growth, J. R. Soc. Interface 5 (27) (2008) 1173–1180.

[12] H. Karcher, K. Polthier, Construction of triply periodic minimal surfaces, Philos.Trans. R. Soc. London A 354 (1715) (1996) 2077–2104.

[13] C.M. Bidan, F.M. Wang, J.W. Dunlop, A three-dimensional model for tissue deposition on complex surfaces, Comput. Methods Biomech. Biomed. Eng. 16(10) (2013) 1056–1070.

[14] H. Jinnai, Y. Nishikawa, M. Ito, S.D. Smith, D.A. Agard, R.J. Spontak, Topological similarity of sponge-like bicontinuous morphologies differing in length scale, Adv. Mater. 14 (22) (2002) 1615–1618.

[15] H. Jinnai, H. Watashiba, T. Kajihara, Y. Nishikawa, M. Takahashi, M. Ito, Surface curvatures of trabecular bone microarchitecture, Bone 30 (1) (2002) 191–194.

[16] S.T. Hyde, G.E. Schröder-Turk, Geometry of interfaces: topological complexity in biology and materials, Interface Focus 2 (5) (2012) 529–538.

[17] S.C. Kapfer, S.T. Hyde, K. Mecke, C.H. Arns, G.E. Schröder-Turk, Minimal surface scaffold designs for tissue engineering, Biomaterials 32 (29) (2011) 6875–6882.

[18] J.W. Galusha, L.R. Richey, J.S. Gardner, J.N. Cha, M.H. Bartl, Discovery of a diamond-based photonic crystal structure in beetle scales, Phys. Rev. E 77 (5)(2008) 050904.

[19] J.W. Galusha, L.R. Richey, M.R. Jorgensen, J.S. Gardner, M.H. Bartl, Study of natural photonic crystals in beetle scales and their conversion into inorganic structures via a sol–gel bio-templating route, J. Mater. Chem. 20 (7) (2010) 1277–1284.

[20] S. Hyde, S. Andersson, K. Larsson, Z. Blum, T. Landh, S. Lidin, B. Ninham, The Language of Shape: The Role of Curvature in Condensed Matter: Physics, Chemistry and Biology, Elsevier, 1997.

[21] H.-U. Nissen, Crystal orientation and plate structure in echinoid skeletal units, Science 166 (3909) (1969) 1150–1152.

[22] G. Schröder-Turk, S. Wickham, H. Averdunk, F. Brink, J.F. Gerald, L. Poladian, M. Large, S. Hyde, The chiral structure of porous chitin within the wing-scales of Callophrys rubi, J. Struct. Biol. 174 (2) (2011) 290–295.

[23] V. ABAQUS, 6.13, Dassault Systemes, 2013.

[24] J. Schindelin, I. Arganda-Carreras, E. Frise, V. Kaynig, M. Longair, T. Pietzsch, S.Preibisch, C. Rueden, S. Saalfeld, B.Schmid, Fiji: an open-source platform for biological-image analysis, Nat. Methods 9 (7) (2012) 676–682.

[25] M. Doube, M.M. Kłosowski, I. Arganda-Carreras, F.P. Cordelières, R.P. Dougherty, J.S. Jackson, B. Schmid, J.R. Hutchinson, S.J. Shefelbine, BoneJ: free and extensible bone image analysis in ImageJ, Bone 47 (6) (2010) 1076–1079.

[26] W. Sobieski, A. Trykozko, Darcy's and Forchheimer's laws in practice–Part 1: The experiment, Tech. Sci. 17 (4) (2014) 321–335.

[27] International Organization for Standardization (ISO), ISO13314: Mechanical Testing of Metals – Ductility Testing – Compression Test for Porous and Cellular Metals, First edition 2011-12-15, 2011.

[28] International Organization for Standardization (ISO), ISO12108: MetallicMaterials – Fatigue Testing – Fatigue Crack Growth Method, Second edition2012-08-15, 2012.

[29] S. Ahmadi, G. Campoli, S.A. Yavari, B. Sajadi, R. Wauthlé, J. Schrooten, H. Weinans, A. A. Zadpoor, Mechanical behavior of regular open-cell porous biomaterials made of diamond lattice unit cells, J. Mech. Behav. Biomed.Mater. 34 (2014) 106–115.

[30] S.M. Ahmadi, S.A. Yavari, R. Wauthle, B. Pouran, J. Schrooten, H. Weinans, A.A.Zadpoor, Additively manufactured open-cell porous biomaterials made from six different space-filling unit cells: the mechanical and morphological properties, Materials 8 (4) (2015) 1871–1896.

[31] R. Wauthle, B. Vrancken, B. Beynaerts, K. Jorissen, J. Schrooten, J.-P. Kruth, J. Van Humbeeck, Effects of build orientation and heat treatment on the microstructure and mechanical properties of selective laser melted Ti6Al4V lattice structures, Addit. Manuf. 5 (2015) 77–84.

[32] V. Karageorgiou, D. Kaplan, Porosity of 3D biomaterial scaffolds and osteogenesis, Biomaterials 26 (27) (2005) 5474–5491.

[33] S. Amin Yavari, R. Wauthlé, A.J. Böttger, J. Schrooten, H. Weinans, A.A. Zadpoor, Crystal structure and nanotopographical features on the surface of heat-treated and anodized porous titanium biomaterials produced using selective laser melting, Appl.Surf. Sci. 290 (2014) 287–294.

[34] A.B. Faia-Torres, S. Guimond-Lischer, M. Rottmar, M. Charnley, T. Goren, K. Maniura-Weber, N.D. Spencer, R.L. Reis, M. Textor, N.M. Neves, Differential regulation of osteogenic differentiation of stem cells on surface roughness gradients, Biomaterials 35 (33) (2014) 9023–9032.

[35] R.A. Gittens, T. McLachlan, R. Olivares-Navarrete, Y. Cai, S. Berner, R. Tannenbaum, Z. Schwartz, K.H. Sandhage, B.D. Boyan, The effects of combined micron-/submicron-scale surface roughness and nanoscale features on cell proliferation and differentiation, Biomaterials 32 (13) (2011)3395–3403.

[36] Y. Khan, M.J. Yaszemski, A.G. Mikos, C.T. Laurencin, Tissue engineering of bone: material and matrix considerations, J. Bone Joint Surg. 90 (Supplement 1) (2008) 36–42.

[37] X. Li, J. Lan, M. Ai, Y. Guo, Q. Cai, X. Yang, Biomineralization on polymer-coated multi-walled carbon nanotubes with different surface functional groups, Colloids Surf. B 123 (2014) 753–761.

[38] S. Zhao, J. Zhang, M. Zhu, Y. Zhang, Z. Liu, Y. Ma, Y. Zhu, C. Zhang, Effects of functional groups on the structure, physicochemical and biological properties of mesoporous bioactive glass scaffolds, J. Mater. Chem. B 3 (8) (2015) 1612–1623.

[39] E. Gamsjäger, C. Bidan, F. Fischer, P. Fratzl, J. Dunlop, Modeling the role of surface stress on the kinetics of tissue growth in confined geometries, Acta Biomater. 9 (3) (2013) 5531–5543.

[40] E.F. Morgan, H.H. Bayraktar, T.M. Keaveny, Trabecular bone modulus–density relationships depend on anatomic site, J. Biomech. 36 (7) (2003)897–904.

[41] K. Choi, J. Kuhn, M. Ciarelli, S. Goldstein, The elastic moduli of human subchondral, trabecular, and cortical bone tissue and the size-dependency of cortical bone modulus, J. Biomech. 23 (11) (1990).

[42] D.T. Reilly, A.H. Burstein, The elastic and ultimate properties of compact bone tissue, J. Biomech. 8 (6) (1975). 393IN9397–396IN11405.

[43] J.W. Vahey, J.L. Lewis, R. Vanderby, Elastic moduli, yield stress, and ultimate stress of cancellous bone in the canine proximal femur, J. Biomech. 20 (1) (1987) 29–33.

[44] L.J. Gibson, The mechanical behavior of cancellous bone, J. Biomech. 18 (5) (1985) 317–328.

[45] D.A. Shimko, V.F. Shimko, E.A. Sander, K.F. Dickson, E.A. Nauman, Effect of porosity on the fluid flow characteristics and mechanical properties of tantalum scaffolds, J. Biomed. Mater. Res. B Appl. Biomater. 73 (2) (2005)315–324.

[46] M. Wettergreen, The Effect of Material Organization on the Structural Properties of Porous Architectures, Rice University, Department of Bioengineering, 2008.

[47] S. Amin Yavari, S. Ahmadi, R. Wauthle, B. Pouran, J. Schrooten, H. Weinans, A.Zadpoor, Relationship between unit cell type and porosity and the fatigue behavior of selective laser melted meta-biomaterials, J. Mech. Behav. Biomed.Mater. 43 (2015) 91–100.

[48] S. Amin Yavari, R. Wauthlé, J. van der Stok, A. Riemslag, M. Janssen, M. Mulier,J.-P. Kruth, J. Schrooten, H. Weinans, A.A. Zadpoor, Fatigue behavior of porous biomaterials manufactured using selective laser melting, Mater. Sci. Eng. C 33(8) (2013) 4849–4858.

[49] M. Silva, E.F. Shepherd, W.O. Jackson, F.J. Dorey, T.P. Schmalzried, Average patient walking activity approaches 2 million cycles per year: pedometers under-record walking activity, J. Arthroplasty 17 (6) (2002) 693–697.

[50] V.S. Nikolaou, N. Efstathopoulos, G. Kontakis, N.K. Kanakaris, P.V. Giannoudis, The influence of osteoporosis in femoral fracture healing time, Injury 40 (6) (2009) 663–668.

[51] R. Hedayati, S. Janbaz, M. Sadighi, M. Mohammadi-Aghdam, A. A. Zadpoor, How does tissue regeneration influence the mechanical behavior of additively manufactured porous biomaterials?, J Mech. Behav. Biomed. Mater. 65 (2017)831–841.

[52] S. Amin Yavari, S. Ahmadi, J. van der Stok, R. Wauthlé, A. Riemslag, M. Janssen, J. Schrooten, H. Weinans, A.A. Zadpoor, Effects of bio-functionalizing surface treatments on the mechanical behavior of open porous titanium biomaterials, J. Mech. Behav. Biomed. Mater. 36 (2014) 109–119.

[53] J. De Krijger, C. Rans, B. Van Hooreweder, K. Lietaert, B. Pouran, A.A. Zadpoor, Effects of applied stress ratio on the   fatigue behavior of additively manufactured porous biomaterials under compressive loading, J. Mech.Behav. Biomed. Mater. (2016). in press.

[54] R. Wauthle, S.M. Ahmadi, S.A. Yavari, M. Mulier, A.A. Zadpoor, H. Weinans, J. Van Humbeeck, J.-P. Kruth, J. Schrooten, Revival of pure titanium for dynamically loaded porous implants using additive manufacturing, Mater.Sci. Eng. C 54 (2015) 94–100.

[55] R. Wauthle, J. Van der Stok, S.A. Yavari, J. Van Humbeeck, J.-P. Kruth, A.A. Zadpoor, H. Weinans,

M. Mulier, J. Schrooten, Additively manufactured porous tantalum implants, Acta Biomater. 14 (2015) 217–225.

[56] M.J. Grimm, J.L. Williams, Measurements of permeability in human calcaneal trabecular bone, J. Biomech. 30 (7) (1997) 743–745.

[57] E.A. Nauman, K. Fong, T. Keaveny, Dependence of intertrabecular permeability on flow direction and anatomic site, Ann. Biomed. Eng. 27 (4) (1999) 517–524.

[58] F.J. O'Brien, B.A. Harley, M.A. Waller, I.V. Yannas, L.J. Gibson, P.J. Prendergast, The effect of pore size on permeability and cell attachment in collagen scaffolds for tissue engineering, Technol. Health Care 15 (1) (2007) 3–17.

[59] G. Baroud, R. Falk, M. Crookshank, S. Sponagel, T. Steffen, Experimental and theoretical investigation of directional permeability of human vertebral cancellous bone for cement infiltration, J. Biomech. 37 (2) (2004) 189–196.

[60] B. Bucklen, W. Wettergreen, E. Yuksel, M. Liebschner, Bone-derived CAD library for assembly of scaffolds in computer-aided tissue engineering, VirtualPhys. Prototyping 3 (1) (2008) 13–23.

[61] A.M. Tarawneh, M. Wettergreen, M.A. Liebschner, Computer-aided tissue engineering: benefiting from the control over scaffold micro-architecture, Comp. Aided Tissue Eng. (2012) 1–25.

[62] M. Wettergreen, B. Bucklen, M. Liebschner, W. Sun, CAD Assembly Process for Bone Replacement Scaffolds in Computer-Aided Tissue Engineering, Virtual Prototyping & Bio Manufacturing in Medical Applications, Springer, 2008, pp.87–111.

[63] M. Wettergreen, B. Bucklen, B. Starly, E. Yuksel, W. Sun, M. Liebschner, Creation of a unit block library of architectures for use in assembled scaffold engineering, Comput. Aided Des. 37 (11) (2005) 1141–1149.

[64] M. Liebschner, B. Bucklen, M. Wettergreen, Mechanical aspects of tissue engineering, in: Seminars in Plastic Surgery, Copyright© 2005 by Thieme Medical Publishers, Inc., 333 Seventh Avenue, New York, NY 10001, USA, 2005, pp. 217–228.

[65] M. Liebschner, M. Wettergreen, Optimization of bone scaffold engineering for load bearing applications, Top. Tissue Eng. (2003) 1–39.

[66] A.A. Zadpoor, Open forward and inverse problems in theoretical modeling of bone tissue adaptation, J. Mech. Behav. Biomed. Mater. 27 (2013) 249–261.

[67] B. Bucklen, Investigation of Surface Mechanical Environment as an Optimization Criterion for Improved Tissue Engineering Scaffolds, Rice University, Department of Bioengineering, 2008.

[68] R. Goulet, S. Goldstein, M. Ciarelli, J. Kuhn, M. Brown, L. Feldkamp, The relationship between the structural and orthogonal compressive properties of trabecular bone, J. Biomech. 27 (4) (1994) 375–389.

[69] D. Ulrich, B. Van Rietbergen, A. Laib, P. Ruegsegger, The ability of three-dimensional structural indices to reflect mechanical aspects of trabecular bone, Bone 25 (1) (1999) 55–60.

[70] G. Bevill, T.M. Keaveny, Trabecular bone strength predictions using finite element analysis of micro-scale images at limited spatial resolution, Bone 44(4) (2009) 579–584.

[71] P. Rüegsegger, B. Koller, R. Müller, A microtomographic system for the nondestructive evaluation of bone architecture, Calcif. Tissue Int. 58 (1) (1996)24–29.

[72] X.-N. Gu, Y.-F. Zheng, A review on magnesium alloys as biodegradable materials, Front. Mater. Sci. Chin. 4 (2) (2010) 111–115.

[73] D.L. Kopperdahl, T.M. Keaveny, Yield strain behavior of trabecular bone, J.Biomech. 31 (7) (1998) 601–608.

[74] F. Linde, I. Hvid, B. Pongsoipetch, Energy absorptive properties of human trabecular bone specimens during axial compression, J. Orthop. Res. 7 (3) (1989) 432–439.

[75] A. Rohlmann, H. Zilch, G. Bergmann, R. Kolbel, Material properties of femoral cancellous bone in axial loading, Arch. Orthop. Trauma. Surg. 97 (2) (1980) 95–102.

[76] J.D. Currey, Tensile yield in compact bone is determined by strain, post-yield behavior by mineral content, J. Biomech. 37 (4) (2004) 549–556.

[77] J.C. Lotz, T.N. Gerhart, W.C. Hayes, Mechanical properties of trabecular bone from the proximal femur: a quantitative CT study, J. Comput. Assist. Tomogr.14 (1) (1990) 107–114.

[78] A.J. Beaudoin, W.M. Mihalko, W.R. Krause, Finite element modeling of polymethylmethacrylate flow through cancellous bone, J. Biomech. 24 (2)(1991) 127131–129136.

4

Deployable non-assembly mechanisms

Porous biomaterials are often used to treat large bony defects or fractured vertebrae. Most of such biomaterials are made of metals and their alloys and have a predefined, fixed shape. Due to their predefined fixed shape, however, they are not suitable for implantation through minimally invasive surgical procedures. To overcome this problem, we designed three different deployable non-assembly mechanisms, which were manufactured using selective laser melting. Upon the application of an external force, the structures expand radially into their deployed load-bearing configuration. Using non-assembly manufacturing, revolute joints, wavelike elements, rigid rods and restrictions could be integrated into the design. Mechanical tests were performed to determine the forces required to deploy the designed structures and to determine their failure load. The elongated geometry of our designs makes them ideal for implantation using minimally invasive surgical procedures.

4.1 Introduction

Bone tissue regeneration approaches often require the use of porous biomaterials for the treatment of large bony defects [1]. These bony defects are too large to be repaired by the cells inside our body and surgical intervention is required [2]. Although bone tissue substitutes such as autogenous and allogeneic tissue grafts are available, their limited supply [3, 4], donor site morbidity [3], and the risk of viral and bacterial disease transmission [3, 5] motivate the development of engineered and innovative replacements [3, 4].

Various types of bone substitutes [2, 6-8] have been fabricated using additive manufacturing (AM) techniques. Selective laser melting (SLM) is the most commonly used AM technique for the fabrication of porous biomaterials made of metals and their alloys, including titanium [9-12], zinc [13-15], magnesium [16-18], and iron [19, 20].

Although many types of porous biomaterials and (patient-specific) orthopedic implants have been manufactured using SLM [21], most of them have a pre-determined, fixed shape. Such voluminous, fixed-shape implants can hardly be implanted using minimally invasive surgery techniques. Minimally invasive surgeries, such as arthroscopy and laparoscopy [22, 23] limit the damage to the body, require shorter recovery times [24], and lower the risk of post-operative complications [25, 26]. This is due to the small incisions required to insert the medical devices into the body [23].

A potential solution for the high invasiveness of such orthopedic surgeries is the use of deployable implants, which are initially compact and can, thus, be implanted using minimally invasive surgical techniques. Upon the application of an external force, the structures can transform into their deployed configuration inside the defect. We have recently applied AM for the fabrication of deployable meta-implants [27, 28]. While our previous designs demonstrate both the concept of deployability in meta-implants and the utility of AM, they generally require an assembly step. Such a step is labor-intensive, time-consuming, and makes it very challenging to upscale the production of such implants. Non-assembly AM could pave the way for the large-scale production of deployable meta-implants.

Recently, AM has been used for the fabrication of a limited number of non-assembly mechanisms [29-31], which are manufactured using a single-step fabrication process and are often made of rigid bodies and joints. Due to the design choices and the orientation of such mechanisms on the build platform, there is no need for an assembly step after fabrication [32, 33]. The other advantages of this approach include unique functionalities, improved kinematic performance, and the integration of advanced features in the design process [31]. Two examples of non-assembly mechanisms manufactured using SLM are the CubeSat [34] and metallic clay [35]. The CubeSat is a cube ($10 \times 10 \times 10$ cm^3) developed for space research. Although various CubeSat designs are available, Boschetto *et al.* (2019) used SLM to manufacture an already-assembled CubeSat consisting of two half cubes connected by a hinge [34]. By integrating locating and locking features into the design, both halves are guided

as the cube closes, thereby ensuring that they eventually attach to each other [34]. A more relevant concept for orthopedic applications is that of metallic clay, which we have recently proposed for shape-matching biomaterials [35]. Metallic clay is composed of a network of joints, spring-like elements, rigid rods, and locking mechanisms that work together to enable the shape-morphing and shape-locking behaviors of the mechanisms (analogous to the states of clay before and after firing, respectively) [35].

In this study, we propose a number of novel designs that make it possible to use SLM for non-assembly AM of deployable implants. We chose the treatment of fractured vertebrae and large bony defects in the pelvis as the model surgical challenges for which the deployable implants were designed. We designed the mechanisms such that they had a large aspect ratio in their retracted state. Upon the application of an external force, the elongated structures expand radially into their deployed configuration. We integrated different features to lock the deployed configuration of the specimens. Wavelike elements, revolute joints, and restrictions enable the reconfiguration and locking of the mechanisms. Additionally, we used specific design approaches and selected the build orientation in such a way that the minimum number of support structures were required during the manufacturing process. We then manufactured different designs using SLM and mechanically tested the resulting implants to determine their deployment force and their failure loads.

4.2   Materials and Methods

4.2.1   Design

4.2.1.1   Components of the designs

Three different deployable geometries were designed, namely a bicapped trigonal antiprism, a bicapped square antiprism, and a bicapped cube (Figure 1a, b). The bicapped antiprisms were constructed with connecting rods a and b along all the slanting edges of the geometry. No rods were placed along the edges of the base faces. At all vertices, clusters of revolute joints were positioned with a separate joint for every connecting rod. The axes of rotation of all joints were in parallel to the basal plane and perpendicular to the connecting rods.

Contrary to the bicapped antiprisms, the side faces of the bicapped cube did not consist of alternating isosceles triangles but of rectangles (Figure 1a, b). In this geometry, the rods were positioned along the diagonals m and n with a revolute joint at the intersection, creating two mirrored isosceles triangles. No rods were placed at the vertical and horizontal edges.

The geometries can be deployed by compressing them at the proximal and distal vertices A and B, respectively (Figure 1c). This action decreases the angle α of the lateral edge with the base diagonal of the bicapped structures and simultaneously increases the vertex angle γ of the isosceles triangles on the side faces. Consequently, the circumradius R of the triangle or square base face increases from its smallest value in the retracted state to its maximum value
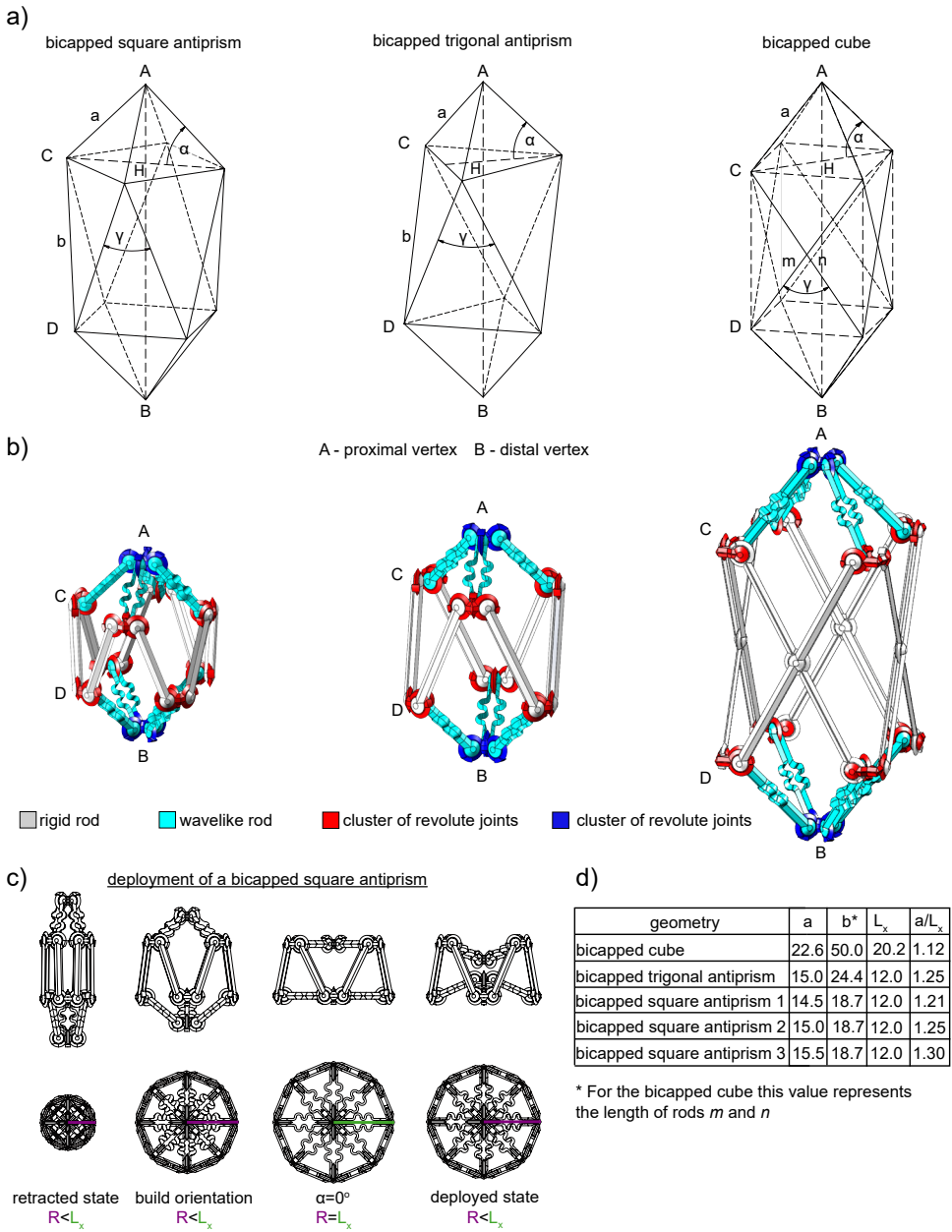
a)

bicapped square antiprism   bicapped trigonal antiprism   bicapped cube

b)

A - proximal vertex   B - distal vertex

☐ rigid rod   ☐ wavelike rod   ■ cluster of revolute joints   ■ cluster of revolute joints

c) deployment of a bicapped square antiprism

retracted state   build orientation $\alpha=0°$ deployed state
$R<L_x$ $R<L_x$ $R=L_x$ $R<L_x$

d)

geometry	a	b*	L_x	a/L_x
bicapped cube	22.6	50.0	20.2	1.12
bicapped trigonal antiprism	15.0	24.4	12.0	1.25
bicapped square antiprism 1	14.5	18.7	12.0	1.21
bicapped square antiprism 2	15.0	18.7	12.0	1.25
bicapped square antiprism 3	15.5	18.7	12.0	1.30

* For the bicapped cube this value represents the length of rods *m* and *n*

Figure 1. a) The line drawings of the bicapped square antiprism, the bicapped trigonal antiprism, and the bicapped cube. b) The CAD models of the three geometries plotted in their configuration during the SLM process. Red: a cluster of revolute joints, Blue: the proximal and distal clusters of revolute joints, turquoise: wavelike rod, grey: rigid rod. c) The different states of a bicapped square antiprism during its deployment process with an indication of the circumradius R and the designed maximum circumradius L_x. d) The values of the length of the wavelike rods (*a*) [mm], the length of the rigid rods (*b*, *m*, and *n*) [mm], and the designed maximum circumradius L_x.

when $\alpha = 0°$ (Figures 1c, 2). By moving A and B further inwards, the circumradius reduces until A and B meet in the center and the deployed state of the geometry is reached. Pulling at A and B reverses the deployment process and leads to the retraction of the geometry.
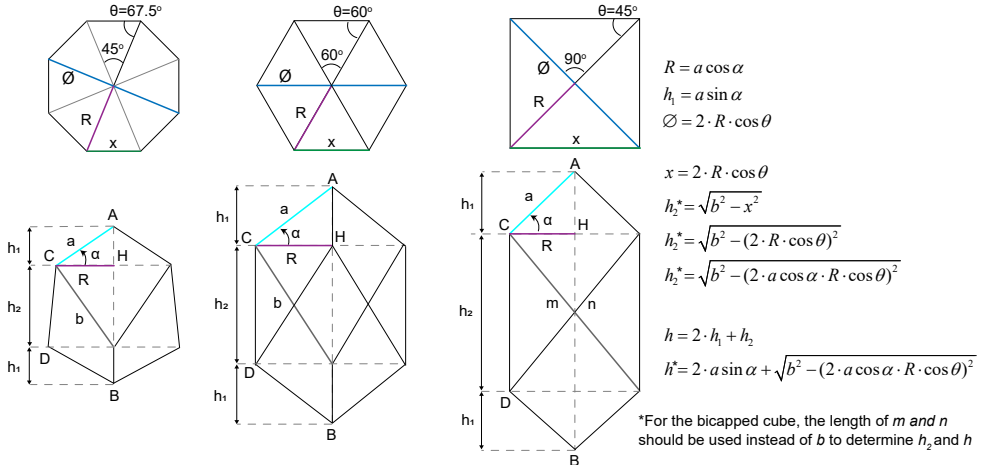

Figure 2. Equations to determine the theoretical diameter and height of the different geometries from their maximum circumradius ($\angle ABH = 0°$) to fully retracted. The top and side views of the bicapped square antiprism, the bicapped trigonal antiprism, and the bicapped cube.

4.2.1.2   Design variations

We varied the dimensions of the designed structures to study the effects of those dimensions on the kinematics and kinetics of the deployable meta-implants. The length of the connecting rod a determined the circumradius of the structure while the height is determined by the length of the connecting rod b or m and n for the bicapped antiprism and bicapped cube, respectively. Figure 3d shows six bicapped square antiprisms, including three different lengths for the connecting rod a and two different lengths for the connecting rod b (Figure 3a).

4.2.1.3   Evaluated design

In order to create a retracted configuration, a maximum circumradius, and a deployed state, restrictions were placed on the bearings of the revolute joints to limit the movement of the rods. The rods b and m and n of the antiprisms and the bicapped cube, respectively, were restricted in the deploying direction to a maximum circumradius of $L_{x'}$. In addition, rods a were restricted at the retracted and deployed positions.

When comprising only rigid rods, the geometries can freely move between the retracted and deployed positions provided that the length of the connecting rods a is smaller or equal to the maximum restricted circumradius $L_{x'}$. However, when they are longer than $L_{x'}$, the geometry cannot move further towards the deployed position. Substituting these rigid rods

connected to the proximal and distal vertices *A* and *B* with wavelike rods allows the rods to deform in the lateral direction. This deformation reduces the length of the wavelike rod to equal the circumradius and enables vertices *A* and *B* to be pushed through this position and reach the deployed, locked state.

Five configurations were prepared with a varying oversize of the wavelike rods (Figure 1d). The oversize was defined as $a\,/\,L_x$ where *a* is the length of the wavelike rods and L_x is the designed axis-to-axis distance between the paired revolute joint bearings at the maximum restricted circumradius, measured horizontally.

The changes in the specimen dimensions as a consequence of deployment were determined through the measurements of the height and circumdiameter of the specimens in their retracted and deployed configurations. Since the height reduced and the circumdiameter increased upon deployment, the reduction in the height and increase in the circumdiameter were determined as:

$$reduction\ in\ height = \left(1 - \frac{deployed\ height}{retracted\ height}\right) \times 100$$

and

$$increase\ in\ circumdiameter = \frac{deployed\ circumdiameter}{retracted\ circumdiameter} \times 100$$

4.2.2   Manufacturing

The specimens were manufactured in-house using an SLM125 (Realizer GmbH, Germany) machine. As feedstock, plasma-atomized Ti6Al4V-ELI powder with a particle size between 10 and 45 µm (AP&C, Canada) was used. The build chamber was flushed with argon gas to ensure an oxygen level below 0.2% during printing. The substrate plate, on which the specimens were built, was kept at 100 °C. The process parameters used for the contour and hatch are specified in Table 1.

Process parameters	Contour	Hatch
Exposure time (µs)	20	5
Point distance (µm)	10	10
Laser current (mA)	1100	1100
Hatch distance (µm)	-	150

Table 1. The contour and hatch parameters used in the laser scanning process.

After printing (Figure 3b, c), the substrate supports were removed from all downward-facing, exterior surfaces of the specimens. The revolute joints of the specimens were designed in such a manner that support structures were not required for maintaining their clearance space. This is in contrast with traditional joints (*e.g.*, traditional ball-and-socket joints) where

support structures are required to ensure the different parts of the joints remain separate from each other. In order to remove the loose powder particles remaining in the joint clearance, the specimens were ultrasonically cleaned for 15 minutes.
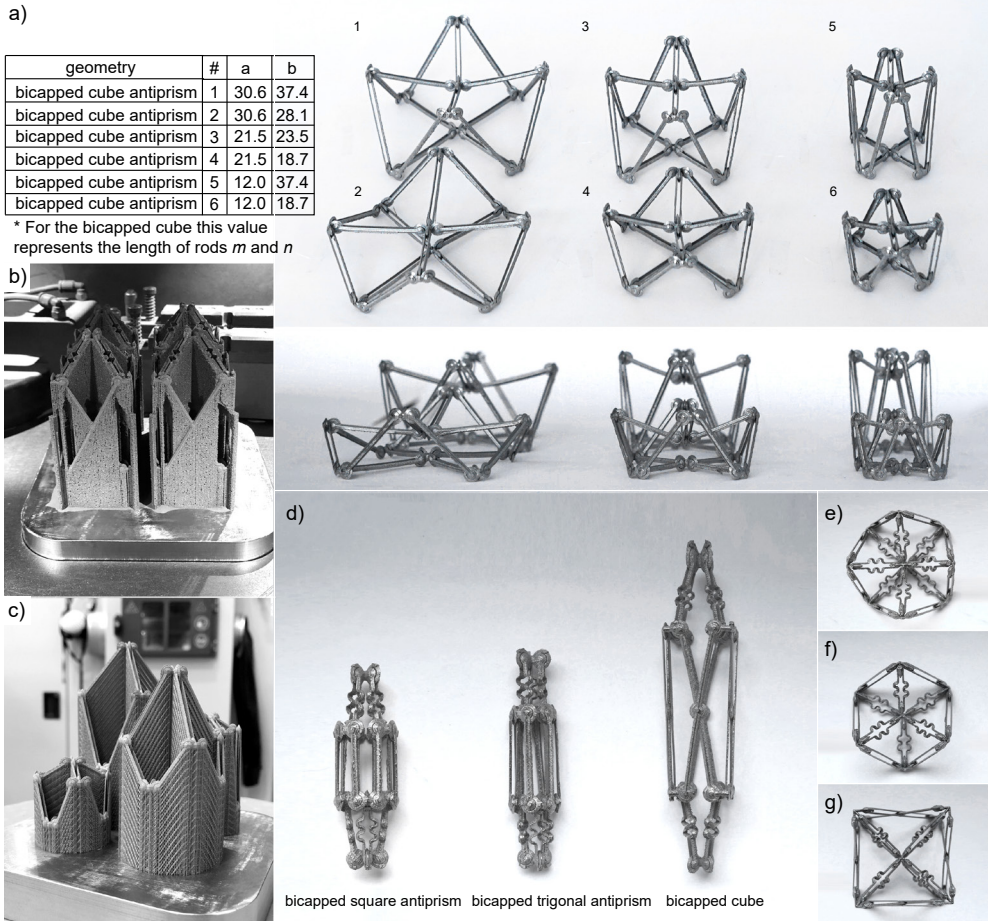
a)

geometry	#	a	b
bicapped cube antiprism	1	30.6	37.4
bicapped cube antiprism	2	30.6	28.1
bicapped cube antiprism	3	21.5	23.5
bicapped cube antiprism	4	21.5	18.7
bicapped cube antiprism	5	12.0	37.4
bicapped cube antiprism	6	12.0	18.7

* For the bicapped cube this value represents the length of rods *m* and *n*

b)

c)

d)

bicapped square antiprism   bicapped trigonal antiprism   bicapped cube

e)

f)

g)

Figure 3. a) The table listing the lengths of the connecting rods *a* and *b* with numbers corresponding to the bicapped square antiprisms designs presented. b) As-built bicapped cube specimens with wavelike and rigid connecting rods. c) As-built bicapped square antiprism specimens composed of solely rigid rods. d) SLM specimens in their retracted state: a bicapped square antiprism, a bicapped trigonal antiprism, and a bicapped cube. e) The top view of the deployed configuration of a bicapped square antiprism specimen. f) The top view of the deployed state of a bicapped trigonal antiprism specimen. g) The top view of the deployed configuration of a bicapped cube specimen.

4.2.3 Mechanical tests

4.2.3.1 Deployment forces

A Lloyd LR5K mechanical testing machine was used to determine the forces required to deploy the specimens. Compression tests were performed using a crosshead speed of 20

mm/min and a 100 N load cell. Before a specimen was compressed in order to deploy the specimen, it was attached to the machine using wire steel at its proximal and distal vertices (Figures 4a, 5a).

Due to the different dimensions of the specimens, the maximum displacement of the crosshead varied per design. The tests were aborted after 42 mm, 44 mm, and 70 mm for the bicapped square antiprisms, bicapped trigonal antiprism, and the bicapped cube specimens, respectively. The deployment force measurements were repeated three times per specimen.

The forces taken from the force-displacement curves were $F_{firstpeak}$ (the force required to open the specimen), F_{max} (the force required to deform the wavelike elements to enable the locking process), and F_{lock} (the force required to bring the specimen into its load-bearing deployed state ($\angle ABH < 0°$)).

4.2.3.2 Failure load

The failure loads of the specimens were measured in their deployed configuration to determine the maximum load that the specimens could support. The specimens were placed onto the bearing plate and a 5 kN load cell was connected to the crosshead to compress the specimens with a crosshead speed of 5 mm/min.

4.3   Results

4.3.1   Change in dimensions

All specimens were measured in their retracted and deployed configurations (Table 2). The smallest increase in the circumdiameter (185 ± 40 %) and smallest reduction in the height (53 ± 2%) were found for the bicapped cube specimens. The circumdiameter of the bicapped trigonal antiprism specimens increased the most (322 ± 7 %) and the largest reduction in the height (61 ± 1%) was found for the bicapped square antiprism 3 specimens.

4.3.2   Mechanical tests

4.3.2.1   Deployment forces

The different lengths of the rigid and wavelike rods and the geometry of the specimens led not only to different mechanical behaviors but also to different ways of deployment (Figures 3b, 4b). The bicapped cube specimens all started their deployment process by opening the proximal vertex and distal vertex simultaneously, which was followed by the inward movement and locking of the distal vertex. The inward movement and locking of the proximal vertex were always the last step in the deployment process (Figure 4a). In addition to this deployment sequence, the bicapped trigonal antiprism and bicapped square antiprism specimens also showed a sequence in which the inward movement and locking of the distal vertex was the last step in the deployment process. These different sequences of deployment

	Retracted		Deployed		Change in dimensions	
Geometry	Height [mm]	Circumdiameter [mm]	Height [mm]	Circumdiameter [mm]	Height [%]	Circumdiameter [%]
bicapped cube	97.6 ± 2.7	31.4 ± 5.7	45.8 ± 0.9	56.6 ± 1.1	53 ± 2	185 ± 40
bicapped trigonal antiprism	60.1 ± 0.1	12.8 ± 0.3	25.3 ± 0.1	41.1 ± 0.1	58 ± 0	322 ± 7
bicapped square antiprism 1	53.1 ± 0.2	16.0 ± 0.3	22.3 ± 0.7	39.2 ± 0.2	58 ± 1	245 ± 4
bicapped square antiprism 2	54.0 ± 0.3	16.0 ± 0.2	21.9 ± 0.1	40.4 ± 0.9	59 ± 0	253 ± 7
bicapped square antiprism 3	55.1 ± 0.2	16.7 ± 0.6	21.4 ± 0.3	40.7 ± 0.2	61 ± 1	244 ± 9

Table 2. The dimensions of the specimens in their retracted and deployed states.

showed different force-displacement curves (Figures 4-5).

In the first stage of the deployment process, the bicapped square antiprism 3 specimens required the highest force ($F_{firstpeak}$ = 6.7 ± 1.1 N) to open either the proximal or distal vertex of the specimens. The bicapped cube specimens required the least force to open ($F_{firstpeak}$ = 1.5 ± 1.4 N) (Figure 4b, c).

The force-displacement graphs of the sequence in which the locking of the proximal vertex is the last step in the deployment process (Figure 4b) showed that the wavelike elements of bicapped square antiprism 3 require the most force to be compressed (F_{max} = 10.3 ± 1.6 N).

This geometry is followed by the bicapped cube specimens (F_{max} = 6.3 ± 2.4 N), bicapped square antiprism 2 (F_{max} = 2.6 ± 0.3 N), bicapped square antiprism 1 (F_{max} = 2.2 ± 0.6 N), and finally the bicapped trigonal antiprism (F_{max} = 1.3 ± 0.2 N) specimens (Figure 4b, c). The bicapped square antiprism 3, bicapped square antiprism 2, and the bicapped cube specimens showed a negative force of F_{lock} =-1.6 ± 1.2 N, F_{lock}= 0 ± 0.3N, and F_{lock} =-1 ± 0.8 N respectively, during the locking of the proximal vertex.

Similar to the deployment sequence in which the locking of the proximal vertex was the last step of the deployment process, the bicapped square antiprism 3 specimens required the highest force to completely open the proximal and distal vertices ($F_{firstpeak}$ = 4.6 ± 0.6 N) and to deform the wavelike rods (F_{max} = 8.7 ± 0.1 N) when the inward movement of the distal vertex was the last step of the deployment process (Figure 5b, c). Contrary to the forces in the final stage of the deployment process of the bicapped square antiprism 3 specimens, no negative forces were observed during the locking of the distal vertex (F_{lock}) of the bicapped trigonal antiprism, bicapped square antiprism 1, and bicapped square antiprism 2 specimens

(Figure 5b, c).

4.3.2.2   Failure loads

The mechanical tests performed to determine the failure loads of the specimens showed that the bicapped square antiprism 3, bicapped square antiprism 2 and bicapped square antiprism 1 specimens failed after applying 1212 ± 45.5 N, 1074 ± 273.6 N, and 1110 ± 185.9 N, respectively (Figure 6). The bicapped trigonal antiprism and bicapped cube specimens
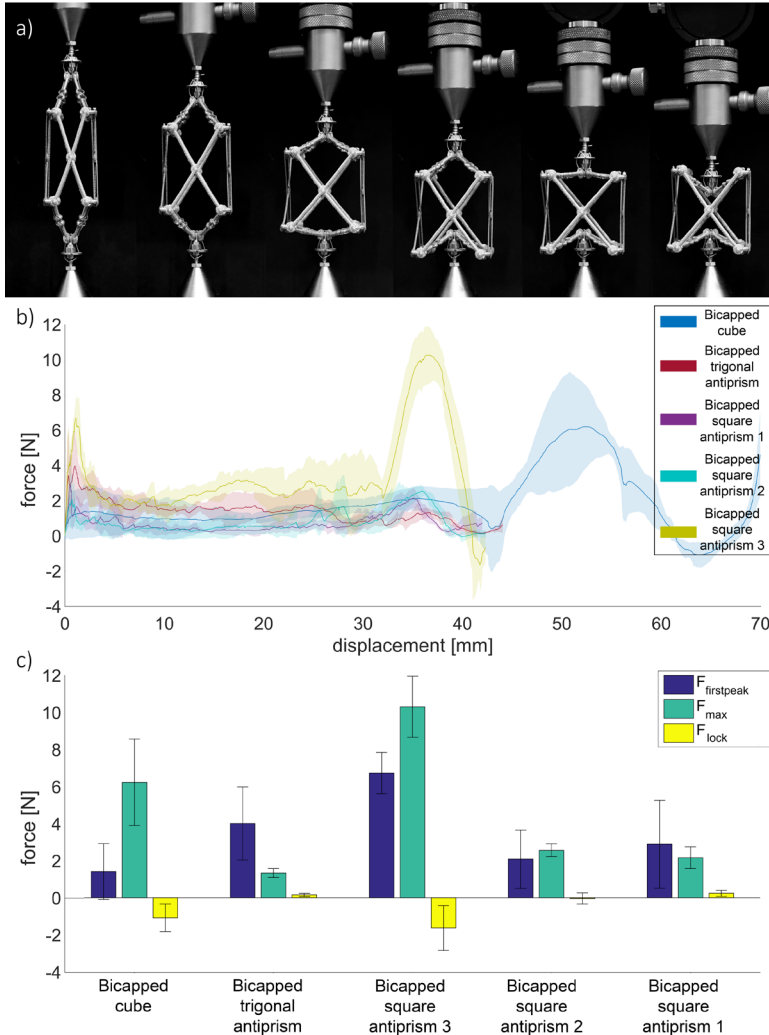

Figure 4. The results of the compression tests where the proximal vertex moves inward later than the distal vertex. a) An example of a bicapped cube compression where the distal vertex opens firsts, followed by the inward movement of the distal vertex and finally the inward movement of the proximal vertex. b) The force-displacement curves of the different structures. c) A bar plot with $F_{firstpeak}$, F_{max}, and F_{lock} and the corresponding standard deviations measured for all the deployable structures studied here.

failed at much lower loads (547 ± 64.1 N and 232 ± 5.5 N, respectively) (Figure 6). At the point of their failure, the rigid rods bent and buckled (Figure 6a). All wavelike rods remained intact.

4.4 Discussion

In this study, we presented the concept of non-assembly AM deployable mechanisms for application as orthopedic implants. An important aspect of these new designs is that they can be manufactured from metals using a powder bed fusion process (*i.e.*, SLM) and
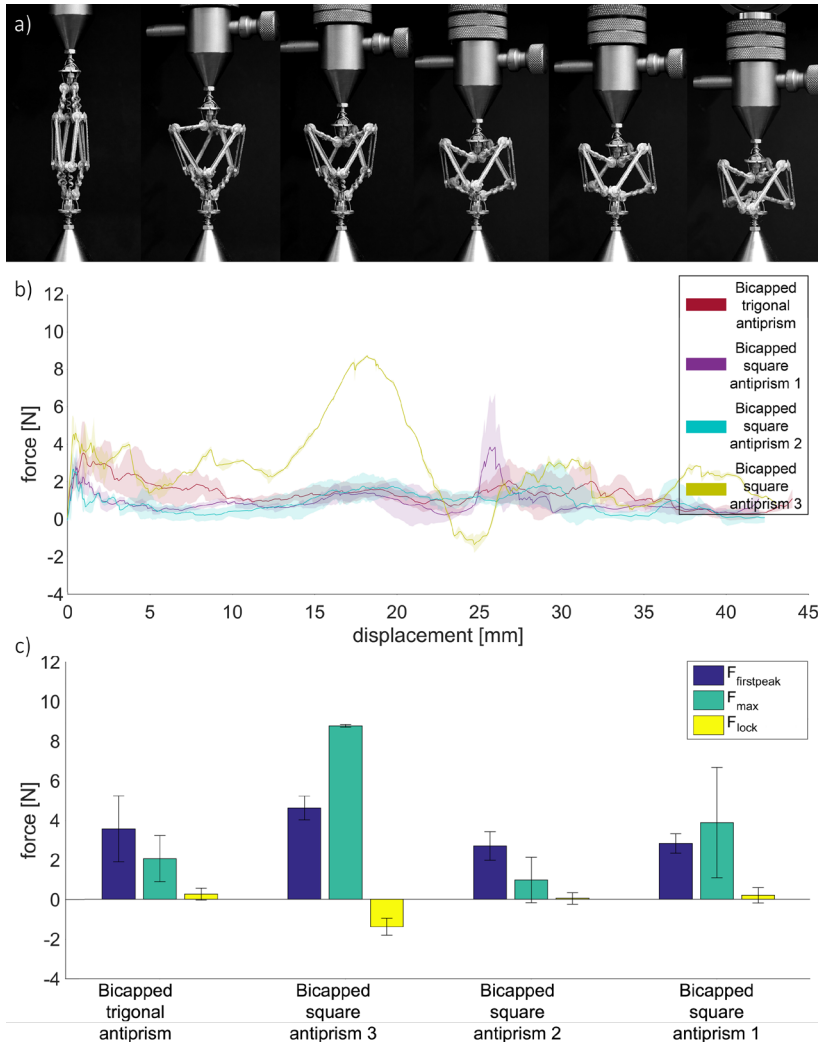

Figure 5. The results of the compression tests where the distal vertex moves inward after the proximal vertex. a) An example of the compression of a bicapped trigonal antiprism specimen where the proximal vertex opens firsts, followed by the inward movement of the proximal vertex and finally the inward movement of the distal vertex. b) The force-displacement curves of the different structures. c) A bar plot with $F_{firstpeak}$, F_{max}, and F_{lock} and the corresponding standard deviations measured for all the deployable structures studied here.

without a need for internal supports (*i.e.*, in the clearance space of the joints). Both the non-assembly nature of the designs and the fact that these structures were manufactured from metals distinguish this study from our previous study where we introduced the concept of deployable meta-implants for the first time [27]. The non-assembly nature of the designs means that their manufacturing step is practical and straightforward to upscale, while the fact that they are made from metals means that they exhibit much higher mechanical properties as compared to the previous polymeric designs.

4.4.1 Deployability

The deployable porous biomaterials presented in this study could all reconfigure from an elongated retracted state to a radially expanded and lengthwise shortened deployed configuration. The small circumdiameter of the retracted specimens makes it possible to insert the porous biomaterials via a small incision into the body. A large standard deviation of 40% was observed for the increase in circumdiameter of the bicapped cube specimens. This could be explained by the much smaller circumdiameter of one of the specimens in its retracted state. Since all specimens were manufactured simultaneously and were based on the same design, this behavior seems to be an effect of the SLM process. The bicapped trigonal antiprism specimens had the smallest circumdiameter in their retracted state, which can be explained by the number of joint bearings at the sides of the geometry. The joint bearings of the antiprism specimens touch each other in their retracted configuration. Since
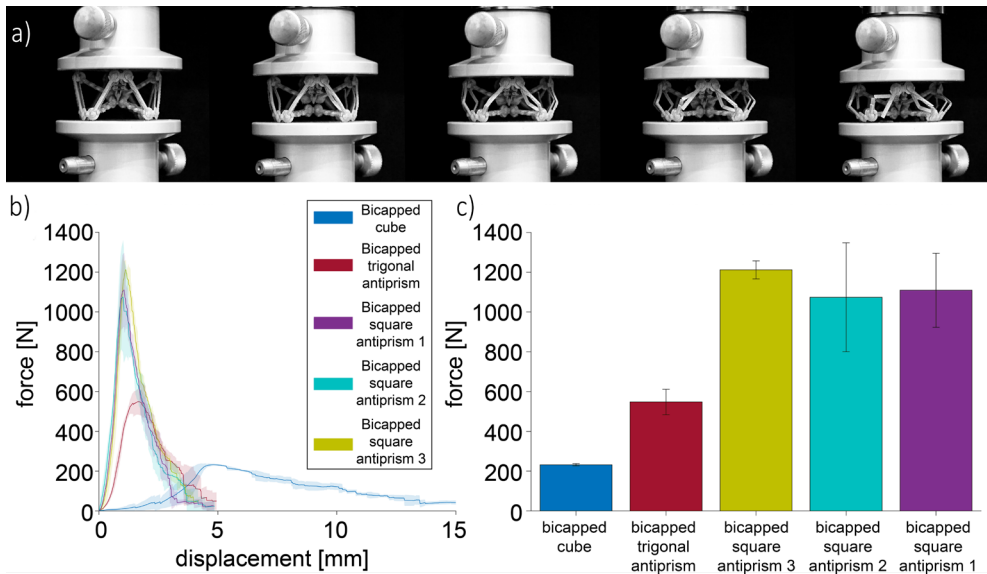

Figure 6. The results of the compression to failure tests. a) An example of a bicapped square antiprism specimen being compressed. b) The force-displacement curves of the different structures. c) A bar plot with the load to failure of the different geometries.

the bicapped trigonal antiprism specimens have fewer joint bearings, these specimens can be made smaller than the bicapped square antiprism specimens. The circumdiameters of all the specimens in their deployed state are dependent on the length of the wavelike rods (a). Due to the similar length of these rods for the antiprism specimens, the circumdiameter of the deployed state of these specimens is comparable. Due to the smaller radial dimensions in its retracted state, the bicapped trigonal antiprism geometry would be the most suitable for implantation using minimally invasive surgery.

4.4.2   Mechanical performance

4.4.2.1   Deployment forces

This concept of deployable mechanisms as potential porous biomaterials for the treatment of large bony defects using minimally invasive surgery requires easy deployment when brought into the bone defect. The deployable structures proposed in this paper are easily reconfigurable by applying a compressive force at their proximal and distal vertices. Although our designs can be easily deployed by hand or by a mechanical testing machine with a maximum force of 10.3 ± 1.6 N, a dedicated minimally invasive surgery tool would be required to deploy such type of implants inside the body. The maximum force required during the deployment process was reached during the deformation of the wavelike elements at the point where the maximum circumradius is reached ($\alpha = 0°$). This means that the maximum force can be controlled by adjusting the oversize, which depends on the length of the wavelike rods a and the designed maximum circumradius L_x. Longer wavelike rods need to deform more than shorter wavelike rods when L_x is kept constant. In Figures 4b and c, it can be seen that the bicapped square antiprisms with smaller values for a, indeed, require a lower maximum force when the inward movement of the proximal vertex is the last step in the deployment process. However, this theory does not seem to hold when the inward movement of the distal vertex is the last step in the deployment process. Moreover, the geometry of the deployable structure affects the force required to deform the wavelike rods at the point where the maximum circumradius is reached. While the specimens designed based on the bicapped trigonal antiprism and bicapped square antiprism 2 have the same oversize value, more force is required to deform the wavelike rods of the latter type. This could be explained by the number of the wavelike rods connected to the proximal and distal vertices. Only three wavelike rods need to be deformed simultaneously in the bicapped trigonal antiprism while four rods need to be deformed in the bicapped square antiprism.

Our observation of a negative force during the deployment of the bicapped square antiprism 3, bicapped square antiprism 2, and the bicapped cube specimens show that there is a snap-through behavior present in some deployment sequences. This effect is enabled by the deformation of the wavelike rods connected to the proximal and distal vertices, which act as bi-stable beams at the point where the maximum circumradius L_x is reached. Bi-stable

beams can snap from one load-bearing configuration to another when the load applied reaches a critical level [36]. In one of our previous studies [27], we used this type of instability to develop our first concepts of deployable meta-implants.

4.4.2.2   Failure loads

Large bony defects can occur at any location, either load-bearing or not. The deployed structures evaluated in this paper could support loads up to 1212 ± 45.5 N before bending or buckling occurs. This is a significant improvement as compared to the load-bearing properties of our previously developed concepts for deployable implants and is already within the lower range of the compressive loads reported in the literature for spinal compression (relevant for the treatment of fractured vertebrae) [37]. Our multi-stable deployable PLA (polylactic acid) meta-biomaterials made of bi-stable elements [27] and bi-stable panels [28] could respectively support loads of ≈ 10 N or ≈ 35 N, before retraction would occur. This large difference can be mainly explained by the definition of 'deployed configuration' of our PLA specimens and these non-assembly mechanisms. The PLA specimens were defined as deployed when they were expanded in all directions, while these non-assembly mechanisms are defined as deployed when they are radially expanded and lengthwise shortened. In their deployed state, the non-assembly mechanisms are, therefore, already retracted in their axial direction and locked in this deployed configuration. Both types of deployment (*i.e.*, deployment in all directions or radial deployment upon axial compression) could potentially be applied as deployable bone substitutes. While our previous designs of multi-stable structures and foldable designs can be transported in a compact state in all directions, these non-assembly mechanisms can be easily inserted into the body due to their elongated shape in their retracted configuration. It is clear that the designs with the second type of deployment are superior in terms of load-bearing properties.

The force-displacement curves show that the force is slowly building up for the bicapped cube specimens, while the force of the bicapped square antiprisms quickly increases at the start of the test. This large difference could be explained by the number and length of the rigid rods of the different geometries. While the force is distributed over eight short rigid rods in the bicapped square antiprism specimens, the force is distributed over fewer and longer rods in the bicapped trigonal antiprism and bicapped cube specimens. The shorter rods in the bicapped square antiprism specimens are less susceptible to bending and buckling as compared to the longer rods present in the bicapped cube specimens. Similar results were found by El-Sayed *et al.* (2020) [38], who used SLM to manufacture diamond lattice structures with various strut thicknesses and lengths. The compressive strength was observed to increase with the strut thickness and to decrease with the strut length [38]. The different mechanical properties of our non-assembly mechanisms can be used to optimize the geometrical design of the implants to best suit the particular application at hand.

4.4.3   Future work

Although our non-assembly manufactured deployable implants show many advantages, some limitations should be addressed. SLM still has its limitations when it comes to the accuracy of printing. The smallest line thickness is dependent on the laser spot size and is found to be 200 μm with a laser beam size of 100 μm [39]. Since the revolute joints in our designs are used to enable the reconfiguration of the structures, it is challenging to reduce the size of the joint bearings significantly. These joint bearings are responsible for the circumdiameter of the retracted mechanisms, meaning that the diameter of the retracted mechanisms presented in this paper cannot be significantly reduced. We showed that different non-assembly deployable mechanisms can be made using single-step additive manufacturing. The designs and fabrication approaches presented in this study can be exploited to advance the applications of non-assembly mechanisms in other areas as well.

4.5   Conclusions

We designed and additively manufactured non-assembly deployable structures for application as orthopedic implants. SLM was used to manufacture these deployable structures from a medical grade titanium alloy that is widely used for the fabrication of orthopedic implants. SLM enables the integration of revolute joints, wavelike elements, rigid rods, and mechanical constraints. Additionally, this approach made the assembly of different components after manufacturing redundant and only the removal of the support structures and ultrasonic cleaning were required to make the deployable structures functional. Various geometries with different lengths for the rigid and wavelike rods were mechanically tested to determine the forces required to deploy the structures and to determine their failure loads. The porous structure of such implants is advantageous for bone ingrowth while their ability to reconfigure from an elongated to a load-bearing structure enables implantation using minimally invasive surgery. As compared to other implants that have been manufactured using SLM, the main advantage of these mechanisms is their ability to change their configuration. However, since the mechanisms reported here are the first SLM manufactured deployable non-assembly bone substitutes, future studies are required to further develop such mechanisms and to make them suitable as orthopedic implants.

References

[1] M. Ansari, Bone tissue regeneration: biology, strategies and interface studies, Progress in biomaterials (2019) 1-15.

[2] J.J. Li, C.R. Dunstan, A. Entezari, Q. Li, R. Steck, S. Saifzadeh, A. Sadeghpour, J.R. Field, A. Akey, M. Vielreicher, A Novel Bone Substitute with High Bioactivity, Strength, and Porosity for Repairing Large and Load-Bearing Bone Defects, Advanced healthcare materials 8(8) (2019) 1801298.

[3] C. Laurencin, Y. Khan, S.F. El-Amin, Bone graft substitutes, Expert review of medical devices 3(1) (2006) 49-57.

[4] Y. Yu, Y. Wang, W. Zhang, H. Wang, J. Li, L. Pan, F. Han, B. Li, Biomimetic periosteum-bone substitute composed of preosteoblast-derived matrix and hydrogel for large segmental bone defect repair, Acta biomaterialia 113 (2020) 317-327.

[5] C. Delloye, Tissue allografts and health risks, Acta orthopaedica Belgica 60 (1994) 62-67.

[6] S. Sahmani, A. Khandan, S. Esmaeili, S. Saber-Samandari, M.G. Nejad, M. Aghdam, Calcium phosphate-PLA scaffolds fabricated by fused deposition modeling technique for bone tissue applications: fabrication, characterization and simulation, Ceramics International 46(2) (2020) 2447-2456.

[7] Y. Lai, H. Cao, X. Wang, S. Chen, M. Zhang, N. Wang, Z. Yao, Y. Dai, X. Xie, P. Zhang, Porous composite scaffold incorporating osteogenic phytomolecule icariin for promoting skeletal regeneration in challenging osteonecrotic bone in rabbits, Biomaterials 153 (2018) 1-13.

[8] S.K. Nandi, G. Fielding, D. Banerjee, A. Bandyopadhyay, S. Bose, 3D-printed β-TCP bone tissue engineering scaffolds: Effects of chemistry on in vivo biological properties in a rabbit tibia model, Journal of materials research 33(14) (2018) 1939-1947.

[9] A. Ataee, Y. Li, M. Brandt, C. Wen, Ultrahigh-strength titanium gyroid scaffolds manufactured by selective laser melting (SLM) for bone implant applications, Acta Materialia 158 (2018) 354-368.

[10] Y. Li, Y. Ding, K. Munir, J. Lin, M. Brandt, A. Atrens, Y. Xiao, J.R. Kanwar, C. Wen, Novel β-Ti35Zr28Nb alloy scaffolds manufactured using selective laser melting for bone implant applications, Acta biomaterialia 87 (2019) 273-284.

[11] H. Kolken, K. Lietaert, T. van der Sloten, B. Pouran, A. Meynen, G. Van Loock, H. Weinans, L. Scheys, A.A. Zadpoor, Mechanical performance of auxetic meta-biomaterials, journal of the mechanical behavior of biomedical materials 104 (2020) 103658.

[12] S. Wang, L. Liu, K. Li, L. Zhu, J. Chen, Y. Hao, Pore functionally graded Ti6Al4V scaffolds for bone tissue engineering application, Materials & Design 168 (2019) 107643.

[13] Y. Li, P. Pavanram, J. Zhou, K. Lietaert, P. Taheri, W. Li, H. San, M. Leeflang, J. Mol, H. Jahr, Additively manufactured biodegradable porous zinc, Acta Biomaterialia 101 (2020) 609-623.

[14] C. Shuai, Y. Cheng, Y. Yang, S. Peng, W. Yang, F. Qi, Laser additive manufacturing of Zn-2Al part for bone repair: Formability, microstructure and properties, Journal of Alloys and Compounds 798 (2019) 606-615.

[15] P. Wen, L. Jauer, M. Voshage, Y. Chen, R. Poprawe, J.H. Schleifenbaum, Densification behavior of pure Zn metal parts produced by selective laser melting for manufacturing biodegradable implants, Journal of Materials Processing Technology 258 (2018) 128-137.

[16] Y. Li, J. Zhou, P. Pavanram, M. Leeflang, L. Fockaert, B. Pouran, N. Tümer, K.-U. Schröder, J. Mol, H. Weinans, Additively manufactured biodegradable porous magnesium, Acta biomaterialia 67 (2018) 378-392.

[17] C. Gao, S. Li, L. Liu, S. Bin, Y. Yang, S. Peng, C. Shuai, Dual alloying improves the corrosion resistance of biodegradable Mg alloys prepared by selective laser melting, Journal of Magnesium and Alloys (2020).

[18] F. Bär, L. Berger, L. Jauer, G. Kurtuldu, R. Schäublin, J.H. Schleifenbaum, J.F. Löffler, Laser additive manufacturing of biodegradable magnesium alloy WE43: a detailed microstructure analysis, Acta Biomaterialia 98 (2019) 36-49.

[19] D. Carluccio, C. Xu, J. Venezuela, Y. Cao, D. Kent, M. Bermingham, A.G. Demir, B. Previtali, Q. Ye, M. Dargusch, Additively manufactured iron-manganese for biodegradable porous load-bearing bone scaffold applications, Acta Biomaterialia 103 (2020) 346-360.

[20] Y. Li, H. Jahr, P. Pavanram, F. Bobbert, U. Puggi, X.-Y. Zhang, B. Pouran, M. Leeflang, H. Weinans, J. Zhou, Additively manufactured functionally graded biodegradable porous iron, Acta biomaterialia 96 (2019) 646-661.

[21] Y. Chen, J. Lu, Minimise joint clearance in rapid fabrication of non-assembly mechanisms, International Journal of Computer Integrated Manufacturing 24(8) (2011) 726-734.

[22] D. Bergqvist, G. Lowe, Venous thromboembolism in patients undergoing laparoscopic and arthroscopic surgery and in leg casts, Archives of internal medicine 162(19) (2002) 2173-2176.

[23] C.-H. Kuo, J.S. Dai, Robotics for minimally invasive surgery: a historical review from the perspective of kinematics, International symposium on history of machines and mechanisms, Springer, 2009, pp. 337-354.

[24] V. Mais, S. Ajossa, S. Guerriero, M. Mascia, E. Solla, G.B. Melis, Laparoscopic versus abdominal myomectomy: a prospective, randomized trial to evaluate benefits in early outcome, American Journal of Obstetrics and Gynecology 174(2) (1996) 654-658.

[25] S.S. Biere, M.I. van Berge Henegouwen, K.W. Maas, L. Bonavina, C. Rosman, J.R. Garcia, S.S. Gisbertz, J.H. Klinkenbijl, M.W. Hollmann, E.S. De Lange, Minimally invasive versus open oesophagectomy for patients with oesophageal cancer: a multicentre, open-label, randomised controlled trial, The Lancet 379(9829) (2012) 1887-1892.

[26] R. Treuting, Minimally invasive orthopedic surgery: arthroscopy, Ochsner Journal 2(3) (2000) 158-163.

[27] F. Bobbert, S. Janbaz, A. Zadpoor, Towards deployable meta-implants, Journal of Materials Chemistry B 6(21) (2018) 3449-3455.

[28] F. Bobbert, S. Janbaz, T. van Manen, Y. Li, A. Zadpoor, Russian doll deployable meta-implants: Fusion of kirigami, origami, and multi-stability, Materials & Design (2020) 108624.

[29] F. Calignano, Design optimization of supports for overhanging structures in aluminum and titanium alloys by selective laser melting, Materials & Design 64 (2014) 203-213.

[30] Y.-q. Yang, X.-b. Su, D. Wang, Y.-h. Chen, Rapid fabrication of metallic mechanism joints by selective laser melting, Proceedings of the Institution of Mechanical Engineers, Part B: Journal of Engineering Manufacture 225(12) (2011) 2249-2256.

[31] A. Boschetto, L. Bottini, Manufacturability of non-assembly joints fabricated in AlSi10Mg by selective laser melting, Journal of Manufacturing Processes 37 (2019) 425-437.

[32] J.S. Cuellar, G. Smit, D. Plettenburg, A. Zadpoor, Additive manufacturing of non-assembly mechanisms, Additive Manufacturing 21 (2018) 150-158.

[33] Y. Liu, J. Zhang, Y. Yang, J. Li, J. Chen, Study on the influence of process parameters on the clearance feature in non-assembly mechanism manufactured by selective laser melting, Journal of Manufacturing Processes 27 (2017) 98-107.

[34] A. Boschetto, L. Bottini, M. Eugeni, V. Cardini, G.G. Nisi, F. Veniali, P. Gaudenzi, Selective laser melting of a 1U cubesat structure. Design for additive manufacturing and assembly, Acta Astronautica 159 (2019) 377-384.

[35] S. Leeflang, S. Janbaz, A.A. Zadpoor, Metallic clay, Additive Manufacturing 28 (2019) 528-534.

[36] Y. Zhang, M. Tichem, F. van Keulen, Rotational snap-through behavior of multi-stable beam-type metastructures, International Journal of Mechanical Sciences (2020) 106172.

[37] M. Hajihosseinali, N. Arjmand, A. Shirazi-Adl, Effect of body weight on spinal loads in various activities: a personalized biomechanical modeling approach, Journal of biomechanics 48(2) (2015) 276-282.

[38] M.A. El-Sayed, K. Essa, M. Ghazy, H. Hassanin, Design optimization of additively manufactured titanium lattice structures for biomedical implants, The International Journal of Advanced Manufacturing Technology 110(9) (2020) 2257-2268.

[39] F. Calignano, M. Lorusso, J. Pakkanen, F. Trevisan, E. Ambrosio, D. Manfredi, P. Fino, Investigation of accuracy and dimensional limits of part produced in aluminum alloy by selective laser melting, The International Journal of Advanced Manufacturing Technology 88(1-4) (2017) 451-458.

5

Multi-stable structures

Meta-biomaterials exhibit unprecedented or rare combinations of properties not usually found in nature. Such unusual mechanical, mass transport, and biological properties could be used to develop novel categories of orthopedic implants with superior performance, otherwise known as meta-implants. Here, we use bi-stable elements working on the basis of snap-through instability to design deployable meta-implants. Deployable meta-implants are compact in their retracted state, allowing them to be brought to the surgical site with minimum invasiveness. Once in place, they are deployed to take their full-size load-bearing shape. We designed five types of meta-implants by arranging bi-stable elements in such a way to obtain a radially-deployable structure, three types of auxetic structures, and an axially-deployable structure. The intermediate stable conditions (i.e. multi-stability features), deployment force, and stiffness of the meta-implants were found to be strongly dependent on the geometrical parameters of the bi-stable elements as well as on their arrangement.

We have recently proposed [1] the concept of meta-implants as orthopedic implants that exploit the rare or unprecedented properties of meta-biomaterials [2-4] to improve their performance and longevity. For example, hybrid meta-biomaterials with a rational distribution of both negative and positive Poisson's ratios could be used to improve bone-implant contact and potentially its longevity [1].

The unusual properties of meta-biomaterials, in turn, originates from their small-scale (*i.e.,* micro/nano-scale) geometrical design. In that sense, meta-biomaterials are similar to other types of designer materials such as mechanical [5-9] or acoustic [10-13] metamaterials.

Here, we propose a new type of meta-implants called 'deployable meta-implants'. Deployable implants are undersized in their compact mode, which allows them to be brought to the surgical site with a smaller incision and minimum invasiveness. Once they are in place, an activation mechanism deploys the implant into a full-size load-bearing shape. Moreover, deployable implants are fully porous to allow for bone ingrowth.

The main mechanisms used here for development of deployable implants are the mechanical concepts of bi- [14-16] and multi-stability [17-19] that are, for example, seen in snap-through instability systems. Bi-stable structures are part of the instability-based metamaterials [20] and are often based on a snap-through mechanism which enables the structure to shift between two different stable equilibria [21, 22]. Due to the existence of two stable equilibrium states, no external forces are required to maintain the structural configuration once it is configured in one of those two positions [21, 23, 24]. By combining bi-stable structures, it is possible to develop multi-stable structures which have more than two stable equilibria [23-29]. Contrary to structures with only one stable, or rigid configuration, these structures could adapt their configuration to specific situations [24]. Two important properties of bi- and multi-stable structures are their capability to be deployed and to absorb energy [29]. Bi-stable and multi-stable structures could therefore be used in the design of space frame structures [29], actuators [30], energy absorbing materials [31], and energy harvesters [32, 33]. For biomedical applications, the concept of multi-stable stent [34] has been presented before for cardiovascular applications.

The basic elements and assembled multi-stable structures developed in this study are the first step towards deployable structures for application as bone implants. We designed two types of basic bi-stable elements with single curved (D1) and double curved (D2) side hinges where the joint at the center is similar (Figure 1a).

The basic bi-stable elements consisted of flexible components which act as joints and rigid components that fulfil structural functions. Several design parameters including the length (L) [mm], angle (α) [°], and width (w) [mm] (Figure 1b) determine the mechanical and bi-stable behaviors of D1 and D2. There are at least four different ways of connecting the basic bi-stable elements (T1, T2, T3, T4) to create more complex (multi-stable) mechanisms

(Figure 1d, e).

We performed a parametric study (parameters listed in Table 1) to evaluate the effects of the different parameters on both types of behaviors. The design variants were named according to the value of the examined parameters. For example, specimens made according to D1 with L = 40 mm, α = 30°, and w = 4 mm were referred to as D140304.

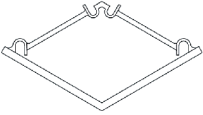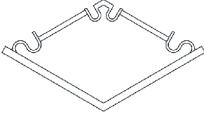| Design 1	L [mm]	α [°]	w [mm]	Design 2	L [mm]	α [°]	w [mm]
	40	30	4		40	30	4
	45	30	4		45	30	4
	50	30	4		50	30	4
	55	30	4		55	30	4
	45	35	4		45	35	4
	45	40	4		45	40	4
	45	30	6		45	30	6
	45	35	6		45	35	6
	45	40	6		45	40	6

Table 1. The different variants of two basic bi-stable element design with varying values of dimensions L, α, and w.

3D printers working on the basis of fused deposition modeling (FDM) [35] (Ultimaker 2+, Geldermalsen, The Netherlands) were used to fabricate the bi-stable (and later multi-stable) structures. A biocompatible polymer, namely Poly (lactic acid) (PLA), was used as the main material for printing the basic elements as well as the connecting parts (Figure 2f) which connected the bi-stable elements for the assembly of the multi-stable structures. In addition to being a biocompatible polymer [36, 37], PLA is biodegradable [37, 38]. It has also proven to be a suitable material for implants onto which cells could adhere and grow [36-38]. The connecting parts were designed such that the proposed connection types could be assembled, and that these small assemblies could be connected together.

A mechanical testing machine (Lloyd LR5K) was used to measure the minimum forces required to make the elements shift from their deployed or retracted configuration to their other stable configuration (F_s). To make a distinction between these forces for the compression and tensile tests, F_{Sc} and F_{St} were used, respectively. Moreover, the minimum forces required to switch the configurations back to their configuration at the start of the test F_{SB} for both compression (F_{SBc}) and tensile tests (F_{SBt}) were evaluated [39]. All compression and tensile tests were performed with a deformation rate of 10 mm/min. Because the elements were printed in their deployed state, the elements were first tested under compression. When the element was bi-stable after the load was removed, the sample was also tested under tension (Figure 1f). For the basic elements whose F_{Sc} was below 5 N, a 5 N load cell was used. A 100 N load cell was used for the mechanical tests of the assemblies and the basic elements whose F_{Sc} was above 5 N. In order to control the direction of the load and to measure the load at all times, extra parts were designed and printed in a similar way to the bi-stable elements (Figure 2f). All mechanical tests reported in this study were repeated at least three times, unless the design failed at the first trial. The mechanical tests were terminated after the

force-deflection curve intersected the x-axis for the second time.

Changing the parameters L, α, and w affected the F_S and F_{SB} values, which are the maximum and minimum forces in the force-deflection graph, respectively (Figure 1g-j, Table 2). The mean values of the equilibrium paths are shown in the force-deflection curves of the different designs (Figure 1g-j). All variants showed typical force-deflection curves for bi-stable structures. These curves start and end with regions showing a positive stiffness, which are separated by a region with a negative stiffness (Figure 1g-j). It was found (data not shown) that F_{Sc} reduces from the first shape shifting cycle to about the third one, and that the force-deflection curves become more constant afterwards. The curves of both D1 and D2 showed a small increase in F_{Sc} and F_{St} when the width of the elements increased from 4 to 6 mm and the corresponding deflection to reach the F_{Sc} and F_{St} shifted to the right (Figure 1g, h). The stiffness, amount of deflection, F_{Sc}, and F_{St} were affected by the values of α and L. Increasing α led to a higher stiffness, a higher F_{Sc} and F_{St}, and more deflection of the elements (Figure 1h), while an increase of L led to a slightly lower initial slope during compression. For four variants, D145354, D145356, D145404, and D145406, F_{SBc} was positive (Figure 1g, Table 2).

As for D2, where the side joints consisted of two curves, a lower initial slope and lower values for F_S and F_{SB} were found (Figure 1i, j). Contrary to the D1 variants, the deflection of the D2 variants reduced when the width increased from 4 to 6 mm (Figure 1j). For three variants of D2 (*i.e.,* D240304, D245306, and D245406) F_{SBc} was positive (Figure 1i). The positive values of F_{SBc} found for the variants of D1 and D2 agreed with the observation that these elements were not bi-stable.

In general, due to the stiffer side hinges of D1, the D1 variants required more force to shift from the deployed configuration to the retracted configuration as compared to the D2 variants. For both designs, higher forces were required to make the structures shift from their deployed configuration back to their retracted configuration than vice versa. This could be explained by the energy stored in the deflected members of the basic elements during compression [25]. Therefore, their retracted state is, as desired, less stable than their deployed state in which the basic elements were printed. The parametric study showed that the variant D145304 is the most stable in its retracted configuration. We therefore used this design variant for the remainder of the study.

By combining the basic bi-stable elements with the different connection types (T1, T2, T3, T4), five different 3D deployable structures were assembled (Figure 2a-e). Among these structures, different ways of deployment and retraction were seen. Two of the multi-stable structures retract and deploy radially or axially and exhibit a positive and zero Poisson's ratio, respectively, while three others behave auxetically (*i.e.,* exhibit negative Poisson's ratio). The ring structure, consisting of elements assembled by a combination of T4 connections, deployed and retracted radially (Figure 2a). Moreover, three different auxetic structures were developed, where the structures retracted in all directions upon compression (Figure 2b-d). The opposite occurred when the structures were subjected to tension. In two of
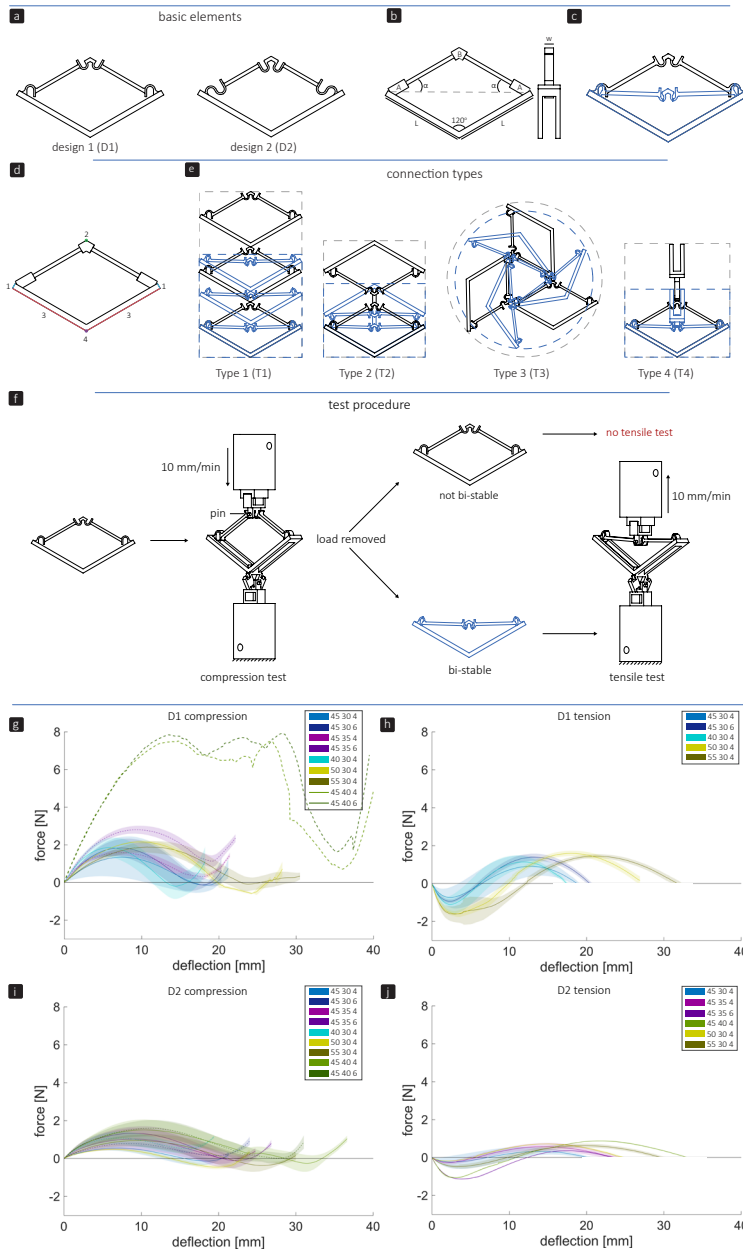
Figure 1. Overview of the two basic element designs. a) two basic bi-stable element designs, D1 and D2, b) parameters of the basic element, c) working mechanism of a basic element, d) connection sites for assembly, e) different connection types, type 1 (T1) and type 2 (T2): 2D assembly of basic bi-stable elements reconfigures axially, Type 3 (T3): 2D assembly of three bi-stable elements changes dimensions radially, Type 4 (T4): 3D assembly reconfigures axially. The black and blue lines represent the deployed and retracted configurations, respectively. f) Testing procedure and setup for both compression and tensile tests. A pin at the top of the basic element ensured that both compression and tensile forces were measured at all times. g- j) Force-deflection diagrams all variants of bi-stable element design 1 (g,h) and design 2 (i,j) with different values for parameters *L* [mm], *α* [°], and *w* [mm], under compression (g,i) and tension (h,j).

these structures (*e.g.*, auxetic structure 1 (Figure 2b) and 3 (Figure 2d)) a combination of T3 connections was used. Auxetic structure 2 was designed by combining rotated versions of T2 connections. The fifth structure (Figure 2e) was similar to the T1 connection (Figure 1e), where deployment and retraction occurred axially in the direction of the applied force.

The assemblies showed different changes in dimensions (height (h), width (w), and circumference (c)) from the retracted to deployed configuration (Figure 2a-e). Structure

Sample	Design 1								Design 2							
	Compression				Tension				Compression				Tension			
L α w	F_{Sc}	SD	F_{SBc}	SD	F_{St}	SD	F_{SBt}	SD	F_{Sc}	SD	F_{SBc}	SD	F_{St}	SD	F_{SBt}	SD
40 30 4	1.85	0.5	-0.20	0.7	-1.35	0.3	1.10	0.5	1.09	0.5	0.53	0.3	-0.24	0.2	0.33	0.2
45 30 4	1.34	1.1	-0.15	0.3	-0.73	0.5	0.91	0.5	0.55	0.5	-0.14	0.2				
45 30 6	1.83	0.5	-0.13	0.2	-0.93	0.1	1.39	0.2	0.79	0.2	0.15	0.1	-0.27	0.2	0.57	0.5
45 35 4	1.25	0.1	0.31	0.2					1.03	0.6	-0.01	0.6	-1.13	0.4	0.36	0
45 35 6	2.80	0.2	1.13	0.3					1.33	0.4	-0.11	0.4	-1.06	0.4	0.88	0
45 40 4	7.51		0.71						1.51	0.6	-0.25	0.6				
45 40 6	7.84		1.63						1.69	0.4	0.02	0.4				
50 30 4	2.15	0.1	-0.59	0.1	-1.44	0.4	1.71	0.3	0.49	0.3	-0.46	0.1	-0.18	0.1	0.72	0
55 30 4	1.88	0.3	-0.09	0.4	-1.30	0.5	1.69	0.4	0.94	0.4	-0.36	0.3	-0.49	0.3	0.62	0.1

Table 2. The values of the switching forces of the compression tests (F_{Sc} and F_{SBc}) and tensile tests (F_{St} and F_{SBt}) determined for all variants of the bi-stable elements D1 and D2 from the force-deflection diagrams

5 showed the largest change (h:170%), followed by the ring structure (*c*:136%), auxetic structure 2 (*c*:127%, *h*:107%), auxetic structure 1 (*h*:126%, *w*:107%), and finally auxetic structure 3 (*h*:115%, *w*:111%). The ring structure required the highest force for complete deployment (Figure 2f, g). For this type of structure, additional parts were developed to make the structure deploy or retract under compression or tension, respectively. The F_{Sc} values of the different stable configurations were similar during compression, while F_{St} increased during tension (Figure 2f, g). Auxetic structure 1 showed an increase in load both under compression and tension, followed by one valley or a valley, a peak and a valley, respectively (Figure 2f,g). The force-deflection curve of auxetic structure 2 during compression started and ended with a linear region with increasing loads up to about 10 N. After this peak, there was a negative slope consisting of three peaks and four valleys (Figure 2f).

Auxetic structure 3 showed two clearly different curves for compression and tension (Figure 2f, g). While the force peaks of this type of structure increased when it was subjected to compression, the first peak in the curve of the tensile tests was the highest, followed by some lower peaks (Figure 2f, g). Structure 5 deployed and retracted only in the direction of the applied load and showed three peaks of similar heights and three valleys when subjected to either tension or compression (Figure 2f, g).

This study showed that by assembling basic elements in various ways, different multi-stable structures which reconfigure differently could be obtained. In addition to two multi-stable structures which deployed and retracted radially or axially, three auxetic structures were developed. In the case of the ring structure, increasing forces were found during the tensile tests as compared to the more equal forces during compression tests. Upon compression, the ring was pushed outwards which made the elements shift from their retracted configuration to their deployed configuration. The results of the basic elements showed that their retracted configuration is less stable than their deployed configuration, hence the lower forces during the compression of the ring structure. The opposite held when the structure was subjected to tension, when the elements had to shift from their deployed state to their retracted state.

When auxetic structure 1 was subjected to tension or compression, elements were gradually snapping into their other stable configuration. As could be seen in the force-deflection graph, the force drops suddenly at some points. At these points of deflection, a combination of several elements in the T3 connection snapped through at the same time.

The force-deflection curves of auxetic structure 2 showed that for both compression and tension, the first force peak was high, meaning that about 10 N was required to make the first snap-through happen of one of the elements within the structure. However, when the first element switched its configuration, the other elements followed shortly after. During both the tensile and compression tests, we observed that the elements reconfigure gradually but quickly after each other, which explains the similar drops in force after the succeeding F_S were reached.
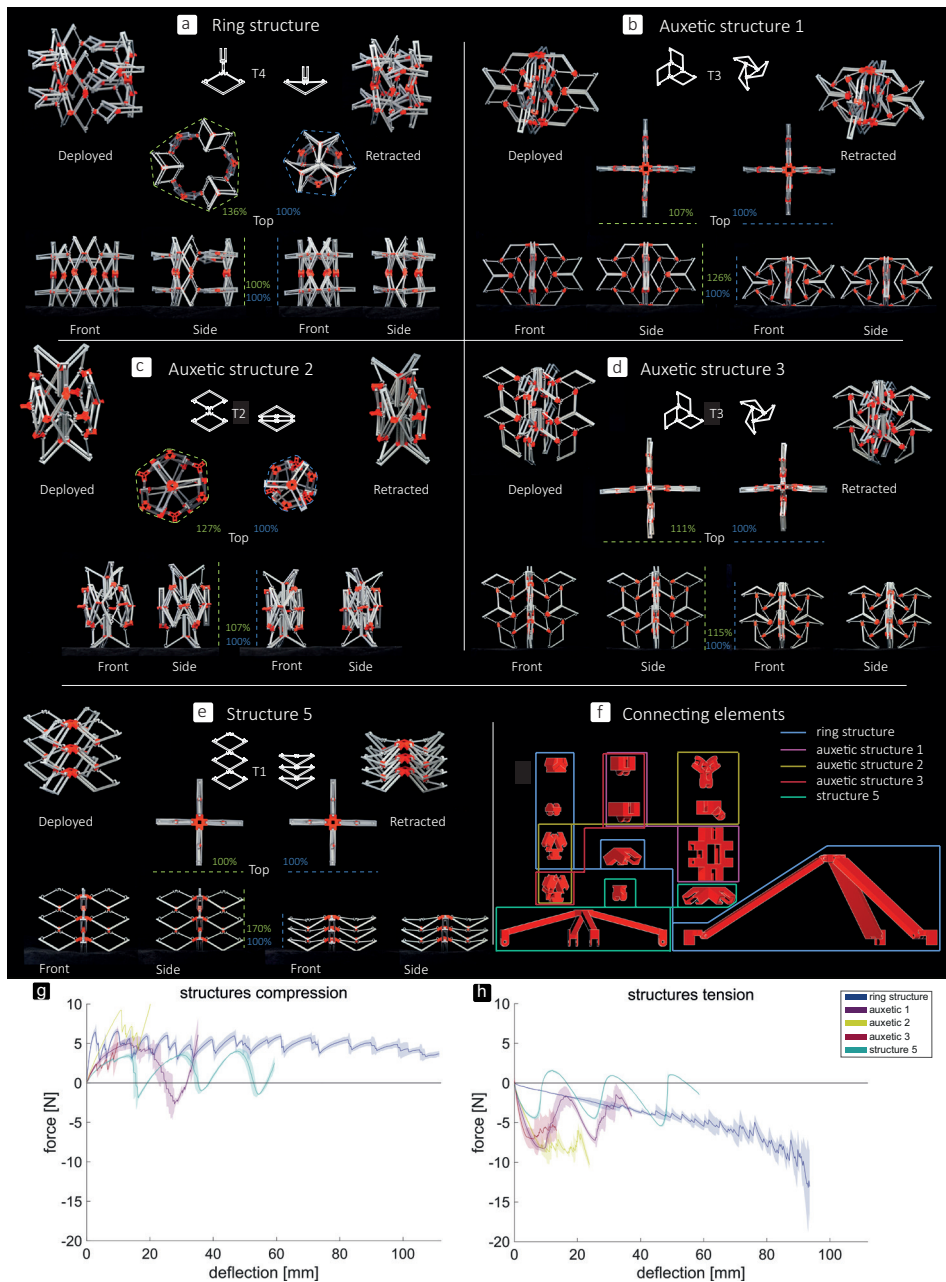
Figure 2. Pictures of different 3D assemblies in their fully deployed and retracted stable configurations. a) ring structure, deploying and retracting radially. b, c, d) auxetic structures, retracting upon compression in all directions and vice versa upon tension. e) structure 5, axially deployable and retractable. f) connecting elements to assemble the deployable structures. The elements surrounded by one color are used for the assemblage of the corresponding structure. The large parts were connected to the top of structure 5 and to both the top and bottom of the ring structure during the tensile and compression tests to enable deformation of the structures. g,h) force-deflection curves of the different multi-stable structures. g) compression tests h) tensile tests.

During both compression and tensile tests of auxetic structure 3, not all elements retracted or deployed, respectively. It was found that the elements at the sides of the structure deployed first, after which only two of the elements at the top deployed. Finally, three of the four elements at the bottom of the structure switched their configuration. Because the elements at the top of the structure were not connected to the other elements as such that they were forced to deploy, they remained in their retracted configuration during the tensile tests.

Structure 5, which deployed and retracted axially, shows three peaks and valleys in both compression and tensile tests. These peaks represent the least amount of force required to switch from one to another stable configuration of this structure. During the compression tests, first the bottom layer retracted, followed by the second layer and finally the top layer. This order was reversed when the structure deployed.

This study showed that multi-stable structures with different deploying and retracting behavior could be generated based on simple bi-stable elements. It was shown that some of these structures (*e.g.*, structure 5, the ring structure, and auxetic structure 1) are capable of shifting between two distinct configurations (deployed and retracted) with some stable configurations in between.

Retracted implant   Implanted inside the body   Deployed inside the body
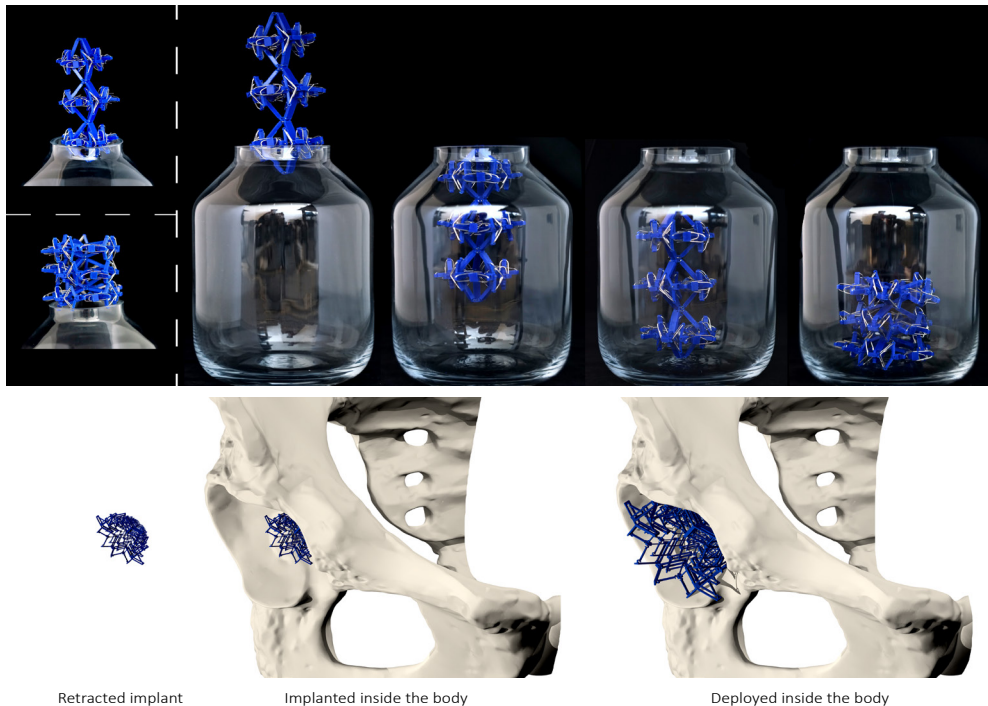
Figure 3. Top: Example of how a multi-stable structure (based on the ring structure) can be put inside a bottle when the deployed configuration does not fit through the opening. Bottom: Example of how multi-stable structures could be applied as bone implant.

In summary, we described the design and manufacturing process of simple bi-stable elements and their assembly into deployable 3D structures. Different parameters of the bi-stable elements affected not only the force required to make the structure shift from one stable position to the other, but could also lead to elements which were not bi-stable at all. Moreover, energy is stored in the bi-stable elements when they are configured in their retracted state. This resulted in lower F_{St} values during deployment as compared to the F_{Sc} values during retraction. The multi-stable structures could be deployed and retracted axially, radially, and behave auxetically. Auxetic structures are especially interesting for application as minimally invasive deployable meta-implants. Due to their small dimensions in all directions in their retracted configuration, the size of the incision and the damage to the surrounding tissues is minimized during surgery. The recovery time of the patient and the chance of pre-operative implant-associated infections are therefore expected to be reduced.

The multi-stable structures presented here need to be further developed before actual clinical application. The high porosity of these deployable structures allows for improved bony ingrowth. As deployable implants use minimum amount of material, a major design challenge is to ensure they provide enough mechanical support. Future research should therefore be focused on evaluating the mechanical performance of meta-implants as well as on designing miniaturized versions that make them more suitable for application as bone substitutes.

References

[1] H.M. Kolken, S. Janbaz, S.M. Leeflang, K. Lietaert, H.H. Weinans, A.A. Zadpoor, Rationally designed meta-implants: a combination of auxetic and conventional meta-biomaterials, Materials Horizons (2017).

[2] S.M. Ahmadi, R. Hedayati, Y. Li, K. Lietaert, N. Tümer, A. Fatemi, C.D. Rans, B. Pouran, H. Weinans, A.A. Zadpoor, Fatigue performance of additively manufactured meta-biomaterials: The effects of topology and material type, Acta Biomaterialia (2017).

[3] F. Bobbert, K. Lietaert, A.A. Eftekhari, B. Pouran, S. Ahmadi, H. Weinans, A. A. Zadpoor, Additively manufactured metallic porous biomaterials based on minimal surfaces: A unique combination of topological, mechanical, and mass transport properties, Acta biomaterialia 53 (2017) 572-584.

[4] A.A. Zadpoor, Design for Additive Bio-Manufacturing: From Patient-Specific Medical Devices to Rationally Designed Meta-Biomaterials, International Journal of Molecular Sciences 18(8) (2017) 1607.

[5] J. Berger, H. Wadley, R. McMeeking, Mechanical metamaterials at the theoretical limit of isotropic elastic stiffness, Nature 543(7646) (2017) 533-537.

[6] C. Coulais, C. Kettenis, M. van Hecke, A characteristic length scale causes anomalous size effects and boundary programmability in mechanical metamaterials, Nature Physics (2017).

[7] R. Hedayati, A. Leeflang, A. Zadpoor, Additively manufactured metallic pentamode meta-materials, Applied Physics Letters 110(9) (2017) 091905.

[8] A.A. Zadpoor, Mechanical meta-materials, Materials Horizons 3(5) (2016) 371-381.

[9] X. Zheng, H. Lee, T.H. Weisgraber, M. Shusteff, J. DeOtte, E.B. Duoss, J.D. Kuntz, M.M. Biener, Q. Ge, J.A. Jackson, Ultralight, ultrastiff mechanical metamaterials, Science 344(6190) (2014) 1373-1377.

[10] T. Bückmann, M. Thiel, M. Kadic, R. Schittny, M. Wegener, An elasto-mechanical unfeelability cloak made of pentamode metamaterials, Nature Communications 5 (2014) 4130.

[11] H. Chen, C. Chan, Acoustic cloaking in three dimensions using acoustic metamaterials, Applied Physics Letters 91(18) (2007) 183518.

[12] L. Fok, M. Ambati, X. Zhang, Acoustic metamaterials, MRS Bulletin 33(10) (2008) 931-934.

[13] S.H. Lee, C.M. Park, Y.M. Seo, Z.G. Wang, C.K. Kim, Acoustic metamaterial with negative modulus, Journal of Physics: Condensed Matter 21(17) (2009) 175704.

[14] A. Crivaro, R. Sheridan, M. Frecker, T.W. Simpson, P. Von Lockette, Bi-stable compliant mechanism using magneto active elastomer actuation, Journal of Intelligent Material Systems and Structures 27(15) (2016) 2049-2061.

[15] J.L. Silverberg, J.-H. Na, A.A. Evans, B. Liu, T.C. Hull, C.D. Santangelo, R.J. Lang, R.C. Hayward, I. Cohen, Origami structures with a critical transition to bistability arising from hidden degrees of freedom, Nature Materials 14(4) (2015) 389-393.

[16] H. Yasuda, J. Yang, Reentrant origami-based metamaterials with negative Poisson's ratio and bistability, Physical Review Letters 114(18) (2015) 185502.

[17] R.L. Harne, Z. Wu, K.-W. Wang, Designing and harnessing the metastable states of a modular Metastructure for programmable mechanical properties adaptation, Journal of Mechanical Design 138(2) (2016) 021402.

[18] S. Sengupta, S. Li, Multi-stability and variable stiffness of cellular solids designed based on origami patterns, SPIE Smart Structures and Materials+ Nondestructive Evaluation and Health Monitoring, International Society for Optics and Photonics, 2017, pp. 1016426-1016426-10.

[19] S. Waitukaitis, R. Menaut, B.G.-g. Chen, M. van Hecke, Origami multistability: From single vertices

to metasheets, Physical Review Letters 114(5) (2015) 055503.

[20] K. Bertoldi, V. Vitelli, J. Christensen, M. van Hecke, Flexible mechanical metamaterials, Nature Reviews Materials 2 (2017) natrevmats201766.

[21] M. Ohsaki, S. Nishiwaki, Shape design of pin-jointed multi-stable compliant mechanisms using snapthrough behavior, Structural and Multidisciplinary Optimization 30(4) (2005) 327-334.

[22] B.D. Jensen, M.B. Parkinson, K. Kurabayashi, L.L. Howell, M.S. Baker, Design optimization of a fully-compliant bi-stable micro-mechanism, Ann Arbor MI 48109 (2001) 2125.

[23] Y.S. Oh, S. Kota, Synthesis of multi-stable equilibrium compliant mechanisms using combinations of bi-stable mechanisms, Journal of Mechanical Design 131(2) (2009) 021002.

[24] M. Santer, S. Pellegrino, Compliant multi-stable structural elements, International Journal of Solids and Structures 45(24) (2008) 6190-6204.

[25] M. Santer, S. Pellegrino, Concept and design of a multi-stable plate structure, Journal of Mechanical Design 133(8) (2011) 081001.

[26] G. Chen, Q.T. Aten, S. Zirbel, B.D. Jensen, L.L. Howell, A tristable mechanism configuration employing orthogonal compliant mechanisms, Journal of Mechanisms and Robotics 2(1) (2010) 014501.

[27] J. Zhang, C. Zhang, L. Hao, R. Nie, J. Qiu, Exploiting the instability of smart structure for reconfiguration, Applied Physics Letters 111(6) (2017) 064102.

[28] D. Restrepo, N.D. Mankame, P.D. Zavattieri, Phase transforming cellular materials, Extreme Mechanics Letters 4 (2015) 52-60.

[29] T. Chen, J. Mueller, K. Shea, Integrated Design and Simulation of Tunable, Multi-State Structures Fabricated Monolithically with Multi-Material 3D Printing, Scientific Reports 7 (2017).

[30] Y. Gerson, S. Krylov, B. Ilic, D. Schreiber, Design considerations of a large-displacement multi-stable micro actuator with serially connected bi-stable elements, Finite Elements in Analysis and Design 49(1) (2012) 58-69.

[31] S. Shan, S.H. Kang, J.R. Raney, P. Wang, L. Fang, F. Candido, J.A. Lewis, K. Bertoldi, Multi-stable architected materials for trapping elastic strain energy, Advanced Materials 27(29) (2015) 4296-4301.

[32] Z. Wu, R.L. Harne, K.-W. Wang, Energy harvester synthesis via coupled linear-bi-stable system with multi-stable dynamics, Journal of Applied Mechanics 81(6) (2014) 061005.

[33] A. Arrieta, P. Hagedorn, A. Erturk, D. Inman, A piezoelectric bi-stable plate for nonlinear broadband energy harvesting, Applied Physics Letters 97(10) (2010) 104102.

[34] K. Kuribayashi, K. Tsuchiya, Z. You, D. Tomus, M. Umemoto, T. Ito, M. Sasaki, Self-deployable origami stent grafts as a biomedical application of Ni-rich TiNi shape memory alloy foil, Materials Science and Engineering: A 419(1-2) (2006) 131-137.

[35] A.A. Zadpoor, J. Malda, Additive manufacturing of biomaterials, tissues, and organs, Annals of Biomedical Engineering 45(1) (2017) 1-11.

[36] Y. Ramot, M. Haim-Zada, A.J. Domb, A. Nyska, Biocompatibility and safety of PLA and its copolymers, Advanced drug delivery reviews 107 (2016) 153-162.

[37] R. Kulkarni, K. Pani, C. Neuman, F. Leonard, Polylactic acid for surgical implants, WALTER REED ARMY MEDICAL CENTER WASHINGTON DC ARMY MEDICAL BIOMECHANICAL RESEARCH LAB, 1966.

[38] B. Gupta, N. Revagade, J. Hilborn, Poly (lactic acid) fiber: an overview, Progress in polymer science 32(4) (2007) 455-482.

[39] S. Palathingal, G. Ananthasuresh, Design of bi-stable arches by determining critical points in the force-displacement characteristic, Mechanism and Machine Theory 117 (2017) 175-188.

6

Deployable structures folded from a flat state

Deployable meta-implants aim to minimize the invasiveness of orthopedic surgeries by allowing for changes in their shape and size that are triggered by an external stimulus. Multi-stability enables deployable implants to transform their shape from some compact retracted state to the deployed state where they take their full sizes and are load-bearing. We combined multiple design features to develop a new generation of deployable orthopedic implants. Kirigami cut patterns were used to create bi-stability in flat sheets which can be folded into deployable implants using origami techniques. Inspired by Russian dolls, we designed multi-layered specimens that allow for adjusting the mechanical properties and the geometrical features of the implants through the number of the layers. Because all layers are folded from a flat state, surface-related functionalities could be applied to our deployable implants. We fabricated specimens from polylactic acid, titanium sheets, and aluminum sheets, and demonstrated that a deployment ratio of up to ≈2 is possible. We performed experiments to characterize the deployment and load-bearing behavior of the specimens and found that the above-mentioned design variables allow for adjustments in the deployment force and the maximum force before failure. Finally, we demonstrate the possibility of decorating the specimens with micro-patterns.

6.1 Introduction

It is often said that in biological tissues such as bone, "form follows function" [1, 2]. It should, thus, come as no surprise that in orthopedic implants that replace the human bone either temporarily or permanently, 'function follows form'. This short statement summarizes the underlying principle of the so-called "meta-biomaterials" [3] and "meta-implants" [4, 5], where the geometrical design at various scales is used to develop unprecedented functionalities.

This novel approach, whose success depends on the feasibility of fabricating complex geometries at different scales, owes its emergence to the recent advances in additive manufacturing (AM, = 3D printing) techniques. Thanks to the "form-freedom" [6-8] and "batch-size-indifference" of AM techniques [7], the problem of developing implants with advanced functionalities reduces to the problem of geometrically designing them using the "rational design" principles [3, 9].

At the microscale, the application of the rational design principles has resulted in meta-biomaterials that exhibit, for example, improved bone-implant interaction realized through the incorporation of auxetic meta-biomaterials [4] or a remarkably high level of bone-mimicry [10-12]. These uncommon properties could then be exploited to design novel meta-implants with improved bone-implant contact and, thus, enhanced longevity [4].

At the macro-scale, the fusion of geometrical design, advanced AM techniques, and rational design principles has recently enabled the development of a new category of orthopedic implants known as "deployable implants" [5]. The shape and mechanical properties of such implants can be changed upon the application of a triggering mechanism that transforms the implant from its compact, retracted state to a fully deployed, load-bearing state. The initially compact shape of the implant ensures that the performed surgery is as minimally invasive as possible. One of the applications of such implants is to repair vertebral compression fractures. Currently, vertebroplasty (VB) and balloon kyphoplasty (BKP) are used to treat such fractures with minimal invasiveness. While VB only stabilizes the fracture by the injection of bone cement [13], BKP is a technique in which a balloon catheter is inserted and inflated prior to the injection of bone cement in order to restore the height of the vertebra [13-16]. To improve the vertebral height restoration achieved with BKP, another technique is proposed, namely vertebral body stenting (VBS) [17]. This technique uses a stent mounted on the balloon catheter that expands upon the inflation of the balloon. The expanded stent keeps the created cavity open after the balloon is removed to let the bone cement fill the cavity [13]. Although these treatments result in pain relief for the patient, cement does not allow for bony ingrowth [18]. Moreover, cement leakage as well as other complications such as persisting pain and the fracture of adjacent vertebrae may occur [19]. Our deployable implants, on the other hand, are porous devices that are deployed like the stent in VBS but do not require cement, and, thus, allow for bony ingrowth (Figure 1a).

The underlying shape-shifting mechanism used in the design of the first generation of our deployable meta-implants [5] was the concept of "multi-stability" [20, 21] where the implant is designed to have two or more stable states. By transitioning from one stable state to another, the shape and mechanical properties of the implant can change. Our first generation of deployable implants introduced the concept of deployability in orthopedic implants and demonstrated the possibility of fabricating functional prototypes using widely available techniques. However, they were limited in two major aspects. First, they required individual printing and manual assembly of many multi-stable mechanisms. Second, due to their 3D geometry they did not allow for the incorporation of surface-related functionalities such as surface nanopatterns [22, 23].

Here, we present a new generation of deployable implants that not only address those limitations but also offer some additional advantages. We used origami-based designs to fold *multi-layered* deployable implants from a flat state. The use of multiple layers is inspired by Russian dolls (Matryoshka) where identically shaped dolls that gradually increase in size successively encapsulate one another (Figure 1b). Similar concepts can also be observed in nature (Figure 1c). Given that each layer is folded from a flat state [24, 25], advanced nanopatterning techniques that are only applicable to flat surfaces (*e.g.*, electron beam lithography [26, 27], reactive ion etching (RIE) [28, 29] and electron beam induced deposition

Figure 1. a) The novel concept of deployable implants as applied to the treatment of a fractured vertebra. With minimally invasive surgery, a deployable structure including a balloon is placed inside the fractured vertebra. Upon the inflation of the balloon, the deployable structure expands and restores the height of the vertebra. The balloon is then removed. b) Russian dolls shown from the front and top views. c) Red onion also consists of different layers.

[22]) could be used to simultaneously stimulate the osteogenic differentiation of stem cells [30, 31] and kill bacteria [28, 32].

6.2 Materials and methods

6.2.1 Design

We used the concept of bi-stability to design deployable flat panels. Kirigami cut patterns are known to introduce bi-stability into flat materials [33, 34]. This approach to design bi-stable mechanisms is compatible with our ultimate goal of creating foldable multi-layer implants. The flat panels were then arranged in such a way to create three-dimensional cubes with varying sizes (Figure 2c,d). Towards that end, two connection sites were designed at every corner to enable the spatial arrangement of the panels (Figure 2a). Each panel of the unscaled (100%) cube consisted of four bi-stable elements with two perpendicular rigid elements of 15 mm length and a rigid beam with a length of 10 mm and width of 3 mm to enable the shape transformation of the bi-stable elements (Figure 2a).

To create the desired foldable cubes, six of the panels described above were arranged according to the unfolded shape of a cube (Figure 2e). Two scaled versions of these unfolded states (by 30% and 40%) were also fabricated (Figure 2b, e). In addition to the unfolded cube patterns with deployed bi-stable elements, an unfolded cube with retracted bi-stable elements was designed by cutting the deployed geometry of one deployable element at the rotation points of its hinges. The deployed element was then moved towards its retracted state (Figure 2a). By assembling four of these elements into a rectangular panel, the unfolded pattern of a cube comprising six retracted panels was created. This cube pattern was then scaled by 20%, 30%, and 40% (Figure 2b).

6.2.2 Manufacturing

6.2.2.1 PLA specimens (control group)

To evaluate the advantages of the origami approach, we fabricated similar designs using the same methodology as was used in the first generation of our deployable implants (*i.e.*, 3D printing and manual assembly). These specimens are, therefore, considered our control specimens against which the performance of our origami designs is evaluated.

The design of one panel (100%) was prepared and scaled (to 80% and 60%) in Cura (Ultimaker, The Netherlands) to prepare the files for a fused deposition modeling (FDM) 3D printer (Ultimaker 2+, Ultimaker, The Netherlands). A 0.25 mm nozzle was used to print the panels from polylactic acid (PLA) filaments. Six panels for every cube were printed. For the three different panel sizes (*i.e.*, 100%, 80%, and 60%), three different panel thicknesses were designed (*i.e.*, 2 mm, 1.5 mm, 1 mm).
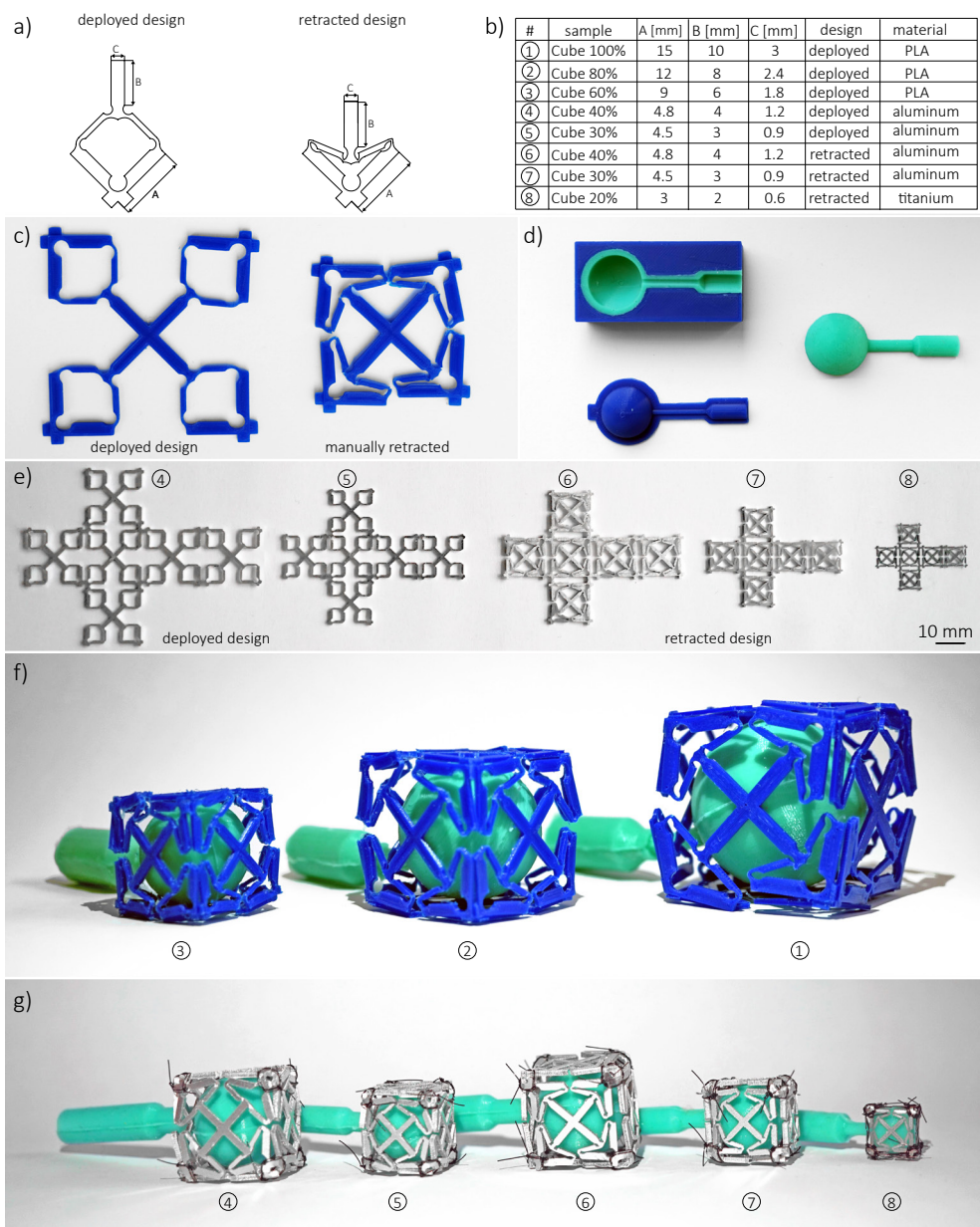
Figure 2. a) The parameters of the deployed and retracted designs. b) The dimensions of one corner of all specimens c) 1. 3D printed panels in their deployed configuration. 2. Manually shifted panels in their retracted configuration. d) The molding of silicon balloons. e) Laser-cut aluminum (scaling = 40% and 30%, both deployed and retracted conditions) and titanium (scaling = 20%, retracted) specimens. f) Balloons positioned inside the retracted control specimens. g) Balloons positioned inside the retracted origami-based specimens. From left to right: Manually retracted aluminum specimens (scaling = 40% and 30%, deployed), aluminum specimens (scaling = 40%, 30%, retracted), and a titanium specimen (scaling = 20%, retracted).

6.2.2.2   Origami-based designs

In order to cut the specimens from metal sheets, the drawings of the unfolded cube patterns were saved as DXF files. These files were then used to laser-cut aluminum sheets (1050A) and titanium foils (purity 99.6+%, annealed; Goodfellow) with respective thicknesses of 1 mm and 0.125 mm. Three specimens of both deployed and retracted designs (scaling = 40% and 30%) were cut from aluminum sheets (12 specimens in total) using a Lion 900 laser cutter (Lion Laser Systems BV, The Netherlands). The three specimens of the retracted design (scaling = 20%) were cut from the titanium foil (3 specimens in total) using laser micromachining (Optec Laser Systems, Belgium).

6.2.3   Assembly of cubes

6.2.3.1   PLA specimens (control group)

Before the panels with bi-stable elements were assembled, the bi-stable elements were brought to their retracted configurations (Figure 2c). The panels were then assembled into a cube by gluing the connection sites at the corners to the sides of the adjacent panels.

6.2.3.2   Origami-based designs

Similar to the PLA specimens, the unfolded origami specimens with a deployed design were brought to their retracted configurations. All unfolded sheets were then folded into cubes. The corners of the cubes were connected to each other with polyamide threads to hold the specimens together during the deployment process.

6.2.4   Balloons

Silicone balloons were manufactured in order to deploy the retracted structures (Figure 2d). First, the molds were designed and printed using an FDM 3D printer (Ultimaker2+, Ultimaker, The Netherlands) and a 0.4 mm nozzle. The molds were then filled with silicone (Vinylpolysiloxane Elite Double 22, Zhermack, Italy). The inner parts of the molds were removed when the silicone was cured. Silicone was then used to connect both halves of the balloons. Since there were six different sizes of the cubes, namely control specimens (scaling = 100%, 80%, and 60%), aluminum specimens (scaling = 40% and 30%), and titanium specimens (scaling = 20%), six sizes of balloons were fabricated. The wall thickness of the balloons varied for the different sizes (2 mm for the three large balloons and 1 mm for the three smaller balloons).

    The balloons were inflated using a 6 L air compressor (Michelin, France) and the required pressure was measured using the integrated pressure gauge (accuracy = 0.5 bar). The pressure was slowly increased from 0 bar to the value required to deploy the structures (Table 1).

6.2.5 The Russian doll (Matryoshka) principle

The Russian doll principle (Figure 1b) was used to enhance the structural integrity of the designed deployable structures. By inserting a small cube inside a larger one, the smaller cube deploys upon the inflation of the balloon up to the point that it comes into contact with the larger one, thereby deploying it. Two versions of the Russian doll implants with two (scaling factor of the layers = 30% and 40%) and three (scaling factor of the layers = 30%, 40%, and 50%) aluminum layers were designed, laser cut, and folded (Figure 5a, b).

6.2.6 Change in dimensions between the deployed and retracted structure

A caliper was used to determine the dimensions of the specimens in their retracted and deployed states. The change in the dimensions of the specimens between both configurations was determined as:

$$change\ in\ dimensions\ [\%] = \frac{dimensions\ deployed\ structure\ [mm]}{dimensions\ retracted\ structure\ [mm]} \times 100$$

6.2.7 Mechanical tests

The mechanical properties of the different designs were determined using compression tests. Before the mechanical tests were performed, the balloons were removed from the deployed structures. The specimens were uniaxially compressed using a Lloyd LR5K mechanical testing machine at a crosshead velocity of 1 mm/min. Two load cells (5 kN and 100 N) were used depending on the expected range of the forces to compress the control specimens and the aluminum specimens. In the case of the single-layer specimens, the tests were aborted when either a 50 N force was reached or when the specimens were compressed to 60% of their deployed size. For the Russian doll specimens, the specimens were allowed to experience higher forces. For the compression of the titanium structures, a velocity of 0.5 mm/min and a 5 N load cell were used. These tests were aborted when a maximum force of 4.95 N was reached to prevent damage to the load cell. In order to evaluate the effects of friction at the interface of the compression plates and the control specimens, sandpaper (P80) was used for the compression of the control specimens (scaling = 80%) (*i.e.*, PLA cubes) with a thickness of 1.5 mm. These specimens were chosen because they were the least fragile during the manual retraction of the bi-stable elements and the deployment of the specimens.

6.2.8 Micropatterns

Micropatterns were created on a titanium specimen to demonstrate the concept of patterning a flat sheet and folding it afterwards. The patterns included circles and squares with a diameter and edge lengths of 65 µm, respectively. The wavy pattern consisted of waves with a length of 5 mm and an amplitude of 0.25 mm. These micropatterns were engraved into a

titanium foil through laser micromachining (Optec Laser Systems, Belgium). To engrave the sheet, the laser frequency (50 kHz) and current (3.8 A) were kept constant, while the firing rate (30 kHz, 50 kHz and 70 kHz) and the number of repetitions (n = 2, n = 10, n = 20, n = 30, n = 40) were varied. After engraving, the specimen was cleaned with demineralized water and detergent in an ultrasonic bath for 10 minutes followed by rinsing with demineralized water in the ultrasonic bath for another 5 minutes. A Keyence VH-Z250R (Keyence, Japan) digital microscope was used to determine the depth, diameter, and width of the micropatterns.

6.3 Results

6.3.1 Inflation of balloons and mechanical tests

6.3.1.1 PLA specimens (control group)

The deployment of a cube was considered successful when it deployed without any fractures. Out of a total of 43 control specimens (*i.e.*, PLA cubes), 16 cubes were successfully deployed. Some of the partially damaged cubes were still measurable with either one fracture (7 cubes), two fractures (2 cubes), or with more than two fractures (2 cubes). For the control specimens that fractured during inflation, one replacement cube was manufactured in order to be able to test more than one specimen under compression. For the control specimens (scaling = 60%) with a thickness of 1.5 mm, three replacement cubes were made of which only one could be used for the compression tests. The control specimens (scaling = 80%) with a thickness of 1.5 mm were all successfully deployed (Figure 3a).

The smallest change in the dimensions was observed for the control specimens (scaling = 60%) with a thickness of 2 mm. The maximum pressure required to deploy the different control specimens varied between 0.1-0.5 bar. The control specimens (scaling = 60%) required the highest pressure while the unscaled control specimens (100% cube) required the lowest pressure (Table 1).

6.3.1.2 Origami-based designs

All origami-based specimens with a single layer were successfully deployed (Figure 4a). Signs of fractures were only observed in the smallest cube of the multi-layer Russian doll specimens. As expected, the smallest cube was deployed first until it was in contact with the medium-sized cube. Upon further inflation of the balloon, both cubes deployed together until deployment was restricted by the maximum deployment of the smallest cube. To complete the deployment of the third cube, we needed to use another balloon to continue the inflation process. When comparing the changes in the configuration between the different specimens, the origami-based designs showed a larger change in the dimensions as compared to the control group (Table 1). The titanium specimens showed the best results with a change of 179% (Table 1).

The aluminum specimens (scaling = 30% and 40%) required ≈1.2-2 bar to deploy. The more complex Russian doll specimens with two or three layers of cubes required a higher pressure than all other specimens (Table 1). The Russian doll specimens with three layers could not be deployed with a single balloon due to the rupture of the balloon at ≈3.5 bar. A larger balloon to inflate the origami-based specimens (scaling = 40%) was inserted and could deploy the last part of the specimen. The titanium specimens could be deployed with a pressure of ≈1.5 bar.

	Dimensions of configuration [mm]		Thickness [mm]	Change in dimensions [%]	Material	Maximum pressure [bar]
	Retracted	Deployed				
Cube 100% deployed	37.8 ± 0.5	46.1 ± 1.9	1	124 ± 7.5 (4~)	PLA	≈ 0.1
	37.2 ± 0.6	48.7 ± 1.7	1.5	131 ± 9.0 (2+1~)	PLA	≈ 0.1
	38.2 ± 0.3	51 ± 1.5	2	133 ± 5.6 (4~)	PLA	≈ 0.1
Cube 80% deployed	30.6 ± 0.3	37.1±0.7	1	121 ± 3.5 (3+1~)	PLA	≈ 0.2
	31.2 ± 0.2	39.9 ± 0.6	1.5	128 ± 2.3 (3)	PLA	≈ 0.2
	31.0 ± 0.3	40.5± 0.3	2	130 ± 1.5 (1+1~)	PLA	≈ 0.2
Cube 60% deployed	23.5 ± 0.2	30.8 ± 1.0	1	129 ± 4.6 (3+1~)	PLA	≈ 0.5
	24.1 ± 0.4	30.4 ± 0.2	1.5	124 ± 4.4 (1+1~)	PLA	≈ 0.5
	24.7 ± 0.1	29.8 ± 0.3	2	119 ± 4.5 (2)	PLA	≈ 0.5
Cube 40% deployed	17.5 ± 0.1	28 ± 0.3	1	164 ± 7.6 (3)	Aluminum	≈ 1.5
Cube 30% deployed	13.5 ± 0.1	22.4 ± 1.1	1	166 ± 9.0 (3)	Aluminum	≈ 2
Cube 40% retracted	17.0 ± 0.1	29.5 ± 1.2	1	173 ± 6.1 (3)	Aluminum	≈ 1.2
Cube 30% retracted	13.2 ± 0.2	20.8 ± 0.2	1	158 ± 7.5 (3)	Aluminum	≈ 1.4
Cube 20% retracted	7.7 ± 0.1	13.8 ± 0.5	0.125	179 ± 7.2 (3)	Titanium	≈ 1.5
Russian doll specimen, two layers	17.0 ± 0.3	26.7 ± 1.7	2	157 ± 10.8 (3~)	Aluminum	≈ 2.5
Russian doll specimen, three layers	20.5 ± 0.1	27.1 ± 0.5	3	132 ± 2.7 (1+2~)	Aluminum	≈ 3.5

Table 1. The dimensions of the retracted and deployed specimens with their thickness, volume change, and the type of the material. The numbers between round brackets indicate the number of the intact specimens and the number followed by ~ is the number of the specimens with fractured parts. Example: (1+2~) means that the dimensions were measured from one intact specimen and two specimens with fractures.

6.3.2 Mechanical tests

6.3.2.1 PLA specimens (control group)

The control specimens which included less than three fractures after inflation were compressed with 1 mm/min using a Lloyd LR5K testing machine. During the tests, the deployable elements slowly retracted (Figure 3b). As expected, the cubes with thicker planes required more force to be compressed (Figure 3d). The force-displacement curves of the specimens that neatly retracted without out-of-plane deformations showed a steep slope at their end phases (Figure 3d). The curves of the specimens with a thickness of 1 mm were relatively smooth as compared to those of thicker specimens (Figure 3d).

When sandpaper was applied to the top and bottom of the control specimens (scaling = 80%) with a thickness of 1.5 mm, no retraction of the panels at the top and bottom was observed (Figure 3c). However, fracture and out-of-plane deformation of the vertical panels were observed (Figure 3c). The force-displacement graph shows that the same force is
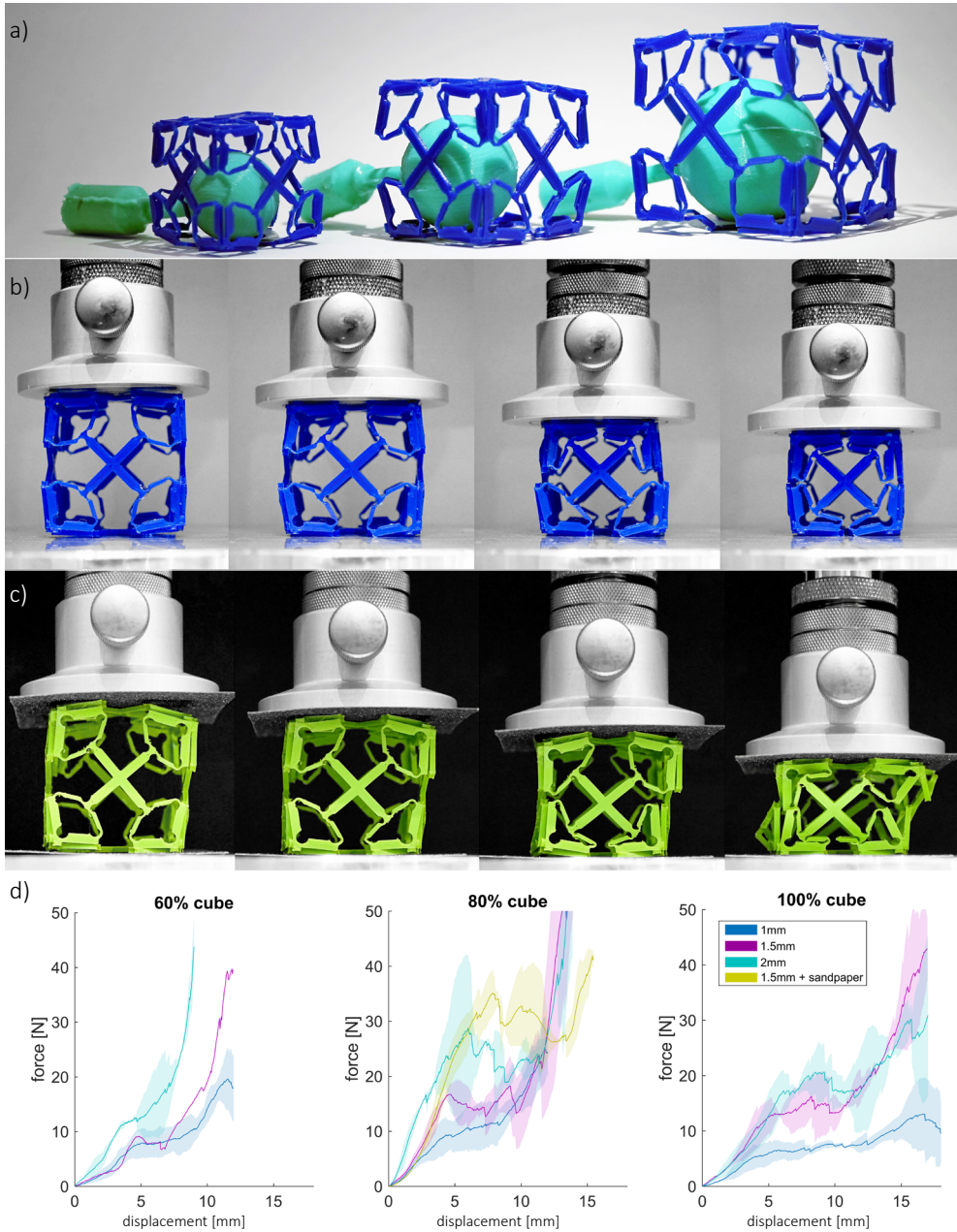
Figure 3. PLA specimens (control group). a) Deployed control specimens (scaling = 60%, 80%, 100%). b) The compressive behavior of a control specimen (scaling = 80%, thickness = 1.5mm). c) The compressive behavior of a control specimen with sandpaper (scaling = 80%, thickness = 1.5mm). d) The force-displacement curves of the control specimens (scaling = 60%, 80%, and 100%).

required to deform the control specimens (scaling = 80%) with a thickness of 1.5 mm with and without sandpaper up to 4 mm (Figure 3d). The difference is visible after this point, where the force still increases for a specimen with sandpaper and slightly decreases for the same specimen compressed without sandpaper (Figure 3d).

6.3.2.2   Origami-based designs

All single-layer specimens developed a spherical shape thanks to the forces transmitted from the balloon to the cubic specimens (Figure 4a). The multi-layer Russian doll specimens also developed a spherical shape, although to a lesser extent than the single-layer specimens (Figure 5c). While one of the three multi-layer specimens deployed fully symmetrically, the outer layer of the two other specimens contained one or two retracted planes. As opposed to the control specimens, the origami-based specimens did not return to their retracted configuration during the compression tests. Instead, they flattened into disc-like shapes without retracted elements (Figure 4c). For the 30% and 40% specimens, initially more force was required to compress these specimens as compared to their retracted counterparts (Figure 4c). For all origami-based specimens, initially more compression force was required to deform the specimens as compared to the control specimens (Figure 3d, 4d). The titanium specimens showed the least variation in the measured forces and required the least amount of force to be compressed (Figure 4d).

When comparing the force-displacement curves of the two-layer Russian doll specimens with those of the single-layer aluminum (scaling = 30% and 40%) specimens, we found that their initial stiffness is comparable up to 1 mm of displacement (Figure 5e). However, after this point, more force is required to compress the Russian doll specimens, as compared to the single-layer specimens (Figure 5e). The three-layer Russian doll specimens required the most compression force of all specimens in this study (Figure 5e).

6.3.3   Micropatterns

The designed micropatterns were successfully engraved onto the surface of the specimen (Figure 6, top inset). By keeping the frequency and current of the laser constant but varying the firing rates and the number of repetitions, different depths and quality of the shapes could be achieved. The squares and circles engraved with a firing rate of 70 kHz and 10 repetitions yielded in the most accurate micropatterns in terms of their similarity to the designs. The depth of the patterns depended on the combinations of firing rate and the number of repetitions. A higher number of repetitions resulted in a deeper engraving on the titanium foil. The depth of the micropatterns varied between 2 μm for the wave pattern to 60 μm for the circles.
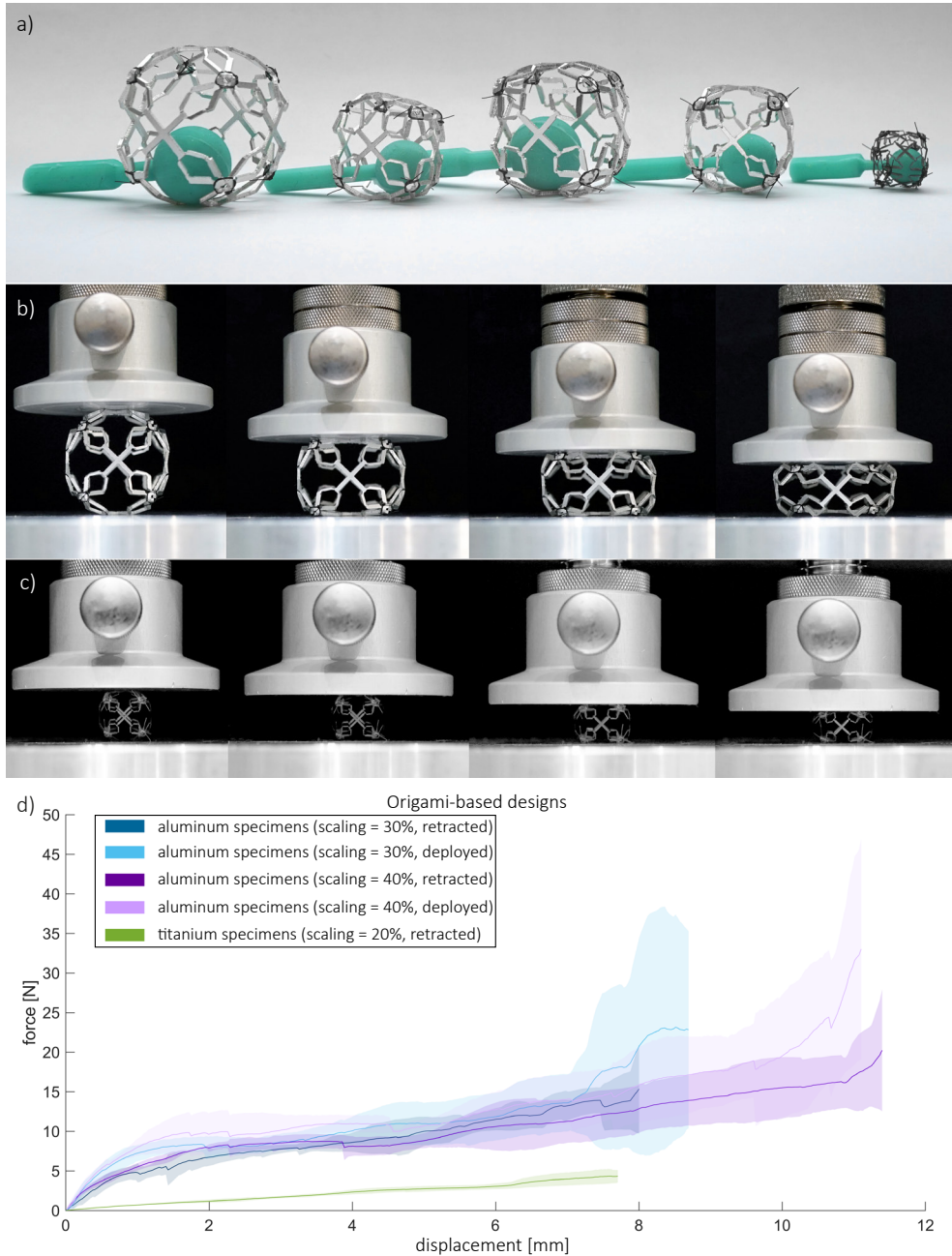
Figure 4. Origami-based design. a) Deployed origami-based specimens. Two deployed aluminum specimens (scaling = 40% and 30%), two retracted aluminum specimens (scaling = 40% and 30%), and a retracted titanium specimen (scaling = 20%). b) The compression of an aluminum specimen. c) The compression of a titanium specimen. d) The force-displacement curves of the origami-based specimens.

6.4 Discussion

We showed, for the first time ever, how the principles of multi-stability, kirigami, and origami could be combined to create deployable meta-implants with precisely controlled and arbitrarily complex surface patterns. The deployment of the designed meta-implants can be easily performed using inflating balloons. A similar balloon-based inflation procedure is already applied as a part of a procedure used to treat vertebral compression fractures minimally invasively, namely balloon kyphoplasty (BKP). Our designs could provide a potential replacement for the stents used in vertebral body stenting (VBS) [35-37], which is a proposed alternative for BKP. This shows the feasibility of our approach and could facilitate the clinical adoption of such implants.
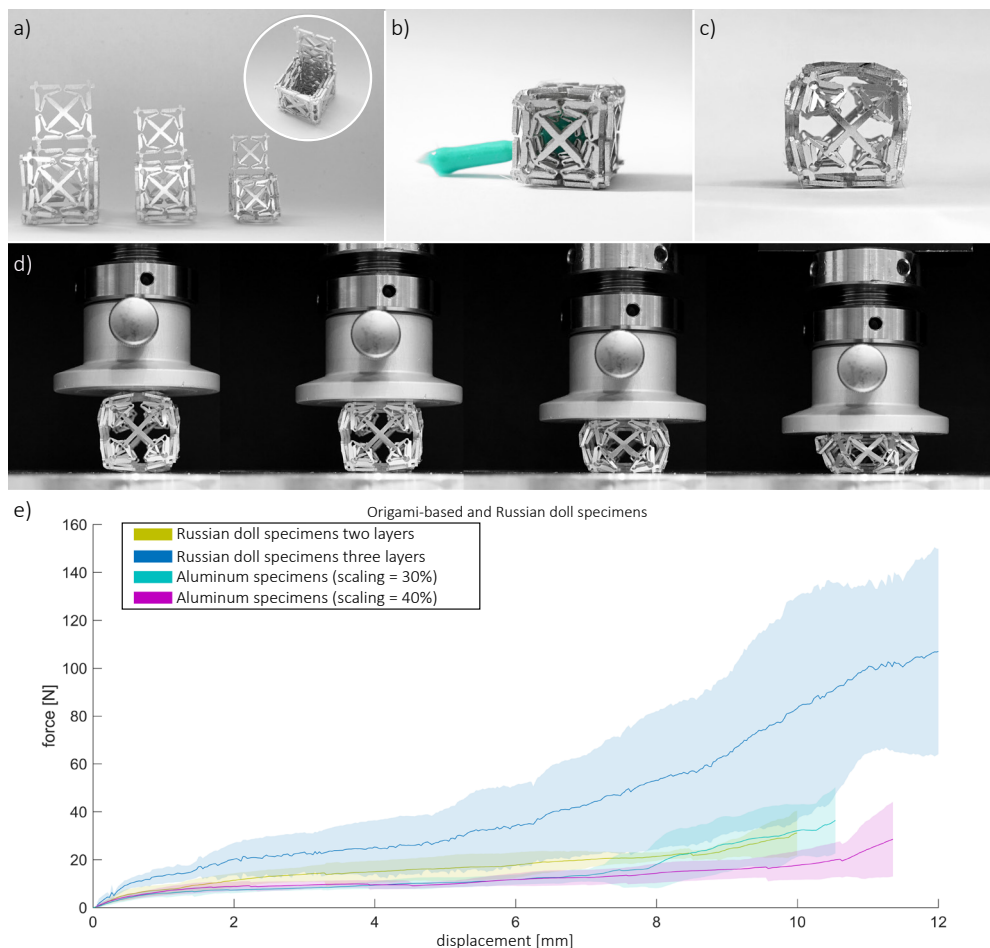

Figure 5. The Russian doll principle. a) Three aluminum cubes are shown from the front view and a top view of a small cube within two larger cubes. b) Retracted Russian doll specimens with three layers (scaling factor of the layers = 30%, 40%, and 50%, aluminum). c) A multi-layer Russian doll specimen with three layers shown after deployment. d) The compression of a Russian doll specimen with three layers. e) The force-displacement curves of the Russian doll specimens and the aluminum specimens (scaling = 30%, 40%).

6.4.1   Deployability

The results of our study clearly show the superior performance of origami-based designs over the control specimens, which were designed and manufactured using the principles introduced in our previous generation of deployable meta-implants. This superior performance is clear in terms of the successful deployment of the meta-implant specimens, the ease of manufacturing, the possibility to incorporate surface nanopatterns and other surface related bio-functionalities, and the mechanical properties.

The design and fabrication of basic elements that exhibit a reliable bi-stable behavior is one of the major challenges in the design of deployable meta-implants. In this study, the use of kirigami as the mechanism through which bi-stability was created enabled us to fold the meta-implants from a flat state using origami principles. This is one of the areas of application where both kirigami and origami principles are required and each play a different role.

In terms of the deployment ratio, the origami-based designs achieved up to ≈2 times larger dimensions after deployment. Given the fact that the volume of the implant has a cubic relationship with the dimensions of the specimens, a two-fold increase in dimensions translates into an eight-fold decrease in the initial volume of the implant and, thus, drastically reduces the invasiveness of the surgery. The design and dimensions of the kirigami cut patterns could be used to adjust the deployment ratio. Studying the design of the kirigami patterns is, therefore, a systematic way for the study of the multi-stability behavior of the implants and provides a general design platform within which deployable meta-implants could be "rationally designed" using predictive computational models.

The origami-based specimens developed a sphere-like shape after deployment. This was due to the fact that the balloon used for their deployment was spherical. Such a rounded shape may be desirable in cases where the sharp edges of the cubic specimens is not compatible with the anatomical shapes that are being operated on. It is, of course, also possible to chamfer the cubic specimens at the design stage.

This change in the shape of the implant after deployment goes far beyond the above-mentioned rounding effect and showcases an interesting and important property of our origami-based meta-implants, namely their shape-morphing behavior. In practice, there are also external boundaries (*i.e.*, bony contours) that define the ultimate shape of the deployed meta-implant. The origami-based designs could, therefore, match the shape of their external boundaries. This eliminates the need for designing implants that match a specific (patient-specific) shape and enables us to use the same (generic) implant for different patients.

6.4.2   Mechanical performance

There are several novel design features in the work presented here that could be used to address the structural challenges faced when designing deployable meta-implants. The Russian doll concept is a particularly interesting approach, because it allows for a high level

of adjustability in terms of the mechanical properties of the meta-implant as well as its dimensions. Each additional layer results in a multi-fold increase in the force corresponding to the same displacement (Figure 5). Simply adding an additional layer could, therefore, be used to reinforce the implant further for the cases where higher forces are expected (*e.g.*, adult, obese patients) while a smaller number of layers could be used in other cases (*e.g.*, pediatric patients) to be able to strike a balance between the requirement to provide enough structural performance and the risk of causing stress shielding. The porous structure of the implant also allows for other types of reinforcing mechanisms to be used for improving the mechanical properties of the meta-implants further. For example, deploying wire-like objects that coil within a confined space (similar to [38]) could drastically increase the mechanical properties of the implant. Furthermore, given the fact that porous structures allow for bony ingrowth, the mechanical properties of the implant are expected to gradually increase with the progress of the bone tissue regeneration.

A previous study has shown that the quasi-static and fatigue mechanical properties of porous structures could increase by up to 7 folds upon bony ingrowth [39]. Moreover, the choice of the material could be used to further increase the mechanical properties of the implant. In this study, we used sheets that were made from pure titanium and aluminum, which are highly deformable but whose mechanical properties are several times lower than other titanium alloys that could be used for the fabrication of orthopedic implants (*e.g.*, Ti-6Al-4V). Finally, the sheet thickness could be used to adjust the mechanical properties of the meta-implants. It is, however, worth noting that the bendability of metal sheets decreases with the thickness. In summary, there are several design strategies that allow for the adjustment of the mechanical properties of the meta-implants developed here and could be used in the future studies to tailor the mechanical properties of deployable implants to the specific problem at hand. Many aspects of such types of implants including their behavior under dynamic loading conditions also need to be studied before they could be used in clinical practice.

6.4.3   Surface nanopatterns and other bio-functionalities

The fact that our origami-based designs are folded from a flat state makes it possible to use surface nanopatterning techniques that usually only work on flat surfaces [40]. We used laser micromachining to create some micropatterns in this study that were applied on our deployable meta-implants. It is, however, possible to use virtually any type of micro-/nanopatterning technique including the ones we have applied in our other studies to titanium and other biomedically relevant materials (Figure 5). With techniques such as electron beam induced deposition (EBID, a nanoscale 3D printing technique) [22, 32], electron beam nanolithography [26, 27], and reactive ion etching (RIE) [28, 41], it is possible to create any design of surface nanopatterns at scales ranging between a few nanometers (in the case of EBID) to hundreds of nanometers (nanolithography, RIE).

A growing body of recent research shows that surface nanopatterns could be used to both determine stem cell fate [42-44] and prevent implant-associated infections [27, 32]. In both cases, the primary action mechanism is mechanical in nature. Regarding the stem cell fate, surface nanopatterns result in cytoskeletal re-arrangement, regulate focal adhesions, and may upregulate the expression of osteogenic markers [45]. This kind of mechanobiological pathways does not require any pharmaceutical agent, meaning that it is less expensive and safer to implement in clinical practice. Moreover, the certification of medical devices that do not incorporate pharmaceutics is more streamlined as compared to those that incorporate one or more active agents.

In the case of bacteria, a mechanical mechanism where the asperities of the nanopattern strain the cell wall of bacteria and cause them to rupture is often cited as the mechanism through which surface nanopatterns kill bacteria [27, 32, 46]. Similar to the case of stem cells, this is a drug-less approach whose success is not dependent on the potency of any specific drug, making it easier for medical devices to be certified for clinical use. Even more importantly, antibiotic resistance is not a problem in the case of surface nanopatterns, meaning that even multi-drug resistant bacteria could be killed using this approach.

It is important to realize that the bio-functionality of the deployable meta-implants presented here is also dependent on the design of the kirigami cut patterns, the thickness of the metal sheets used for creating the different layers of the implants, and the number of
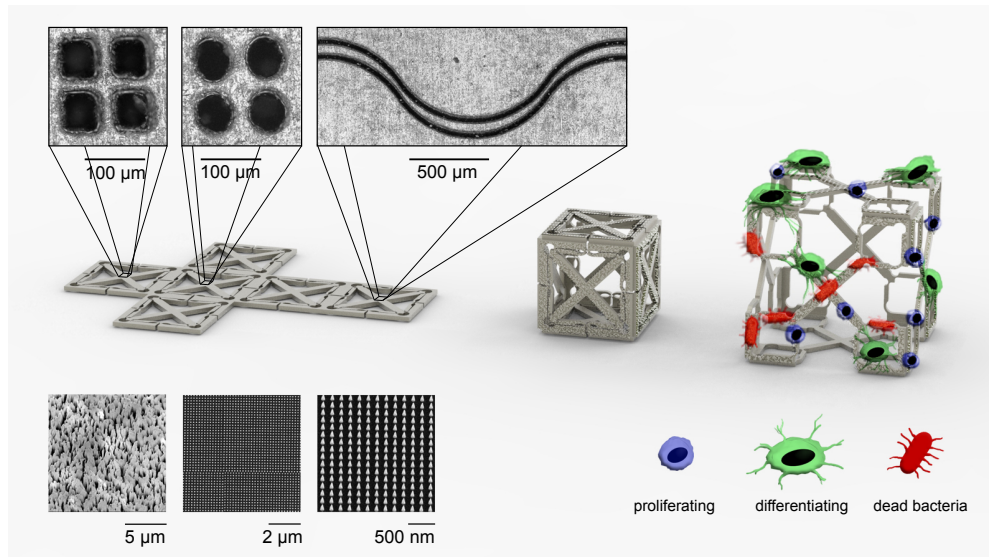
Figure 6. The concept of surface micropatterns and nanopatterns as applied to deployable meta-implants. Top inset: three micropatterns were engraved into a titanium sheet metal specimen (squares, circles and waves). Bottom inset: Some examples of different nanopatterns with specific features (e.g., bactericidal, osteogenic) that could be applied to flat sheets. Left: nanostructures created using RIE, fabrication described by Ganjian et. al (2019) [29], center and right: nanopillars created using EBID [22]. After applying the nanopatterns, the flat specimen can be folded and deployed as meta-implants with different surface-related functionalities.

the layers in the Russian doll designs. That is because these design choices determine the geometrical parameters of such a porous implant including the porosity and pore size. Given the fact that bone tissue regeneration is highly dependent on such geometrical parameters [46,47], the geometrical design of deployable meta-implants could potentially affect their ultimate bone tissue regeneration performance. This and many other aspects of deployable meta-implants need to be studied in future studies.

6.5   Conclusions

We designed and fabricated a new generation of deployable meta-implants using a combination of origami, kirigami, and multi-stability principles. We also applied a multi-layer design, which was inspired by Russian dolls and is also observed in nature. The design strategies applied in the study allow for systematic adjustments of the deployment force, deployment ratio, mechanical properties, pore size, and porosity of the resulting meta-implants. The specimens were manufactured from a variety of materials including PLA, aluminum, and titanium.

We also characterized the deployment behavior and mechanical properties of the manufactured specimens. Since the fabrication of origami-based implants starts from a flat state, it is possible to incorporate precisely-controlled and arbitrarily complex surface micro-/nanopatterns onto the specimens. We demonstrated the feasibility of such surface bio-functionalization using laser micro-machining.

The various functionalities of our design including their deployability, the tunability of the dimensions and mechanical properties, and the applicability of complex surface patterns make these structures a potential replacement for the stents used in vertebral body stenting. The combination of their high porosity and surface nanopatterns could be used to promote bone regeneration and eliminate the use of bone cement.

Future studies are suggested for taking further steps that are required for the clinical adoption of the presented designs. The techniques used in the current study are relatively inexpensive in nature. However, the use of manual labor should be replaced by mass production procedures. Since the proposed approach is amenable to the implementation of these techniques, the production costs of the deployable implants are not expected to be excessively high.

References

[1] D. Sommerfeldt, C. Rubin, Biology of bone and how it orchestrates the form and function of the skeleton, European Spine Journal 10(2) (2001) S86-S95.

[2] E.F. Morgan, G.L. Barnes, T.A. Einhorn, The bone organ system: form and function, Osteoporosis, Elsevier2013, pp. 3-20.

[3] A.A. Zadpoor, Mechanical performance of additively manufactured meta-biomaterials, Acta biomaterialia 85 (2019) 41-59.

[4] H.M. Kolken, S. Janbaz, S.M. Leeflang, K. Lietaert, H.H. Weinans, A.A. Zadpoor, Rationally designed meta-implants: a combination of auxetic and conventional meta-biomaterials, Materials Horizons 5(1) (2018) 28-35.

[5] F. Bobbert, S. Janbaz, A. Zadpoor, Towards deployable meta-implants, Journal of Materials Chemistry B (6) (2018) 3449-3455.

[6] S.A. Tofail, E.P. Koumoulos, A. Bandyopadhyay, S. Bose, L. O'Donoghue, C. Charitidis, Additive manufacturing: scientific and technological challenges, market uptake and opportunities, Materials today 21(1) (2018) 22-37.

[7] A. Zadpoor, Design for additive bio-manufacturing: From patient-specific medical devices to rationally designed meta-biomaterials, International journal of molecular sciences 18(8) (2017) 1607.

[8] A. Yánez, A. Cuadrado, O. Martel, H. Afonso, D. Monopoli, Gyroid porous titanium structures: a versatile solution to be used as scaffolds in bone defect reconstruction, Materials & Design 140 (2018) 21-29.

[9] O. Bas, S. Lucarotti, D.D. Angella, N.J. Castro, C. Meinert, F.M. Wunner, E. Rank, G. Vozzi, T.J. Klein, I. Catelas, Rational design and fabrication of multiphasic soft network composites for tissue engineering articular cartilage: a numerical model-based approach, Chemical Engineering Journal 340 (2018) 15-23.

[10] S.-I. Roohani-Esfahani, P. Newman, H. Zreiqat, Design and fabrication of 3D printed scaffolds with a mechanical strength comparable to cortical bone to repair large bone defects, Scientific reports 6 (2016) 19468.

[11] S. Arabnejad, R.B. Johnston, J.A. Pura, B. Singh, M. Tanzer, D. Pasini, High-strength porous biomaterials for bone replacement: A strategy to assess the interplay between cell morphology, mechanical properties, bone ingrowth and manufacturing constraints, Acta biomaterialia 30 (2016) 345-356.

[12] P. Ouyang, H. Dong, X. He, X. Cai, Y. Wang, J. Li, H. Li, Z. Jin, Hydromechanical mechanism behind the effect of pore size of porous titanium scaffolds on osteoblast response and bone ingrowth, Materials & Design 183 (2019) 108151.

[13] P. Diel, C. Röder, G. Perler, T. Vordemvenne, M. Scholz, F. Kandziora, S. Fürderer, S. Eiskjaer, G. Maestretti, R. Rotter, Radiographic and safety details of vertebral body stenting: results from a multicenter chart review, BMC musculoskeletal disorders 14(1) (2013) 233.

[14] I. Lieberman, S. Dudeney, M.-K. Reinhardt, G. Bell, Initial outcome and efficacy of "kyphoplasty" in the treatment of painful osteoporotic vertebral compression fractures, spine 26(14) (2001) 1631-1637.

[15] D.R. Fourney, D.F. Schomer, R. Nader, J. Chlan-Fourney, D. Suki, K. Ahrar, L.D. Rhines, Z.L. Gokaslan, Percutaneous vertebroplasty and kyphoplasty for painful vertebral body fractures in cancer patients, Journal of Neurosurgery: Spine 98(1) (2003) 21-30.

[16] F.M. Phillips, F.T. Wetzel, I. Lieberman, M. Campbell-Hupp, An in vivo comparison of the potential for extravertebral cement leak after vertebroplasty and kyphoplasty, Spine 27(19) (2002) 2173-2178.

[17] S. Fürderer, M. Anders, B. Schwindling, M. Salick, C. Düber, K. Wenda, R. Urban, M. Glück, P. Eysel, Vertebral body stenting, Der Orthopäde 31(4) (2002) 356-361.

[18] I.H. Lieberman, D. Togawa, M.M. Kayanja, Vertebroplasty and kyphoplasty: filler materials, The Spine Journal 5(6) (2005) S305-S316.

[19] A. Krueger, C. Bliemel, R. Zettl, S. Ruchholtz, Management of pulmonary cement embolism after percutaneous vertebroplasty and kyphoplasty: a systematic review of the literature, European Spine Journal 18(9) (2009) 1257-1265.

[20] X. Lachenal, P.M. Weaver, S. Daynes, Multi-stable composite twisting structure for morphing applications, Proceedings of the Royal Society A: Mathematical, Physical and Engineering Sciences 468(2141) (2012) 1230-1251.

[21] S. Shan, S.H. Kang, J.R. Raney, P. Wang, L. Fang, F. Candido, J.A. Lewis, K. Bertoldi, Multi-stable architected materials for trapping elastic strain energy, Advanced Materials 27(29) (2015) 4296-4301.

[22] M. Ganjian, K. Modaresifar, M.R. Ligeon, L.B. Kunkels, N. Tümer, L. Angeloni, C.W. Hagen, L.G. Otten, P.L. Hagedoorn, I. Apachitei, L.E. Fratila-Apachitei, A.A. Zadpoor, Nature helps: Toward bioinspired bactericidal nanopatterns, Advanced Materials Interfaces 6(16) (2019) 1900640.

[23] K.S. Brammer, S. Oh, C.J. Cobb, L.M. Bjursten, H. van der Heyde, S. Jin, Improved bone-forming functionality on diameter-controlled TiO2 nanotube surface, Acta biomaterialia 5(8) (2009) 3215-3223.

[24] S.J. Callens, N. Tümer, A.A. Zadpoor, Hyperbolic origami-inspired folding of triply periodic minimal surface structures, Applied Materials Today 15 (2019) 453-461.

[25] S. Janbaz, N. Noordzij, D.S. Widyaratih, C.W. Hagen, L.E. Fratila-Apachitei, A.A. Zadpoor, Origami lattices with free-form surface ornaments, Science advances 3(11) (2017) eaao1595.

[26] C. Vieu, F. Carcenac, A. Pepin, Y. Chen, M. Mejias, A. Lebib, L. Manin-Ferlazzo, L. Couraud, H. Launois, Electron beam lithography: resolution limits and applications, Applied surface science 164(1-4) (2000) 111-117.

[27] H. Shahali, J. Hasan, A. Mathews, H. Wang, C. Yan, T. Tesfamichael, P.K. Yarlagadda, Multi-biofunctional properties of three species of cicada wings and biomimetic fabrication of nanopatterned titanium pillars, Journal of Materials Chemistry B 7(8) (2019) 1300-1310.

[28] J. Hasan, S. Jain, K. Chatterjee, Nanoscale topography on black titanium imparts multi-biofunctional properties for orthopedic applications, Scientific reports 7(1) (2017) 1-13.

[29] M. Ganjian, K. Modaresifar, H. Zhang, P.-L. Hagedoorn, L.E. Fratila-Apachitei, A.A. Zadpoor, Reactive ion etching for fabrication of biofunctional titanium nanostructures, Scientific Reports 9(1) (2019) 1-20.

[30] K. Ye, X. Wang, L. Cao, S. Li, Z. Li, L. Yu, J. Ding, Matrix stiffness and nanoscale spatial organization of cell-adhesive ligands direct stem cell fate, Nano letters 15(7) (2015) 4720-4729.

[31] P. Tsimbouri, L. Fisher, N. Holloway, T. Sjostrom, A. Nobbs, R.D. Meek, B. Su, M. Dalby, Osteogenic and bactericidal surfaces from hydrothermal titania nanowires on titanium substrates, Scientific reports 6 (2016) 36857.

[32] X. Shang, L. Liu, A. Rafsanjani, D. Pasini, Durable bi-stable auxetics made of rigid solids, Journal of Materials Research (2017) 1-9.

[33] T.C. Shyu, P.F. Damasceno, P.M. Dodd, A. Lamoureux, L. Xu, M. Shlian, M. Shtein, S.C. Glotzer, N.A. Kotov, A kirigami approach to engineering elasticity in nanocomposites through patterned defects, Nature materials 14(8) (2015) 785.

[34] D. Vanni, A. Pantalone, F. Bigossi, F. Pineto, D. Lucantoni, V. Salini, New perspective for third

generation percutaneous vertebral augmentation procedures: Preliminary results at 12 months, Journal of Craniovertebral Junction and Spine 3(2) (2012) 47.

[35] J. Garnon, B. Doré, P. Auloge, J. Caudrelier, D. Dalili, N. Ramamurthy, G. Koch, R.L. Cazzato, A. Gangi, Efficacy of the Vertebral Body Stenting System for the Restoration of Vertebral Height in Acute Traumatic Compression Fractures in a Non-osteoporotic Population, Cardiovascular and interventional radiology 42(11) (2019) 1579-1587.

[36] S. Schützenberger, S. Schwarz, L. Greiner, O. Holub, S. Grabner, W. Huf, A. Sailler, C. Fialka, Is vertebral body stenting in combination with CaP cement superior to kyphoplasty?, European Spine Journal 27(10) (2018) 2602-2608.

[37] M.R. Shaebani, J. Najafi, A. Farnudi, D. Bonn, M. Habibi, Compaction of quasi-one-dimensional elastoplastic materials, Nature communications 8 (2017) 15568.

[38] R. Hedayati, S. Janbaz, M. Sadighi, M. Mohammadi-Aghdam, A. Zadpoor, How does tissue regeneration influence the mechanical behavior of additively manufactured porous biomaterials?, Journal of the mechanical behavior of biomedical materials 65 (2017) 831-841.

[39] Y. Liu, J. Genzer, M.D. Dickey, "2D or not 2D": Shape-programming polymer sheets, Progress in Polymer Science 52 (2016) 79-106.

[40] T.U. Luu, S.C. Gott, B.W. Woo, M.P. Rao, W.F. Liu, Micro-and nanopatterned topographical cues for regulating macrophage cell shape and phenotype, ACS applied materials & interfaces 7(51) (2015) 28665-28672.

[41] L. Bacakova, E. Filova, M. Parizek, T. Ruml, V. Svorcik, Modulation of cell adhesion, proliferation and differentiation on materials designed for body implants, Biotechnology advances 29(6) (2011) 739-767.

[42] T. Gong, J. Xie, J. Liao, T. Zhang, S. Lin, Y. Lin, Nanomaterials and bone regeneration, Bone research 3 (2015) 15029.

[43] T. Sjöström, M.J. Dalby, A. Hart, R. Tare, R.O. Oreffo, B. Su, Fabrication of pillar-like titania nanostructures on titanium and their interactions with human skeletal stem cells, Acta biomaterialia 5(5) (2009) 1433-1441.

[44] E.K. Yim, E.M. Darling, K. Kulangara, F. Guilak, K.W. Leong, Nanotopography-induced changes in focal adhesions, cytoskeletal organization, and mechanical properties of human mesenchymal stem cells, Biomaterials 31(6) (2010) 1299-1306.

[45] E.P. Ivanova, J. Hasan, H.K. Webb, V.K. Truong, G.S. Watson, J.A. Watson, V.A. Baulin, S. Pogodin, J.Y. Wang, M.J. Tobin, Natural bactericidal surfaces: mechanical rupture of Pseudomonas aeruginosa cells by cicada wings, Small 8(16) (2012) 2489-2494.

[46] Y. Khan, M.J. Yaszemski, A.G. Mikos, C.T. Laurencin, Tissue engineering of bone: material and matrix considerations, Jbjs 90(Supplement_1) (2008) 36-42.

[47] L. Roseti, V. Parisi, M. Petretta, C. Cavallo, G. Desando, I. Bartolotti, B. Grigolo, Scaffolds for bone tissue engineering: state of the art and new perspectives, Materials Science and Engineering: C 78 (2017) 1246-1262.

7

General Discussion and Conclusion

7.1   Main findings of this thesis

The aim of this thesis was to explore the feasibility of making porous biomaterials that are deployable and can be folded from a flat state. In the introduction of this thesis, two reasons were given for this exploration.

1. The lack of porous biomaterials that can be implanted using minimally invasive surgery.
2. It is not possible to apply complex and precisely-controlled surface patterns to the inner surface of three-dimensional porous biomaterials.

To gain more knowledge about the important architectural parameters of porous biomaterials and their effects on the bone regeneration process, a literature review was conducted (Chapter 2). In Chapter 3, rigid porous biomaterials were designed and additively manufactured, and their mechanical and mass transport properties were evaluated. In Chapters 4, 5, and 6, different deployable porous biomaterials were designed and manufactured after which the change in their dimensions and mechanical properties were evaluated.

What are the main requirements for bone substitutes in terms of their geometry, mechanical properties, and mass transport properties and to what extent do existing designs and manufacturing techniques (e.g., 3D printing) achieve those properties?

The architecture of a porous biomaterial affects the bone regeneration process in different ways. Architectural parameters include the pore size, pore shape, porosity, pore interconnectivity, surface topography, surface chemistry, and mechanical properties. The literature review in Chapter 2 demonstrated that these parameters affect cell responses such as proliferation, alignment, and differentiation. Moreover, the mechanical properties of a porous biomaterial are dependent on the material used and the architecture of the porous biomaterial. Pores larger than 400 µm seem to be beneficial for angiogenesis, which is the formation of blood vessels. Angiogenesis is necessary to keep the cells alive given that blood vessels provide the cells with oxygen and nutrients and remove waste products. Furthermore, the bone regeneration process is promoted by large pores, a high porosity, the addition of chitosan or HA, a high surface roughness, and a stiffness close to the elastic modulus of the bone. A higher surface roughness promotes mechanical interlocking, which improves the biomaterial fixation.

Rigid metallic porous biomaterials based on four different types of minimal surfaces were designed using three-dimensional computer models in Chapter 3. Computer models allow for the design of porous biomaterials with the desired properties for the application as bone substitutes. These computer models were used to manufacture the rigid porous biomaterials

using selective laser melting (SLM). Therefore, the micro-architecture of the built structures resembles that of trabecular bone and their porosity ranges between 44% and 71%.

The permeability values (0.05-6.1×10^{-9} m^2) measured for the developed biomaterials were in the range of the values (0.5-14.8×10^{-9} m^2) reported for trabecular bone in the literature.

The mechanical tests show that the elastic modulus of the rigid porous biomaterials varied in the range of 3.2-6.4 GPa. They also show that these structures have a relatively high yield stress (92-276 MPa). Moreover, a high fatigue resistance was obtained with some of the porous structures showing an endurance limit as high as 60% of their yield stress.

How can mechanical joints and elastic deformation be used to develop deployable porous biomaterials?

In Chapter 4, we designed and additively manufactured non-assembly deployable mechanisms for the treatment of large bony defects. These mechanisms have an elongated shape in their retracted configuration. Upon the application of a compressive force at specific locations within the implant structure, the structures retract in the lateral direction and deploy radially into their load-bearing configuration. We integrated different features to lock the deployed configuration of the specimens. Wavelike elements, revolute joints, and restrictions enabled the reconfiguration and locking of the mechanisms. Maximum forces between 1 and 11 N were required to deploy the mechanisms. The maximum failure loads of these mechanisms in their deployed configuration ranged between 200 and 1250 N.

This study demonstrates that deployable porous biomaterials can be manufactured by combining mechanical joints, rigid rods, and wavelike elements into mechanisms. The mechanical joints are used to connect the rigid rods and wavelike elements to each other and enable the movement of these components. Compressive and tensile forces applied to specific locations of these mechanisms cause the wavelike elements to deform elastically. This deformation enables the mechanisms to change their configuration from retracted to deployed and vice versa.

How can elastic deformation be used to develop deployable porous biomaterials?

In Chapter 5, two basic bi-stable elements were designed and 3D printed using a fused deposition modeling (FDM) machine (Ultimaker, The Netherlands). These basic elements consist of flexible components that enable elastic deformation and rigid components that fulfil structural functions. Several design parameters, including the length (*L*) [mm], angle (*α*) [°], and width (*w*) [mm] of the rigid elements determine their mechanical properties and bi-stable behavior. The design parameters of the bi-stable elements affected not only the force required to make the element shift from one stable configuration to the other but could also lead to elements that were not bi-stable at all. The bi-stable elements were used

to assemble five multi-stable structures. The multi-stable structures deploy and retract in the lateral and radial directions, and behave auxetically. The maximum tensile force required to deploy the multi-stable structures varied between 4.5 and 15 N. Retraction occurred when a compressive force between 3 and 10 N was applied to the structures.

This study shows that a combination of rigid and flexible components can be used to develop bi-stable structures. When an external force is applied to a specific location within those elements, the elastic deformation of the flexible components makes the structure snap from one stable configuration to another. By combining bi-stable structures, deployable multi-stable structures can be assembled.

How can deployable porous biomaterials be made foldable in order to apply precisely controlled patterns to their surfaces?

In Chapter 6, we designed and fabricated deployable meta-implants using a combination of origami, kirigami, and multi-stability principles. We also presented a multi-layer design, which was inspired by Russian dolls and is also observed in nature. The design strategies applied in this study allow for the systematic adjustment of the deployment force, deployment ratio, mechanical properties, pore size, and porosity of the resulting meta-implants. The specimens were manufactured from a variety of materials including PLA, aluminum, and titanium. Because the metal origami-based implants are folded from a flat state, it was possible to apply precisely-controlled micropatterns to the surface of the deployable structures.

We characterized the deployment behavior and mechanical properties of the manufactured specimens. The deployable porous biomaterials were deployed using silicone balloons that required a maximum pressure of 3.5 bar to be inflated. The change in dimensions from the retracted position to the deployed configuration ranged between 119% and 179%. Mechanical tests showed that the maximum load that they could support varies between 5 and 75 N.

We have learnt from our study in Chapter 5 that flexible and rigid components can be used to form deployable components. These deployable components can be arranged to form deployable rectangular panels. These panels can then be used to assemble deployable three-dimensional cubes or be organized in a two-dimensional way to create unfolded cubes. These unfolded cubes are suitable to apply surface modifications. After modifying the surfaces, the unfolded cubes can be folded into three-dimensional structures.

Four research questions were answered by a literature review and the development of porous biomaterials using three different manufacturing techniques, four types of materials, and fourteen different designs.

To answer the main research question of this thesis properly, the different designs need to be compared. Therefore, the manufacturing techniques, the deployability of the porous

biomaterials, and the mechanical performance of the implants will be discussed in the following paragraphs.

7.2   Manufacturing techniques

Three different manufacturing techniques were used to fabricate the porous biomaterials, namely selective laser melting (SLM), filament deposition modeling (FDM), and micromachining.

7.2.1   Selective laser melting

In Chapter 3 and 4, we have shown that SLM can be used to create complex, precisely-controlled, and highly porous rigid biomaterials and deployable non-assembly mechanisms. These bone substitutes were made using medical-grade titanium powder and are, thus, biocompatible. SLM is, therefore, an appropriate technique to manufacture bone substitutes.

The main advantage of the rigid structures is that they do not have to be assembled and it is easy to control their porosity, geometry, and size. Moreover, SLM can be used to make the bone substitutes in a patient-specific manner. The deployable non-assembly structures were also immediately functional after manufacturing. However, the revolute joints in these mechanisms increase the complexity of the design. Moreover, due to their three-dimensional nature, it is not possible to apply precisely controlled surface patterns.

7.2.2   Fused deposition modeling

Deployable multi-stable structures were manufactured using FDM in Chapter 5. Simple 3D printed bi-stable elements and connectors were used to manually assemble multi-stable deployable structures. This study showed that bi-stability can be used to create multi-stable deployable structures. PLA, the polymer they were made of, is a biocompatible material and is therefore suitable for the fabrication of bone substitutes. Due to the use of bi-stability, no mechanical joints needed to be integrated, which simplified the designs. Despite the elimination of mechanical joints, it was impossible to miniaturize the designs while keeping the basic elements bi-stable using FDM. Moreover, the multi-stable structures required manual assembly and they were not foldable from a flat state.

FDM was used to manufacture PLA panels with bi-stable elements, which were manually reconfigured to their retracted state in Chapter 6. Deployable cubes were formed by manually connecting the panels to each other. Although it was possible to make several sizes of these cubes, the need for manual retraction and assembly means that the production of such structures cannot be easily upscaled.

7.2.3   Laser micromachining

In addition to the 3D printed PLA structures presented in Chapter 6, aluminum and titanium sheets were cut into unfolded cubes with either deployed or retracted elements using laser micromachining. Laser micromachining is a technique that enables the cutting, engraving, and drilling of sheets of various material types. After cutting unfolded cubes with deployable elements from flat sheets, the panels had to be manually folded to transform the 2D structures into 3D objects. Moreover, nylon threads were used to connect the six panels to prevent the unfolding of the cubes during the deployment process.

7.3   Deployability

The deployable designs presented in Chapter 4, 5, and 6 could all increase in size to a certain extent and in different ways. To make the structures suitable for minimally invasive surgery and the treatment of large bone defects, they should be able to:

1. fit through small incisions (1- 1.5 cm) that are made to insert minimally invasive tools.
2. fit the size of a large bone defect.

In the Introduction of this thesis, large bone defects were defined to be large when the minimum size of the defect is 3 cm in the bones of our lower arm, 5 cm in the bones of our legs, and 6 cm in the bone of our upper arm. With this information, it can be stated that deployable porous structures should have a diameter smaller than 1.5 cm in their retracted state and a height of at least 3 cm in their deployed configuration.

7.3.1   Non-assembly mechanisms

The non-assembly mechanisms developed in Chapter 4 have a circumdiameter in their retracted configuration that ranged between 1.3 and 3.1 cm. The smallest circumdiameter was measured for the bicapped trigonal antiprisms. The non-assembly mechanisms can be deployed by applying compressive forces at the proximal and distal vertices of the mechanisms. Consequently, the structures retract in the lateral direction and expand in the radial direction. The largest (322%) and smallest (185%) changes in the circumdiameter were found for the bicapped trigonal antiprisms and the bicapped cube specimens, respectively. The height of the non-assembly mechanisms in their deployed configuration ranged between 2.1 and 4.6 cm.

7.3.2   Multi-stable structures

The different configurations of the bi-stable elements are responsible for the dimensions of the multi-stable structures. The dimensions of the retracted multi-stable structures varied between 4.5 cm and 21 cm. The multi-stable structures deploy either in the lateral direction or in the lateral and radial direction when tensile forces are applied, with the exception of the ring structure that expands radially upon compression. The maximum increase in height (170%) was acquired for the structure where the basic elements were placed on top of each other. The size of this structure remained the same in the other directions. The size of the ring structure increased the most in the radial direction (by 136%), while no change in the lateral direction occurred. As for the auxetic structures, the largest change in the height was observed for the auxetic structure 1 (by 127%), while the largest change of 127% was observed in the radial direction for the auxetic structure 2.

7.3.3   Deployable cubes

The deployable cubes presented in Chapter 6 deploy in all directions because deployment was induced by the inflation of a balloon. In their retracted configuration, they have a height, width, and length ranging between 0.8 x 0.8 x 0.8 cm and 3.8 x 3.8 x 3.8 cm. The PLA cubes continue to expand until they reach their maximum size, which depends on the initial size of the panels they are assembled of. The smallest change in size was found for the 60% cubes with a sheet thickness of 2 mm. The largest change in the size (*i.e.*, 133%) was found for the full-size (*i.e.*, 100%) cubes with a sheet thickness of 2 mm.

The specimens made of metal sheets deploy to a larger extent due to the plastic deformation of the material. Due to this plastic deformation and the use of a balloon, all metal specimens obtain a spherical shape during the deployment process. The smallest change in the size (132%) was found for the Russian doll specimens with three layers of aluminum sheets. The largest change in the size (179%) was found for the titanium specimens.

The results show that only the bicapped trigonal antiprisms and the titanium deployable cubes would fit through an incision of 1.5 cm. In their deployed configuration, heights of 2.5 cm and 1.4 cm were measured for the bicapped trigonal antiprism and the titanium deployable cube, respectively. Therefore, it can be concluded that for a defect of 3 cm, the bicapped trigonal antiprism may be suitable for implantation if its design is modified. If the retracted dimensions of the titanium deployable cube are increased to 1.5 cm and its change in size can be increased from 179% to 200%, this structure would also fulfill the abovementioned criteria.

7.4 Mechanical performance

7.4.1 Load-bearing locations

For the application as load-bearing bone substitutes, it is important that biomaterials do not fail or deform during daily activities. Studies have shown that the ground reaction force can be as high between 1.3 times [1, 2] and 8 times [3] the body weight during walking and jumping, respectively. Porous bone substitutes need to be able to support these loads to prevent failure of the porous biomaterial, which is caused by plastic deformation or the retraction of the deployed structures. Plastic deformation of the bone substitute can be prevented during any activity, if the induced stresses remain below the yield stress of the material. In the case of the bone, the yield strength is measured to be in the range of 2-18.7 MPa [7, 8] for trabecular bone and 1.7-2278 MPa [9, 10] for cortical bone. However, the highly architected nature and the irregular shape of our designs means that the yield stress values cannot be directly compared with bone nor can "effective mechanical properties" be consistently defined for implants (Chapters 4-6). This is in contrast with more regularly-shaped and architected metamaterials (Chapter 3) for which such effective properties can be defined.

It is important that stress shielding is prevented when a porous biomaterial is implanted inside the body. Stress shielding occurs when the stiffness of a bone substitute is significantly higher than the stiffness of the bone surrounding the implant. This causes under-loading of the bone, which could result in bone resorption around the implant and consequently lead to implant loosening. To avoid stress shielding, the elastic modulus of the implant should be comparable to the stiffness of the surrounding bone. The stiffness of the human cortical and cancellous bone is determined to be 15-20 GPa [4, 5] and 0.02-5.5 GPa [5-7], respectively. The points mentioned above regarding the yield strength are also valid for the elastic modulus. Therefore, in the following paragraphs, the effective mechanical properties are provided in the case of regular meta-biomaterials while force values are reported for the other designs.

7.4.2 Rigid porous biomaterials

The results of the mechanical tests show that the elastic modulus of the rigid porous structures ranged between 3.2 and 6.4 GPa. The yield stress of these structures was found to be 92-276 MPa.

7.4.3 Deployable non-assembly mechanisms

The deployable non-assembly mechanisms could support a maximum load of up to 1212 ± 45.5 N before they failed.

7.4.4   Multi-stable structures

The multi-stable structures could support a maximum load of 10 N before they retracted.

7.4.5   Deployable cubes

The deployable cubes manufactured used PLA could support compressive forces up to 17 N before retraction or fracture of the specimens occurred.

The folded titanium cubes deformed almost immediately after a force was applied. The single-layered and multi-layered aluminum cubes could respectively resist forces of 8 N and 12 N, before plastic deformation occurred.

The results show that the effective yield stress of the rigid porous biomaterials (Chapter 3) is much higher than the yield stress of trabecular bone and falls within the range of the yield stress of cortical bone. Therefore, plastic deformation will not occur if these rigid porous biomaterials are used to fill defects at load-bearing locations. Moreover, the elastic modulus of the porous biomaterials falls within the range of the stiffness of human cortical and trabecular bone. Therefore, no stress shielding is expected to occur when these structures would be applied as porous biomaterials for the regeneration of large bone defects.

The mechanical properties of the deployable porous biomaterials were insufficient to be applied in load-bearing locations. The non-assembly mechanisms could support a maximum load of 1212 N (≈ 120 kg). This means that these mechanisms would only be suitable in load-bearing situation, where the patient does not perform vigorous physical activity and does not weigh more than (120/1.3) 95 kg. The retraction of the deployable structures leads to a reduction of their size and can be seen as failure of the implant. A maximum retraction load of 10 N (≈ 1 kg) was found for the multi-stable structures and 17 N (≈ 1.7 kg) for the deployable cubes with deployable elements.

Plastic deformation of the folded deployable structures occurs when a compressive force of 12 N (≈ 1.2 kg) is applied.

Because the daily activities of patients are hardly predictable, it is important that the mechanical properties of the deployable implants presented here are improved before actual clinical application can be realized.

7.5   Load-bearing capacity of the various designs

The differences in the load-bearing capacity can be explained by the type of the porous biomaterial and the definition of "deployed configuration". The rigid porous structures are rigid and do not contain elements to change their configuration. Therefore, their load-bearing capacity depends on their designed geometry, which can be controlled using computer models. The definition of "deployed configuration" throughout this thesis depends

on the design. The deployable non-assembly porous biomaterials from Chapter 4 and the ring structures from Chapter 5 are defined as "deployed" when they are expanded only in the radial direction. In their deployed configuration, their dimensions in the lateral direction are reduced or remained unchanged. Compressive loads are used to deploy these structures, which brings them into a load-bearing state. Therefore, further compression of these deployed structures is similar to the compression of a rigid load-bearing structure.

The multi-stable structures and the deployable cubes with bi-stable elements are defined as "deployed" when they are expanded in multiple directions. An outward force induced by the inflation of a balloon or tensile forces are used to deploy these structures. When a compressive force is applied to these structures in their deployed configuration, they return to their retracted state because a change in their configuration has already taken place.

The plastically deformed deployable structures folded from flat sheets have the lowest load-bearing capacity. This could be explained by the thickness of the metal sheets, which was 0.125 mm and 1 mm for the titanium and aluminum cubes, respectively. By increasing the sheet thickness or by making multi-layered cubes, the mechanical properties were enhanced. Moreover, the weak part of these structures are the deployable elements, which deform easily upon the application of a force.

7.6 Future work

The main goal of this project was to explore the feasibility of making porous biomaterials that are deployable and foldable from a flat state. In Chapter 6, we presented a potential design which could be explored in future studies. Several opportunities are suggested to improve this concept.

Determine the strength of applied nanopatterns during deployment

Although we have shown that the deployable bone substitutes folded from flat sheets can be patterned using micromachining, these patterns were engraved and not applied on top of the sheet. Many studies have shown that nanopatterning is possible on flat surfaces [11-15]. We may, therefore, assume that similar nanopatterns can be applied to our sheets. However, the actuator we used to deploy our structures was a balloon. This balloon exerts an outward force onto the retracted structure to induce deployment. Therefore, tests should be performed to evaluate whether nanopatterns will remain intact after the deployment process.

Evaluate the cell response on the deployable structures or modification of the inner architecture

The literature review has taught us that many architectural parameters, including porosity, pore size, pore shape, surface properties, and mechanical properties influence the cell response. In this thesis, we have evaluated the mechanical properties and proposed techniques

that enable full control over the surface properties. However, the designs presented are highly porous. Therefore, it is important to perform cell studies to evaluate the *in vivo* cell response of the deployable porous biomaterials folded from flat sheets. If the lack of an inner architecture does not elicit the desired cell response, an 'inner' architecture should be created. This could be realized by inserting components with desired surface properties into the bone substitutes after their deployment. These additional components might also resolve the issue regarding the load-bearing capacity of these structures. The inner object could be a simple filling material, such as highly deformable metal foams that can relatively easily be carried into the inner space of deployed meta-implants.

Enhance the mechanical properties

The mechanical properties of the folded porous biomaterials are at this stage of the development process insufficient for load-bearing applications. Therefore, future studies should focus on improving the mechanical properties of these designs. This could be made possible by increasing the sheet thickness, using or developing other biocompatible materials, or by making multi-layered designs [16].

Create three-dimensional structures from flat surfaces

Many studies have demonstrated the benefits of surface patterns applied on flat surfaces regarding the bone regeneration process. However, these results are only based on two-dimensional implants. To make these patterns valuable for three-dimensional porous biomaterials in the bone regeneration process, it is important that these two-dimensional structures become three-dimensional. Although we have shown that folding is one way to make this happen, there might be other ways to achieve this.

Eliminate manual labor to enable mass-production

Finally, manual folding was used to create three-dimensional structures from flat sheets. The automation of the folding process or self-folding of the sheets could enable mass-production. Self-folding of metal sheets can be realized by adding an elastomeric layer onto a plastically deformable material with specific cutting patterns [17, 18]. By stretching and releasing this multi-layer material, out-of-plane bending can be induced to create three-dimensional structures [17]. This method may be suitable for the folding of our deployable cubes.

Moreover, nylon thread was used to keep the panels of the folded cubes together to prevent the cubes from unfolding during the deployment process and the compression tests. However, this solution is time-consuming and is not suitable for the actual production of potential implants.

7.7 Alternative applications

Vertebral body stenting

One of the commonly occurring problems in the spine are compressed vertebral fractures (CVFs) caused by osteoporosis [19]. This could lead to a loss in the height of the vertebra, back pain, and impaired mobility [19, 20]. Vertebroplasty is a treatment to prevent further compression of a compressed vertebra and includes the injection of bone cement into the vertebra [20]. VCFs can also be treated by kyphoplasty, which is performed by inflating a balloon inside the vertebra prior to the injection of bone cement [20]. The inflation of the balloon restores the height of the vertebra, which is then fixed by the volume of the bone cement. An alternative to kyphoplasty is vertebral body stenting. For this procedure, a stent is mounted onto a balloon catheter, which is deployed upon the inflation of the balloon. After the balloon catheter is removed, bone cement is injected to stabilize the vertebra. Unfortunately, the use of bone cement could lead to complications due to cement leakage [20]. Moreover, cement does not allow for bony ingrowth. To eliminate bone cement from the treatment of compressed vertebral fractures, deployable bone substitutes with a sufficient load-bearing capacity could be used. To be suitable for this application, the structures should be capable of bearing the weight of the upper trunk, which has been calculated to range between 0.6 and 1.95 times the body weight (corresponding to upright standing and 30 degrees forward bending) [21].

Other applications

The recent progress in microfabrication and nanofabrication techniques and the development of micro-electromechanical (MEM) and nano-electromechanical (NEN) systems have increased the importance of folding three-dimensional structures from a flat state [22]. This is due to the improvement of the performance of devices and systems in which advanced functionalities are added to a two-dimensional surface [22]. However, two-dimensional structures lack specific features that three-dimensional structures offer, including an extra dimension and more diversity in the geometry. These features provide for improved physical interactions, better performance, and additional functionalities [22]. Therefore, the foldable structures or the techniques proposed in this thesis may find applications other areas of research, including drug delivering systems [23, 24], biosensors [25, 26], and reconfigurable antennas [27].

7.8 Conclusions

This thesis presents an exploration of deployable porous biomaterials and how they can be folded from a flat state. Several prototypes were designed and manufactured by selective laser melting, fused deposition modeling, and micromachining. The presented structures

were made reconfigurable by revolute joints and the use of elastic and plastic deformation. Due to the lack of porous biomaterials which can be implanted with minimal invasiveness or the inability to apply controlled surface patterning techniques to three-dimensional structures, the central research question of the thesis was defined as

"Is it feasible to fold deployable biomaterials from a flat state which can be used for the treatment of large bone defects?"

The work presented in this thesis demonstrates that deployable porous biomaterials can be folded from a flat state. The foldable, deployable implants are, however, not yet capable of reaching the favorable properties of rigid porous biomaterials manufactured designed using triply periodic minimal surfaces and manufactured using SLM. Moreover, the design of a deployable structure determines the change in dimensions from retracted to deployed and whether a structure deploys in all directions or if deployment occurs in one direction while retraction occurs in the other direction(s). Furthermore, deployable structures that are deployed using compressive forces have a higher load-bearing capacity than structures which deploy upon the application of tensile forces or structures which expand in all directions upon the inflation of a balloon.

Laser micromachining is a promising technique to fabricate two-dimensional structures, which can be folded into three-dimensional structures. These sheets enable the application of precisely controlled surface patterns and other functionalities. After modifying the surface, the structures can be folded into three-dimensional structures, which can be deployed upon the inflation of a balloon. However, the mechanical properties of the current designs are not yet sufficient for load-bearing applications.

Overall, the work in this thesis is the first step in the development of deployable porous biomaterials that can be folded from a flat state. We hope that our designs inspire future research for further developments that will eventually lead to foldable, deployable meta-implants that are suitable for minimally invasive surgery and whose entire surface area is decorated with precisely-controlled surface nanopatterns.

References

[1] M.-C. Chiu, M.-J. Wang, The effect of gait speed and gender on perceived exertion, muscle activity, joint motion of lower extremity, ground reaction force and heart rate during normal walking, Gait & posture 25(3) (2007) 385-392.

[2] S.I. Ismail, H. Nunome, F.F. Marzuki, I. Suaidi, The influence of additional surface on force platforms ground reaction force data during walking and running, American Journal of Sports Science 6(3) (2018) 78-82.

[3] D.J. Cleather, J.E. Goodwin, A.M. Bull, Hip and knee joint loading during vertical jumping and push jerking, Clinical biomechanics 28(1) (2013) 98-103.

[4] S. Zhao, M. Arnold, S. Ma, R.L. Abel, J.P. Cobb, U. Hansen, O. Boughton, Standardizing compression testing for measuring the stiffness of human bone, Bone & Joint Research 7(8) (2018) 524-538.

[5] J.D. Black, B.J. Tadros, Bone structure: from cortical to calcium, Orthopaedics and Trauma (2020).

[6] P. Augat, T. Link, T.F. Lang, J.C. Lin, S. Majumdar, H.K. Genant, Anisotropy of the elastic modulus of trabecular bone specimens from different anatomical locations, Medical engineering & physics 20(2) (1998) 124-131.

[7] J. Wang, B. Zhou, X.S. Liu, A.J. Fields, A. Sanyal, X. Shi, M. Adams, T.M. Keaveny, X.E. Guo, Trabecular plates and rods determine elastic modulus and yield strength of human trabecular bone, Bone 72 (2015) 71-80.

[8] E.F. Morgan, T.M. Keaveny, Dependence of yield strain of human trabecular bone on anatomic site, Journal of biomechanics 34(5) (2001) 569-577.

[9] N. Wachter, G. Krischak, M. Mentzel, M. Sarkar, T. Ebinger, L. Kinzl, L. Claes, P. Augat, Correlation of bone mineral density with strength and microstructural parameters of cortical bone in vitro, Bone 31(1) (2002) 90-95.

[10] K.J. Jepsen, D.T. Davy, Comparison of damage accumulation measures in human cortical bone, Journal of Biomechanics 30(9) (1997) 891-894.

[11] A.I. Greer, V. Goriainov, J. Kanczler, C.R. Black, L.-A. Turner, R.M. Meek, K. Burgess, I. MacLaren, M.J. Dalby, R.O. Oreffo, Nanopatterned titanium implants accelerate bone formation in vivo, ACS applied materials & interfaces 12(30) (2020) 33541-33549.

[12] S. Lavenus, J.-C. Ricquier, G. Louarn, P. Layrolle, Cell interaction with nanopatterned surface of implants, Nanomedicine 5(6) (2010) 937-947.

[13] M. Ganjian, K. Modaresifar, M.R. Ligeon, L.B. Kunkels, N. Tümer, L. Angeloni, C.W. Hagen, L.G. Otten, P.L. Hagedoorn, I. Apachitei, L.E. Fratila-Apachitei, A.A. Zadpoor, Nature helps: Toward bioinspired bactericidal nanopatterns, Advanced Materials Interfaces 6(16) (2019) 1900640.

[14] M. Ganjian, K. Modaresifar, H. Zhang, P-L. Hagedoorn, L.E. Fratila-Apachitei, A.A. Zadpoor, Reactive ion etching for fabrication of biofunctional titanium nanostructures, Scientific Reports 9(1) (2019) 1-20.

[15] L. Richert, F. Vetrone, J.H. Yi, S.F. Zalzal, J.D. Wuest, F. Rosei, A. Nanci, Surface nanopatterning to control cell growth, Advanced Materials 20(8) (2008) 1488-1492.

[16] J. Yanagimoto, T. Oya, S. Kawanishi, N. Tiesler, T. Koseki, Enhancement of bending formability of brittle sheet metal in multilayer metallic sheets, CIRP annals 59(1) (2010) 287-290.

[17] T. van Manen, S. Janbaz, M. Ganjian, A.A. Zadpoor, Kirigami-enabled self-folding origami, Materials Today 32 (2020) 59-67.

[18] Z. Meng, W. Chen, T. Mei, Y. Lai, Y. Li, C. Chen, Bistability-based foldable origami mechanical logic gates, Extreme Mechanics Letters (2021) 101180.

[19] J.L. Old, M. Calvert, Vertebral compression fractures in the elderly, American family physician 69(1) (2004) 111-116.

[20] H. Zhang, C. Xu, T. Zhang, Z. Gao, T. Zhang, Does percutaneous vertebroplasty or balloon kyphoplasty for osteoporotic vertebral compression fractures increase the incidence of new vertebral fractures? A meta-analysis, Pain physician 20(1) (2017) E13-E28.

[21] I. Takahashi, S.-i. Kikuchi, K. Sato, N. Sato, Mechanical load of the lumbar spine during forward bending motion of the trunk–a biomechanical study, Spine 31(1) (2006) 18-23.

[22] Z. Liu, A. Cui, J. Li, C. Gu, Folding 2D structures into 3D configurations at the micro/nanoscale: principles, techniques, and applications, Advanced materials 31(4) (2019) 1802211.

[23] R. Fernandes, D.H. Gracias, Self-folding polymeric containers for encapsulation and delivery of drugs, Advanced drug delivery reviews 64(14) (2012) 1579-1589.

[24] C.L. Randall, T.G. Leong, N. Bassik, D.H. Gracias, 3D lithographically fabricated nanoliter containers for drug delivery, Advanced drug delivery reviews 59(15) (2007) 1547-1561.

[25] T. Bertok, A. Sediva, A. Vikartovska, J. Tkac, Comparison of the 2D and 3D nanostructured lectin-based biosensors for in situ detection of sialic acid on glycoproteins, International journal of electrochemical science/Electrochemical Science Group 9(2) (2014) 890.

[26] J.F. Loo, A.H. Ho, A.P. Turner, W.C. Mak, Integrated printed microfluidic biosensors, Trends in biotechnology 37(10) (2019) 1104-1120.

[27] G.J. Hayes, Y. Liu, J. Genzer, G. Lazzi, M.D. Dickey, Self-folding origami microstrip antennas, IEEE Transactions on Antennas and Propagation 62(10) (2014) 5416-5419.Acknowledgements

Acknowledgements

Before I started my PhD, I went to England and Scotland with my motorbike for three weeks. This was, until then, the biggest adventure of my life. Riding through Scotland in the rain, snow, hail and only three days of dry weather was not exactly what I had in mind when I started this trip. Luckily, the beautiful landscape kept me going and after a few rainy days I discovered that when I kept riding towards my next destination, the rain would pass and dry afternoons and evenings would await me to enjoy a walk along the West coast of Scotland.

Two weeks after my return I started my PhD project, which appeared to be another type of adventure. Thanks to my time in Scotland, I knew how to deal with challenging situations. However, I would not have enjoyed my PhD adventure as much as I did without my colleagues, friends and family.

Thanks to you, **Amir**, I have completed the biggest challenge of my life so far. Your idea to make porous biomaterials for the treatment of large bone defects not only foldable from a flat state but also deployable, was only one of the great ideas you have had in the past few years. Although this project has made me doubt so many times whether I was the right person to tackle this problem, I am very thankful that you have given me this opportunity. Because in spite of all the struggles, I have learnt a lot and had a great time. Thank you for always being there to motivate me and to tell me not to stress too much. You have a great talent for assembling a group of amazing people.

The last year of my PhD adventure was troublesome due to the Covid-19 situation. Trying to work from home with a baby to take care of appeared to be impossible. Luckily, **Mirjam** helped me to deal with this situation, for which I will always be grateful. I also need to thank **DirkJan**, who understood my unfortunate situation and gave me some extra time to finish my thesis.

Angelique, Marjolijn and **Sabrina**, thank you for the nice talks and your help when I needed materials for my project.

Without lab coordinators, labs would be a complete mess and everything would be broken. From the Materials Engineering department, I would like to thank **Ton** for the conversations we had about our motorbike trips and (big) **Sander** for all the nice chats in the hallway, in the lab, on the floor while assembling the wedding gift for Michelle, and your great stories. (Small) **Sander**, thank you for bringing the Biomaterials lab to a higher level. It was always a pleasure to work, talk, and drink coffee with you. Your creative contributions for the various presents we gave to colleagues were much appreciated. Without you and your endless patience, many people would be lost and the lab would be a complete disaster.

Along the way, **Bob, Eric, Esther, Fabian, Helda, Iulian, Jiahui, Jie, Jonathan, Juan, Judith,**

Lidy, Livia, Mahdiyeh, Marike, Michelle, Mohammad, Nazli, Paul, Pedro, and **Teunis**, made my adventure more pleasant with nice talks in the hallway, during lunch and in the lab.

Social events such as movie nights, a BBQ and the laser game afternoon in the Delftse Hout with colleagues have made my time as a PhD candidate more fun. Therefore, I would like to thank **Jinne, Bart** and **Daniel**. It was a pleasure to organize these events with you during fun and efficient lunch meetings.

My PhD adventure started with a bumpy road which got me completely lost. Without **Shahram**, I would probably still be thinking about how and where to start. You have taught me to just realize ideas into real objects to see whether they work or not instead of endlessly thinking about the idea. I have enjoyed all the times we worked together and I will never forget how one of your ideas led to many others.

Working in a multinational group has many advantages. You learn to eat and cook new things, to speak or write (and forget) Chinese or Persian, and with some Iranian, Mexican, Greek or Indonesian colleagues, you end up speaking Dutch. I have enjoyed all the nice (sometimes confusing) Dutch conversations I have had with **Katerina, Khashayar, Mahya, Mauricio** and **Niko**. It is amazing and impressive that you have learnt a new language while doing a PhD.

Although I have not spent much time with you as colleagues, **Katerina, Kirsten, Mauricio, Merle** and **Pier**, I always enjoyed the great times we had during my visits at 3mE with Alex and all the social events.

Mahya, we have shared our office for almost 3.5 years. You have become a great and generous friend and I have enjoyed all the delicious Turkish and Persian dinners, the coffees and ice creams we had together and all the (Persian) snacks you brought to our office. Although we have only shared our office for a year in which we saw each other not more than five times, **Khashayar**, I am very happy that we became friends already before you conquered a spot in our office. I still think it is incredible how fast you have learnt to speak Dutch and it was always fun to try to answer your questions about the Dutch language. Thank you (and **Sara**) for all the nice conversations and the super delicious dinners and lunches with way too much food. **Ingmar**, you are a great listener, I appreciate your down-to-earth mentality and you always seem to know the right things to say. I am glad that we have stayed in touch since you have moved to Italy. **Costanza**, thank you for bringing life (and occasionally confusion) to any conversation. Your presence is always welcome and I truly appreciate the times that you (and **Fede**) stopped in front of our house during the Covid-19 crisis.

Coffee (and hot cocoa) breaks are needed to stay hydrated and relaxed, and most of them I had with **Niko**. Niko, you always make me happy with your big smile and it is great to see you and Alex running around and playing together.

Eline, I met you while you were working on your master's thesis and I got to know you when you became my colleague. You have become a true friend and you have supported me

by always understanding my struggles and thoughts. Thank you for all the talks, the great times and dinners we have had together.

When people are working on the same project and are struggling with similar problems, it is convenient when you can share your thoughts. **Sebastien**, thank you for motivating me every time when I was not sure whether I was going in the right direction with my project. You have inspired me by your great work and I am happy that we have stayed in contact since you have moved to London. I am looking forward to seeing you (and **Delphine**) again for a nice dinner or lunch.

Yageng, although you are back in China, you will always be a friend of mine and Thomas and uncle Li for Alex. Thank you for all the good times we shared inside and outside our office. I will always remember the many (Chinese) dinners we had with Leffe Blond and Doritos.

In addition to some colleagues who have become my friends, I would like to thank some other friends.

Astrid and Thomas, it is always a pleasure to be with you during the planned and unexpected visits at (y)our place. You and the chocolate coated marshmallows are always welcome.

The cover of this thesis would not have looked like this without **Jody**. Jody, you gave me the best birthday present I could wish for this year. The colored pencils enable me to bring color to my drawings and have motivated me to design this cover. I am also thankful for the many evenings with good food, drinks and conversations.

Reza, although you have moved to England and we cannot enjoy delicious and relaxed dinners with you anymore, the Signal conversations we still have are much appreciated.

Maria, I am grateful that I have met you during my internship in Leuven and I am happy that you and **Miguel** have moved to The Netherlands.

Dear aunt **Nicole**, thank you for being there for me in the last year. I have enjoyed all the talks and walks we had in the Delftse Hout and all the delicious food at your place.

Linda and **Jan Willem**, my lovely parents-in-law, thank you for all your support and love. I will always be thankful for all the times that you dropped everything to come to us to take care of Alex. **Marc** and **Annelieke**, although we do not see each other often, I am always enjoying our time together.

Dear **mom** and **dad**, you are both lovely and considerate people and I love you for who you are. Thank you for always supporting me, for guiding me in becoming the person I am today, and for being amazing grandparents for Alex. Mom, thank you for being the best example I could have to teach me how to always care for and think about other people. Dad, thank you for convincing me to accept this PhD position. Telling me about your experiences from your time as a PhD candidate and your work have helped me a lot in the last few years. **Sharon**, I am grateful that you have become a part of my life by meeting my dad.

Mireille, I am happy to be your sister and that we are seeing each other more often since a few years. I admire the way you live your life and I hope you will one day become a successful business owner. You are a great sister and the best aunt Alex could wish for.

Where the beautiful landscape and the thought of dry afternoons and evenings kept me going in Scotland, there are two persons who will always keep me going in my daily life.

Dear **Alex**, I still cannot believe that such a happy, always smiling, funny and sweet boy like you are my son. I hope you will always stay as open and generous as you are right now. Thank you for always making me happy with your presence, a hug, a smile or a kiss.

Thomas, there are no words to describe how happy I am with you as my partner and the father of our son. Doing my PhD was challenging and almost impossible in the last year due to the Covid-19 situation. The fact that we have survived these difficult times and are still happy together confirms that we can handle any situation as long as we are together. You are an amazing person and you will always be my best friend.

This adventure has come to an end and I am sure I would not have enjoyed it as much as I did if it was not for all the great conversations, social events, and all your support. Thank you all for being there for me.

Curriculum vitae

Françoise Siu Lin Bobbert was born on 11 March 1988 in the Amstelland hospital in Amstelveen. She attended secondary school from 2000 to 2007 at the Herman Wesselink College in Amstelveen and decided to study Industrial Design Engineering at the Delft University of Technology in 2007.

In the third year of her bachelor's program she discovered Biomedical Engineering and decided to start the master's program in Biomedical Engineering after obtaining her bachelor's degree and taking a gap year. In this gap year she made 3D visualizations of interiors for interior design companies Imposing Design and Sfeer Interieur.

After obtaining her master's degree in Biomedical Engineering, she became a PhD candidate in the group of Amir Zadpoor at the BioMechanical Engineering department at the Delft University of Technology. This led to the challenging job to develop deployable implants folded from a flat state of which the result is presented in this thesis.

Publications

- Y. Li, P. Pavanram, J. Zhou, K. Lietaert, **F.S.L. Bobbert**, Y. Kubo, M.A. Leeflang, H. Jahr, A.A. Zadpoor, Additively manufactured functionally graded biodegradable porous zinc, Biomaterials Science 8(9) (2020) 2404-2419.

- **F.S.L. Bobbert**, S. Janbaz, T. van Manen, Y. Li, A.A. Zadpoor, Russian doll deployable meta-implants: Fusion of kirigami, origami, and multi-stability, Materials & Design (2020) 108624.

- Y. Li, W. Li, **F.S.L. Bobbert**, K. Lietaert, J. Dong, M.A. Leeflang, J. Zhou, A.A. Zadpoor, Corrosion fatigue behavior of additively manufactured biodegradable porous zinc, Acta Biomaterialia (2020).

- M. Mirzaali, **F.S.L. Bobbert**, Y. Li, A.A. Zadpoor, 4 Additive Manufacturing of Metals Using Powder Bed-Based Technologies, Additive Manufacturing (2019) 93.

- Y. Li, H. Jahr, P. Pavanram, **F.S.L. Bobbert**, U. Paggi, X.-Y. Zhang, B. Pouran, M.A. Leeflang, H. Weinans, J. Zhou, A.A. Zadpoor Additively manufactured functionally graded biodegradable porous iron, Acta biomaterialia 96 (2019) 646-661.

- S. Janbaz, **F.S.L. Bobbert**, M. Mirzaali, A.A. Zadpoor, Ultra-programmable buckling-driven soft cellular mechanisms, Materials Horizons 6(6) (2019) 1138-1147.

- **F.S.L. Bobbert**, S. Janbaz, A.A. Zadpoor, Towards deployable meta-implants, Journal of Materials Chemistry B 6(21) (2018) 3449-3455.

- **F.S.L. Bobbert**, K. Lietaert, A.A. Eftekhari, B. Pouran, S. Ahmadi, H. Weinans, A.A. Zadpoor, Additively manufactured metallic porous biomaterials based on minimal surfaces: A unique combination of topological, mechanical, and mass transport properties, Acta biomaterialia 53 (2017) 572-584.

- **F.S.L. Bobbert**, A.A. Zadpoor, Effects of bone substitute architecture and surface properties on cell response, angiogenesis, and structure of new bone, Journal of Materials Chemistry B 5(31) (2017) 6175-6192.